Engineering of the light elements in silicon for the photovoltaic application

Dilyara Timerkaeva

UNIVERSITÉ DE GRENOBLE

THÈSE

Pour obtenir le grade de

DOCTEUR DE L'UNIVERSITÉ DE GRENOBLE

Spécialité : **Physique des matériaux**

Arrêté ministériel : 7 août 2006

Présentée par

Dilyara TIMERKAEVA

Thèse dirigée par **Pascal POCHET**
et codirigée par **Damien CALISTE**

préparée au sein **Laboratoire de simulation atomistique**
et de **L'école doctorale de physique de Grenoble**

Ingénierie des éléments légers dans le silicium pour applications photovoltaïques

Thèse soutenue publiquement le 10 avril 2015,
devant le jury composé de :

Dr. Noël JAKSE
Président
Dr. Guy TRÉGLIA
Rapporteur
Dr. Laurent PIZZAGALLI
Rapporteur
Dr. Pascal POCHET
Examinateur
Dr. Damien CALISTE
Examinateur
Dr. Claudio ATTACCALITE
Examinateur

Résumé

Depuis des années, le silicium est le semiconducteur principalement utilisé dans l'industrie électronique et photovoltaïque. Intensivement étudié depuis plusieurs décennies, ses propriétés sont essentiellement connues, mais de nouvelles questions viennent se poser. En particulier, une meilleure connaissance des nombreux défauts et impuretés ainsi que leurs propriétés et leur impact sur les performances des dispositifs à base de Si est souhaitable.

Ce travail couvre un éventail de problèmes liés aux défauts ponctuels en interaction au moyen de calculs dits de premiers principes (Density Functional Theory).

Une première partie est dédiée à l'impact du dopage sur la diffusivité de l'oxygène interstitiel. Les coefficients de diffusion obtenus en fonction de la température sont en très bon accord avec les résultats expérimentaux ce qui démontre la validité de la méthodologie appliquée. Nous avons montré que l'augmentation de la diffusivité dans le silicium dopé bore se produit par un mécanisme de transfert de charge depuis le dopant de type p.

Une deuxième partie se rapporte aux différents complexes de défauts ponctuels et leur thermodynamique, leur cinétique, et leurs propriétés optiques. La formation de ces complexes peut être induite expérimentalement par une irradiation par des électrons. Plus généralement, ils apparaissent aussi dans des environnements opérationnels particuliers comme le spatial. Ici, nous avons réalisé une étude expérimentale et théorique combinée pour identifier l'impact du dopage isovalent (C, Ge) et du co-dopage (C-Ge, C-Sn, C-Pb) sur la production de différents complexes (VO_i, C_iO_i, C_iC_s), qui sont électriquement et optiquement actifs.

Enfin, une attention particulière a été portée à la paire de défaut carbone-carbone et ses propriétés. Récemment, il a été établi que le silicium fortement dopé en carbone présente des propriétés d'émission laser. Ici nous avons cherché à étudier les formes possibles du complexe et leurs propriétés, afin de comprendre lequel est présent expérimentalement.

Abstract

Since many years, silicon is the primary semiconductor material in electronic and photovoltaic industry. Intensively studied through decades, its properties are essentially known, however new questions keep arising. We need to achieve deep insight into the numerous possible defects and impurities properties as well as their impact on the performances of the Si based devices. This work covers a range of problems related with point defects interaction of both types long range and short range by means of parameter free first principles calculations.

The former refers to the impact of heavy doping on diffusivity of interstitial oxygen species. The obtained diffusion coefficients as a function of temperature are in a very good agreement with experimental results that demonstrates the validity of the applied methodology. We showed that the enhanced diffusivity in B-doped silicon occurs through a charge transfer mechanism from the p-type dopant

The latter accounts for the various point defect complexes and their thermodynamic, kinetic, and optical properties. Formation of these complexes can be induced by electron irradiation of Czochralski silicon. This aspect is of extreme importance for particular operational environment. Here, we performed a combined experimental-theoretical investigation to identify the impact of isovalent doping (C, Ge) and co-doping (C-Ge, C-Sn, C-Pb) on the production of different complexes (VO_i, C_iO_i, C_iC_s, *etc.*), which are electrically and optically active.

Finally, particular attention is addressed to the carbon-carbon defect pair and its properties. Recently, it was established that heavily carbon doped silicon elucidates lasing properties. Here we aimed to revisit the possible forms of the complex and their properties, in order to associate one of them with light emitting G-centre, observed in experiments.

Acknowledgements

Firstly, I would like to thank my supervisor, Dr. Pascal Pochet, for his guidance and support throughout these three years. Also my special thanks go to Damien Caliste, Thierry Deutsch, and Claudio Attaccalite, who have contributed much towards my progress and understanding.

I am very thankful for our experimental collaborators, in particular Charalampos Londos, Sébastien Dubois and their groups. I am also grateful to everyone who contributed to the BigDFT code development.

I thank all the members of L_Sim lab, in particular Paul Boulanger, Laura Ratcliff, Luigi Genovese, Frédéric Lançon, Yann-Michel Niquet, Gilles Brenet, Alex Marchenko, Maxime Moriniere, Alessandro Cerioni, Ivan Duchemin, Stephan Mohr, Jing Li, Elena Zvereva, Eduardo Machado-Charry.

This thesis couldnot be possible without my lovely friends, who have made my stay in Grenoble brighter and filled my heart with lots of happy memories. In particular, I thank Emerson Vathonne, Anita Sarkar, Anna Wolnik, Izabela Petrykiewicz, Williams Savero Torres, Arpan Krishna Deb, Dibyendu Hazra, Anna Mukhtarova, Vadim Mukhtarov, Joanna Gorniak, Joanna Andrecka, Pan Chen, Tatiana Krishtop, Vladimir Maryasin, Valeria Maryasina, Olesia Danyliv, Oleksandr Nechyporchuk, Andrey Eliseev. I also appreciate support of my old friends, Olga Fedorovich, Diana Bukaeva, Maria Kraynova, Niyaz Beysengulov, Bulat Fattakhov, Ildar Fattakhov. Apologies and thanks to those who were not specifically mentioned, but equally contributed to my happiness during that period.

For their constant support, encouragement, and being always there, I thank my dearest family - to whom I dedicate this thesis.

Contents

Chapter 1

Introduction

Since many years, silicon is the primary semiconductor material in electronic and photovoltaic (PV) industry. It withstands the competition with new materials which show better performances in a range of properties. Compare to other materials, the main advantages of silicon are its cheapness and the existence of developed fabrication technologies. As a result, the semiconductor industry is well suited to the production of silicon based devices, such as silicon based integrated circuits and solar cells. In 2013, 90% of the total PV world production were based on the Si-wafers [124].

Intensively studied through decades, silicon properties are essentially known. However, industrial needs introduce new challenges: we now need small, high-performant, and in the meantime, cheap devices.

The latter criterion becomes the driving force for the modern industry and science. As far as the fabrication of highly purified silicon is extremely expensive, cheaper techniques are often used. As a result, we deal with silicon that contains impurities, intrinsic point defects, and dopants. The latter are added in silicon to vary the conductivity type. Types and quantities of defects presented in silicon depend on the growing method, compound of the initial melt, and the post-growing treatment, including irradiation and ion implantation. Hence, we need to achieve deep insight into the numerous possible defects and impurities properties as well as their impact on the performances of the Si based devices.

Among all the variety of impurities, oxygen is natively present in silicon during the crystal growth. Individual atoms of oxygen are electrically inactive, however they associate with each other and with other impurities. The resulting complexes sometimes affect significantly electrical and photovoltaic properties of future devices. Two examples are listed below. First, heating the silicon sample up to 450 ℃ leads to the formation of Thermal Donors (oxygen containing agglomerates). Second, under illumination, oxygen associates with boron, forming the so-called boron-oxygen complexes. Although the concentration of such complex is rather low 10^{11} cm^{-3},

its presence drastically degrade the solar cells efficiency. This effect is called Light Induced Degradation (LID). The complex's composition and formation mechanism is still unknown, despite significant efforts performed in this direction [116, 12, 3, 43, 72, 134].

The first problem, that will be addressed in this thesis, is in close connection with the formation process of boron-oxygen complexes: we will investigate the oxygen migration mechanisms in doped silicon by means of parameter free first principles calculations. This problem raised from the recent observation of significantly enhanced oxygen diffusivity in heavily B-doped silicon at low temperature regime $T < 700$ ℃ [139]. The acceleration of oxygen diffusion in presence of boron can thus accelerate the undesired defects formation. At the same time, the intensive doping with some other elements, namely Ge, As, and Sn, showed less prominent effect on oxygen migration properties. However, the mechanisms of enhanced or retarded diffusivity are not accessible through experimental techniques. That is why, we aimed to calculate the diffusion coefficient of the migrating oxygen species using the Density Functional Theory approximation.

Irradiation induced material properties is another aspect, closely related with point defects in silicon. This aspect is of extreme importance for particular operational environment. Either enhanced or reduced sensitivity to irradiation is required for a number of applications, such as dosimetry, particle detection, medical equipment, satellite and space station equipment. It is of a great importance to investigate point defect engineering techniques and strategies to master those properties through controlled defect manipulation. Therefore, in the second part of this work we investigate point defects associated with the electron irradiation.

A large variety of impurity associations occurs under electron irradiation. Vacancies and self-interstitials interact with impurities that results in complexes formation. Some of those act as recombination centers and reduce electrical characteristics of future devices. In order to avoid their formation, two solutions are possible. The first one consists in using the impurity-free silicon. In the absence of impurities, any associations will be impossible. However, this solution requires an expensive purification method. The second one consists in finding a proper defect engineering strategy. For example, by adding electrically inactive impurities, we can intend to avoid the detrimental complexes formation in irradiated silicon. The best candidates for that role are isovalent dopants. Their impact on the hardening potential of silicon will be investigated in this thesis by employing combined experimental-theoretical methods.

Finally, the third aspect, that is addressed in this thesis, is the carbon-carbon defect pair and its properties. Recently, it was established that heavily carbon doped silicon elucidates lasing properties. The complex related to this feature is detected to

be C_iC_s complex. Three variations of the complex have been proposed in literature. One of them is widely accepted to be related with light emitting G-centre, however no theoretical confirmation has been presented yet. Here we aimed to revisit the possible forms of the complex and their properties, in order to associate one of them with light emitting G-centre, observed in experiments.

The thesis will be organized as follows. In Chapter 2, we will represent the state of the art in the field of point defects in silicon, followed by the open questions which will be addressed in this thesis. In Chapter 3, we introduce the details of the theoretical methodology employed in the rest of the thesis. In Chapter 4, we present our results on the diffusion coefficient calculations of interstitial oxygen species in pristine and heavily doped silicon. Chapter 5 deals with irradiation induced point defects formation and temperature evolution in isovalently doped and co-doped silicon. Here, we present and analyze the experimental results, obtained by our Greek colleagues along with the multi-scale simulations, accounting for both thermodynamic and kinetic aspects of various point defects associations. Chapter 6 addresses the structural, thermodynamic, vibrational, and optical properties of the C_iC_s complex. And finally, in Chapter 7, we draw conclusions of the present contribution along with perspectives in the field of point defects in silicon.

Chapter 2

State of the Art

This chapter addresses the state of the art in the field of point defects and impurities in silicon. We start by a short description of the origin of point defects in crystalline silicon. Then we classify the possible point defects and complexes in bulk silicon, depending on their origin and properties. We overview, how the performances of silicon-based devices are affected as by these point defects, as well as by their long-range and short-range interactions.

Particularly, we address the oxygen transport as it is responsible for the formation of electrically active thermal donors and B-O complexes. We summarize the recent experiments showing how heavy doping impacts the oxygen transport and specify the open questions.

The electron irradiation causes the formation of a large variety of defect complexes, which impact electrical, photovoltaic, and optical properties of crystalline silicon. This is the second point that we address in this chapter. We overview how electron irradiation affects the Czochralski silicon and emphasize the related questions. We also consider the impact of the isovalent co-doping on complexes formation in irradiation hardness of Czochralski silicon.

Finally, we discuss the irradiation induced CiCs complex. It rises the lasing properties of crystalline silicon. We overview the experimental and theoretical studies of its properties and point out the question of the possible complex configurations.

2.1 Origin of impurities and point defects in silicon

The quality of a silicon-based device considerably depends on the purity of the silicon crystal. The purity and the homogeneity are the main criteria of the crystal. However, in reality the crystal is never perfect. Three main sources of structural defects and impurities can be emphasized: 1) silicon alloy used for the crystal growth,

2) crystal growing method, and 3) operational environment.

2.1.1 Silicon alloys used for the crystal growth: silicon grades

Industry deals with three silicon grades: Metallurgical grade (MG-Si), Electronic grade (EG-Si), and Solar grade (SoG-Si). Lets briefly consider each of the grades.

MG-Si is the alloy, extracted form the silica (SiO_2) in an electric arc furnace. It is a result of the chemical reaction $SiO_2 + 2C \rightarrow Si + 2CO$, which occurs at temperatures higher than 1990 ℃. It is 99% (silicon 2N = 2 Nines) pure. It contains impurities like SiO_2, SiC, metals, dopants, and light elements and is, therefore, useless for the electronic and photovoltaic applications. Depending on the required application, particular purification is followed.

EG-Si is the alloy obtained from MG-Si. The purification process includes the gaseous phase of silicon. Several methods exist, among them, the "Siemens procedure" is the most popular. Very high temperature stages make this purification method extremely expensive. The purification includes the following reaction: $Si + 3HCl \rightarrow SiHCl_3 + H_2$. The fractional distillation separates $SiHCl_3$ from other components. Occurring in the gaseous phase, the inverse reaction liberates Si. Si then crusts on the multi-crystalline bar. Resulting alloy is a 99,9999999% (9N) pure silicon. However, the cost of EG-Si is relatively expensive compare to SoG-Si.

SoG-Si is the alloy also obtained by purification of MG-Si. Contrary to the EG-Si, gaseous phase is not involved in a process. The purification include the solid and the liquid phases only. The fabrication of SoG-Si from MG-Si involves a segregation and a plasma torch processing. The purity of the final material is much cleaner that in MG-Si, but much more dirty than EG-Si, and is fully determined by the quality of the cleaning steps.

The first step consists of the repeated melting and the controlled solidification of a silicon ingot. The crystal growing conditions and the affinities of the impurities with the solid and the liquid phase determine the concentrations of the impurities in the crystal. The impurities concentration in the liquid phase changes during the growth procedure. Hence, the impurities distribution along the crystal is inhomogeneous and characterizes by the segregation parameter. In thermodynamic equilibrium, it is determined as the ratio of the solubility of the impurity in solid, to its solubility in liquid: $k_0 = s_S/s_L$. If $k_0 \ll 1$, the impurity essentially stays in the liquid phase. Only the bottom part of an ingot contains more impurities of this type. It can be simply cut out. This is true for most metallic impurities (for ex. $k_0(\mathrm{Fe}) = 8 \cdot 10^{-6}$). But unfortunately, this is not the case for the light impurities and dopants (see Table

Impurity	k_0	Concentration [cm^{-3}]
B	0.8	$> 10^{13}$
P	0.35	$> 10^{13}$
O	0.25-1.25	$\sim 10^{16} - 10^{18}$
C	0.07	$\sim 10^{16}$
Ge	0.33	NA
Sn	0.016	NA

Table 2.1: The segregation parameter k_0 for some silicon impurities and their approximate concentrations in SoG-Si [57, 132].

2.1). The bigger is k_0 of the particular impurity, the more important content of this impurity will be in the crystal. In the general case, the thermodynamic equilibrium is unachievable. Thus the impurity concentration should be estimated by considering the effective segregation coefficient [18, 108]. However, the tendencies described above maintain essentially valid.

The second step, namely plasma torch processing, allows to remove some of the resting impurities after the segregation step. Despite these two purification steps, SoG-Si contains much more impurities than EG-Si: metals (Fe, Cr, Ti, etc), light elements (O, C, N, etc.), and dopants (B, P, Al, etc). Their approximate concentrations are given in Table 2.1. However, the advantage of the SoG-Si is its cheapness.

2.1.2 Crystalline silicon growth methods

The crystal growth follows the silicon alloy purification step. The crystal growth process can be another possible source of impurities and structural defects. The semiconductor industry deals with mono-crystalline, multi-crystalline, or mono-like silicon.

Monocrystalline silicon is usually grown by Floating Zone (FZ) or Czochralski (Cz) method. The FZ-Si allows to obtain an excellent quality mono-crystalline ingot. An induction coil locally melts the silicon ingot and is gradually moved from its bottom to the top. The procedure can be repeated until the desired quality is reached. The FZ method allows obtaining an excellent crystal quality. The concentration of the oxygen and carbon impurities is less than 10^{16} cm^{-3}. The principal impurity is copper, which is introduced due to the contact of induction coil with the silicon. The second method is the Czochralski method [30, 127] and is one of the most widespread industrial method for the growth of the silicon mono-crystals. Silicon alloy is firstly melted in a quartz crucible (SiO_2). The crystal growth starts when the seed rod is introduced into the melt. The rod and the crucible is slowly rotating in a opposite

directions, while the rod is pulled from the melt. The quartz crucible slowly dissolves into the melt, releasing a large quantity of oxygen. Most of the oxygen evaporates from the melt surface as a SiO gas, while the resting 1% stays in the melt and dissolves into the ingot. After being evaporated, SiO interacts with a hot graphite susceptor and forms carbon monooxide (CO). CO dissolves back into the silicon melt from the surface. At the end of the process, one gets a cylindric single crystal silicon, which orientation is determined by the seed rod. The main impurities of the Cz-Si are oxygen and carbon. Their concentrations are determined by the segregation coefficient and is usually of the order of $10^{17} - 10^{18}$ cm^{-3} for the oxygen impurity and of the order of $10^{16} - 10^{17}$ cm^{-3} for the carbon impurity [57].

Multicrystalline silicon 45% of the photovoltaic industry is based on multicrystalline silicon. The growth procedure is based on the controlled solidification of the silicon melt. Silicon alloy is put in a quartz crucible, covered by a silicon nitride (Si_3N_4) film. The latter reduces the oxygen incorporation to the melt from the crucible. The film also limits crack formation in the crystal. However it is a source of metallic impurities [58]. Once the silicon is melted and become a homogeneous substance, the solidification is started. Solidification is driven by the cooling of the silicon from the bottom to the top until full solidification. The multi-crystal consist of grains of different shape and size. It contains less oxygen that the Cz-Si, about $2 - 3 \cdot 10^{17}$ cm^{-3}.

Mono-like silicon The mono-like technology allows growing silicon crystal with large monocrystalline grains. The technology is based on the controlled bottom-top solidification of the crystal (as in the case of multicrystalline silicon). The difference is that we place one or several monocrystalline seeds on the bottom of the crucible. That allows producing big zones of mono-crystal. This growing method is cheaper than Cz-Si, although the quality is slightly reduced due to disclocations between monocrystalline zones and multicrystalline edges.

2.1.3 Specific operational environment

Particular operational environments can also lead to the formation of point defects in silicon. Often the semiconductor devices have to function in irradiation environments. For example, such conditions appear in the open space, during some medical procedures, or inside particle accelerators. The defect formation can be a desired effect, as in the case of particle detectors, or undesired, as in the case of the space or medical electronic devices. In particular, let us focus on the electron irradiation. This type of irradiation lead to a formation of a Frenkel pair. The Frenkel pair is made of a vacancy (V) and a self-interstitial (I), which are the intrinsic,

or structural, point defect of silicon. Both V and I are quite mobile and interact with impurities, forming a range of defect complexes.

Besides above discussed point defects origins, we consider one last way of their appearing. This is the deliberate introduction of an impurity. It can be realized through different techniques. In the case of dopants, desired elements can be introduced into an alloy before the growing process. It can be also done via ion implantations.

In the following section we will classify all these defects and briefly characterize them.

2.2 Defects classification

As it was previously summarized, it is hardly possible to avoid any kind of defects. The majority of the industrially produced silicon contains defects. Those can be structural defects (grain boundaries, dislocations, vacancies/interstitials) or impurities. All of them can affect the silicon's properties: mechanical, transport, electrical, optical, and others. As a result, defects impact the quality of the future devices. The impact can be negative: for example, some defects act as recombination centers. But they can sometimes positively affect the semiconductor properties. The p- or the n-type dopings change the majority carrier type and they are oFften desired.

That is why it is extremely important to investigate their behavior and their impact on silicon properties. Point defects were intensively studied both theoretically and experimentally [36, 106]. However there are still some lacks related to point defects interactions, which we aim to address in this thesis.

However, prior to emphasize the range of problems in this area, we will summarize and classify the point defects and briefly introduce their properties. Table 2.2 classifies the point defects and impurities according to their origin and effect on the electrical properties.

2.2.1 Extrinsic point defects (Impurities)

We start our description by the native point defect. By native point defects we mean those, which appear in the crystal due to the growth techniques. This include light impurities, metals, and p-/n-type dopants. Then, the isovalent dopants and the electron irradiation induced defects will be also briefly discussed.

Light impurities, such as oxygen, carbon, and nitrogen, are electrically neutral. However, by forming precipitates or defect complexes, they may directly affect silicon's electrical properties. The term "light impurities" is chosen for them as

Light impurities	Metals	Dopants p-type(pD)	Dopants n-type(nD)	Dopants isovalent (iD)	Primary radiation defects	Secondary radiation complexes	Associations of iD with radiation defects
Oi	Fe	B	P	C	V (V2)	VO	DSi_I
O2i	Cu	Al	As	Ge	Si_I	VO2	
	Ti	Ga	Sb	Sn			D_I
C	Co			Pb		V2O	
H	Ni					V2O2	DC
	Mo						
	Au					CiOi	DV
	...					CiO2i	
						CiOiI	DVO
						CsOi	
						CsO2i	
							...
						Ci	
						CiCs	
						CiCi	

Table 2.2: Possible defect complexes are grouped by their origin.

their atomic masses are lighter than that of silicon. C impurity also belongs to the isovalent impurities group.

Metals introduce deep energy levels, close to the middle of the band gap. That is why they act as recombination centers. As a result, the metal impurities reduce free carrier lifetime in photovoltaic or microelectronic devices. Metallic defects can occupy substitutional or interstitial positions. Most of the metal elements can be excluded from the crystal via repeated segregation technique. The resting metallic elements can be eliminated by the so-called internal gettering process [4]. In other words, oxygen precipitates capture and deactivate the metallic impurities, so that there is less of them in the active crystalline zone.

p- and n-type dopants are highly soluble in silicon crystal (in solid phase of silicon). They usually substitute the silicon atoms in the crystal sites. Being the elements of the III and V column of periodic table, they significantly affect semiconducting properties of the silicon by introducing shallow levels in the band gap. p-type dopants consist of B, Al, and Ga, while n-type dopants consist of P, As, and Sb. B and P are the most widely used dopants, as far as they are naturally present in important concentrations in the MG-Si. These elements are often desired as they lead to a certain conductivity type. However, their presence causes sometimes to detrimental effects. For instance, B presence leads to a Light Induced Degradation (LID) of the solar cells [12].

Isovalent dopants include the elements of the IV column of the periodic table, namely C, Ge, Sn, and Pb. Usually, these elements occupy a substitutional position in the crystal. As far as they have four valence electrons they are electrically neutral. Hence, they introduce no levels in the band gap and do not affect the carrier lifetime. However, these elements' sizes differ from that of silicon. As a result, they introduce long-range elastic fields. Their presence in significant concentration of $> 10^{20}$ cm^{-3} changes the cell parameter of the silicon crystal. Similar to the light impurities, they are electrically neutral, but they can form electrically and optically active complexes when associated with other impurities and point defects.

Irradiation induced defects The most important irradiation induced point defects are vacancies and self-interstitials. They can be introduced in small quantities during the growth process. However, electron irradiation may cause their presence in significant concentrations. In this thesis we will consider the electron irradiation induced defects. We classify them into two subgroups, namely primary and secondary radiation defects. The *primary radiation defects* are vacancies and self-interstitials.

The *secondary radiation defects* are the whole range of possible combinations of primary radiation defects with each other and with other impurities.

In this section, we have summarized and structured the point defects and point defect complexes in crystalline silicon. From now, we start the discussion in more detail the problematics, that will be treated in the present thesis.

2.3 Problematics

2.3.1 Inter-defect interactions

The defects intensively interact with each other. One can conventionally distinguish 2 types of interaction: short-range and long-range interactions.

A defect complex is formed as a result of the *short-range interaction*. The complex is a localized defect and its properties usually differ from the properties of its components. Each complex affects the crystal properties in its own way. For example, most of the secondary electron irradiation induced complexes introduces deep levels in the bandgap. VO_i and C_iO_i are thought to act as recombination centers and thus can lead to a severe degradation of the electronic device properties [16, 61]. As a result of the *long-range interaction*, no complex is formed. The interaction happens through the long-range fields, such as electric, elastic, and magnetic fields. The defects properties, their behavior, and the way they affect silicon, can be modified. For example, the solubility of the lead (Pb) atoms in silicon can be increased by carbon (C) incorporation.

In this work we deal with both long- and short-range interaction types. The change in oxygen kinetics properties is an example of the long-range interaction, while the secondary radiation induced complexes are examples of the short-range interaction. In the resting part of this chapter, we point out the background and the open questions related to the two interaction types. We organize the background information and open questions in the order they appear in the next chapters. The titles of the chapters reflect the titles of the background items. Here, we will mostly focus on the experimental aspects of the problems, while the necessary methodological and theoretical insights are given in the methods and the results chapters, respectively.

2.3.2 Oxygen kinetics in heavily doped silicon

Oxygen is a particular impurity, as it is almost always presented in crystalline silicon in concentrations of $10^{16} - 10^{18}$ cm^{-3} [95]. Its impact on silicon-based devices is ambiguous. On one hand, it does not affect the electrical properties of silicon and improves the mechanical strength of the crystal; oxygen precipitates getter the

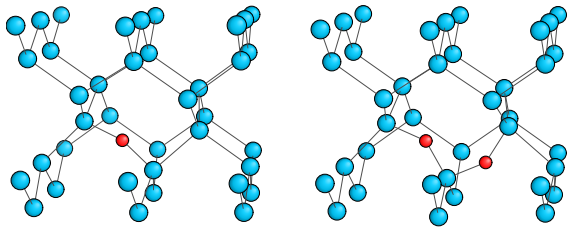

(a) O_i (b) O_{i2}

Figure 2.1: The schematic geometry configuration of oxygen monomer (a) and dimer (b).

undesired metallic impurities [128]. On the other hand, the so-called Thermal Donors [51] are related to the oxygen agglomerates formation; some oxygen containing defects (such as V-O, C-O, B-O complexes) act as a recombination centers and reduce the solar cells efficiency [12, 119]. Famous boron oxygen complex is responsible for the Light Induced Degradation of the solar cells [42, 116, 12, 134]. Both the exact composition of the defect and its formation mechanism are still discussed [2, 134, 116]. However, one can infer the importance of precise knowledge of oxygen diffusing properties for all mentioned phenomena.

The oxygen diffusivity depends on the temperature range, as well as on the concentrations of the dopants and the impurities presented in silicon. In low doped silicon, one can distinguish two temperature modes:

— high temperatures, above 700 ℃ and below the silicon melting temperature $\sim$ 1400 ℃;

— low temperatures, 300-700 ℃.

At the high temperatures, we observe the so-called ‵normal″ diffusion, which diffusion coefficient can be described by the following empirical expression [60]:

$$D(O) = 0.13exp(-\frac{2.53eV}{kT})cm^2s^{-1}. \tag{2.1}$$

In this case, an interstitial oxygen monomer is the particle responsible for the oxygen transport (see Figure 2.1(a)).

At the low temperatures, an enhanced oxygen diffusion is observed. The enhancement was associated with an activation energy of 1.5 eV [70, 88, 117], whereas the dimer is thought to be the responsible diffusing species [46]. However, stress induced dichroism experiments, which is sensitive to only single oxygen atoms jumps, have shown that monomers diffusion coefficient is also described by the extrapolation of Expression (2.1) [60].

While the oxygen diffusivity is not affected by the low doping rates, it turned to be sensitive to heavy doping, when the dopant concentration is equal or greater than

that of oxygen [93, 139, 138]. Gathered during the past two decades, the number of experimental evidences had revealed certain trends, summarized in Table 2.3. Let's consider the reported effects of p-type, n-type, and isovalent dopants on the oxygen diffusivity one by one.

p-type doping. At the low temperatures, experiments show sometimes contradictory trends. Most of the studies suggests the enhanced oxygen diffusion in heavily doped p-type silicon. The first indirect evidence was the observation of an enhanced Thermal Donors formation, as reported by Wada *et al* [136]. Recent Dislocation Locking (DLT) experiments suggest an oxygen transport increase by a factor of at least 8 [139, 93], compared to low doped material. An enhanced kinetics of oxygen precipitation [138], which occurs in heavily B-doped material, also supports the evidence of the enhanced oxygen diffusivity. However, some earlier Secondary Ion Mass Spectroscopy (SIMS) outdiffusion profiles showed a reduced diffusivity in heavily B-doped samples at 600-800 ℃ by a factor of 2 to 5 [126]. At high temperatures, B-doping leads to either very weak or no impact on the oxygen diffusion and precipitation kinetics [99, 138].

n-type doping. There are few evidences of the reduced oxygen diffusion in the heavily n-type doping in the low temperature range. Phosphorus doping reduces the thermal donors formation, according to Wada *et al* [136]. Both the heavily arsenic-doped and the antimony-doped samples slow the oxygen diffusion, as revealed by Takeno *et al* [126], by increasing its migration energy by 0.64-0.68 eV and 1.4 eV, respectively. Dislocation locking experiments show the slowing of the oxygen diffusivity by a factor of 5 in the heavily As-doped silicon [139]. However, no dependence of the diffusivity was found in the antimony doped silicon with the DLT experiment [93].

Isovalent doping. Doping with germanium slows the oxygen diffusivity by the factor of 4 according to Zeng et al. in the low temperature range [139]. As far as the Stress Induced Dichroism (SID) technique is only sensitive to the oxygen monomer diffusion, it was shown that the increasing germanium content is slowing more the monomers diffusion at 375 ℃ [62].

To summarize, p-type, n-type, and isovalent doping have an impact on the oxygen diffusivity at the low temperatures. As it was earlier concluded in Reference [139], experimental evidences suggest that both internal strain and change in Fermi energy level can cause the changes in kinetic properties of oxygen. For example, high germanium content introduces relatively important change in the lattice parameter ($\frac{\Delta a}{a} = +7 \times 10^{-5}$) of silicon without affecting its electrical properties, while high

Dopant	Concentration [cm^{-3}]	Temperature	Effect on oxygen transport	Technique and sensitivity	References
B	$8.0 \cdot 10^{18}$to$1.2 \cdot 10^{19}$	1050 ℃	None	SIMS - effective	[99]
B	$8.0 \cdot 10^{18}$to$1.2 \cdot 10^{19}$	800 ℃	Slows (factor of ~ 5)	SIMS - effective	[99]
B	$4.4 \cdot 10^{18}$	500 and 800 ℃	None	SIMS - effective	[126]
B	$4.4 \cdot 10^{18}$	600 to 700 ℃	Slows (factor of ~ 5to3)	SIMS - effective	[126]
B	$2.7 \cdot 10^{18}$to$8.0 \cdot 10^{18}$	350 to 550 ℃	Enhances (factor of ~ 40)	DLT - effective	[93]
B	$30. \cdot 10^{18}$	350 to 550 ℃	Enhances (factor of $\sim$ 8to25)	DLT - effective	[139]
Ge	$1.0 \cdot 10^{16}$to$1.0 \cdot 10^{20}$	1050 to 1200 ℃	Enhances	SIMS - effective	[23]
Ge	$5.0 \cdot 10^{20}$to$2.7 \cdot 10^{21}$	375 ℃	Slows (more with increasing [Ge])	SIMS - effective	[62]
Ge	$8.0 \cdot 10^{19}$	400 to 700 ℃	Slows (factor of $\sim$ 1.25to3.3)	DLT - effective	[139]
As	$1.1 \cdot 10^{19}$	1050 ℃	None	SID - monomers	[99]
As	$1.1 \cdot 10^{19}$	800 ℃	Slows (factor of ~ 2.5)	SIMS - effective	[99]
As	$4.0 \cdot 10^{18}$to$1.3 \cdot 10^{19}$	400 to 700 ℃	Slows (E_a increased by 0.64 to 0.68 eV)	SIMS - effective	[126]
As	$2.0 \cdot 10^{19}$	400 to 700 ℃	Slows (factor of $\sim$ 1.1to5)	DLT - effective	[139]
Sb	$5.0 \cdot 10^{20}$to$2.7 \cdot 10^{21}$	950 to 1100 ℃	None	SIMS - effective	[100]
Sb	$5.0 \cdot 10^{17}$	800 to 1050 ℃	None	SIMS - effective	[99]
Sb	$1.3 \cdot 10^{18}$	600 to 800 ℃	Slows (E_a increased by 1.40 eV)	SIMS - effective	[126]
Sb	$8.0 \cdot 10^{17}$	450 to 550 ℃	None	DLT - effective	[93]

Table 2.3: Reported effects of hight concentration of various dopants on the transport of oxygen in Cz-Si [139]. We denote SIMS: Secondary Ion Mass Spectroscopy; DLT: Dislocation Locking Technique; SID: Stress Induced Dichroism.

content of the p- and n- type dopants change the Fermi energy level of the crystal. As it was reviewed above, both cases are known to impact the oxygen diffusivity properties.

It is also evident, that experimental techniques employed to measure the diffusivity has a significant impact on the obtained trends. That is why additional studies are necessary to decipher the underlying mechanisms of enhance or retarded diffusion of oxygen species in the silicon crystal.

Significant efforts were made in order to understand the mechanisms lying behind the observed changes in oxygen diffusivity. For example, other diffusing particles, such as VO, IO, molecular O_2 [47], chains of more than 3 interstitial oxygens [71], were proposed as a diffusing species. It was shown that they can barely be involved in oxygen transport [29, 125]. Dimers diffusion in doubly charged state is an alternative possibility for an enhanced transport proposed by Adey *et al* [3, 37]. However, no signs of charged dimers were yet observed [92]. Another explanation for the enhanced diffusion is the so-called Bourgoin-Corbett mechanism [13, 14, 101]. Such mechanism is based on the fact, that the ground state configuration of the neutral oxygen dimer becomes the saddle point of the doubly charged state, whereas the saddle configuration of the neutral dimer becomes the ground state. The mechanism suggests that the oxygen dimer captures and releases one or two electrons and diffuses with a very low activation barrier or even nearly barrierless, which contradicts the experimental observations [46, 93, 139].

To summarize, no satisfactory explanation has been yet proposed for the enhanced and retarded oxygen diffusion in heavily doped silicon. That is why we aimed to investigate this aspect and decipher the enhanced-retarded mechanisms of the oxygen diffusion in heavily doped silicon.

2.3.3 Secondary radiation defects in Cz-Si

The second particular topic, that is discussed in this thesis is the irradiation induced defects in Cz-Si. The principle damage caused by electron irradiation is the formation of a Frenkel pair. The Frenkel pair consists of a silicon self-interstitial (I), the silicon atom knocked off from its formal position, and the resulting vacancy (V). Those are primary radiation defects (see Table 2.2 Column 6). In the course of the irradiation, more and more Frenkel pairs are formed. The vacancies and the self-interstitials diffuse and promptly interact with other point defects and impurities. Those are secondary radiation defects (see Table 2.2 Column 7).

As it was already mentioned, Cz-Si contains oxygen and carbon impurities, which are introduced in the crystal during the growth process. During the irradiation course, the primary radiation defects will thus interact with these impurities. Once

the vacancy encounters an oxygen, they bind together and form vacancy oxygen complex (VO), the so-called A-center. The self-interstitials rather interacts with a carbon atom and form the fast-diffusing carbon interstitials (C_i). C_i diffuses through the crystal until it encounters an oxygen or a substitutional carbon and forms carbon oxygen C_iO_i or carbon-carbon C_iC_s complex. Thus, the concentration of these complexes depends on the irradiation time, the temperature, and the impurities concentrations. Moreover, further interactions of the primary radiation defects with these complexes produce bigger aggregates, consisting of three or more compound atoms.

The complete understanding of the electron irradiation induced complexes is of extreme importance. Firstly, the irradiation damage together with the implantation of certain dopants and impurities allows producing material with specific characteristics. Secondly, it provokes the formation of the defects and complexes in considerable concentrations. That makes them visible for experimental techniques. Finally, the radiation induced complexes are of extreme importance for the applications operating in specific environments. The list of such applications includes: dosimetry, particle detection, medical equipment, satellite equipment, and space station equipment.

Among the range of experimental techniques, the infrared (IR) absorption [6, 48] is the most suitable technique for the point defects identification. It allows identifying defects through their Localized Vibrational Modes (LVM), set of which are unique for each defect and sometimes referred as vibrational fingerprints. The concentration of the defect is proportional to the intensity of the related band. The proportionality coefficient k_{cal} has to be calibrated for each defect using the cross-analysis with other techniques. Table 2.4 lists the calibration coefficients for some defects of the irradiated Cz-Si.

Defect	IR band $[cm^{-1}]$	$k_{cal}[10^{17}cm^{-2}]$	References
O	1106	3.14	[5]
C	606	1.0	[114]
VO	830	0.625	[33]
VO_2		0.313	[79, 73, 80]
C_iO_i	860	1.1	[33]
C_iO_iI	(940;) 1024	0.38	[33]
C_iC_s (B form)	544	(0.015)0.42	[67]

Table 2.4: The calibration coefficients for some point defects in irradiated Cz-Si.

The irradiation induced point defects in Cz-Si have been widely studied. Most of related complexes are identified as well as their properties. Unfortunately, the full microscopic insight cannot be derived solely from the IR absorption experiments. The reasons for that is listed below.

1. LVM of many complexes are not yet identified.

2. Even if the defect or a complex exists, its bands can be sometimes invisible. They can be shadowed by another band or can be out of the detection range or can be under the detection limit.
3. Superposition of two bands may obscure the obtained concentrations.
4. LVM of heavy point defects (heavier than the mass of silicon atom) are superposed with the vibrational frequencies of the bulk silicon.

Some of these difficulties can be overpassed employing theoretical simulations. However, there is still a lack of a precise and effective tool to describe and to predict the defect complexes formation and their temperature evolution in the irradiated material.

Theoretical description of the defect complexes formation and evolution requires three parameters:

— The formation energy, the energy to produce a defect, such as structural point defect(V or I) or charged particles.
— The binding energy of the complex, the energy gain when the two parts of a complex bind together.
— The migration energies of the components and the complex itself, the energy of the barrier, that a species need to overpass to reach the neighboring site.

These parameters can be calculated with *ab initio* methods. However, the further analysis is required to investigate the competitive processes and temperature evolutions. Two most frequently used methods are the Monte Carlo (MC) and the Mass Action Law (MAL) techniques. MC provides a precise kinetic picture, however requires a significant amount of time and computational sources. The second is fast and effective, but only describes the thermodynamic equilibrium and misses the kinetic aspects. The third method is the kinetic mass action law (KMAL). KMAL combines the advantages of both techniques, and is able to provide the temperature evolution of point defects by taking into account both thermodynamic and kinetic aspects.

In this work, we aimed to perform the mixed experimental and multi-scaled theoretical analysis of the irradiated Cz-Si. The theoretical results will be compared with the results of the IR experiments.

2.3.4 Secondary radiation defects in isovalently doped silicon

As it was previously mentioned, some of the secondary irradiation complexes are undesired as they reduce the performances of electronic devices. For example, VO and C_iO_i complexes introduce deep levels in the silicon bandgap, which lead to a severe degradation of Si-based devices. In contrary, some defects are advantageous

as they enhance the performance of the Si-based devices. For example C_iC_s complex can be used to obtain an optical gain and stimulated emission. That is why we do not necessarily need to suppress, but we rather need to control the defect complexes formation in Si.

The use of isovalent doping is a possible defect engineering strategy in order to achieve such a goal. Previously, number of IR absorption studies have been performed to investigate the impact of Ge, Sn, and Pb on irradiation caused defects [24, 25, 63, 75, 77, 78, 83, 81], therefore here we will introduce a short summary of most important trends in Ge, Sn, and Pb isovalently doped silicon. We will focus on the imact of isovalent doping on formation and thermal stability of main electron irradiation induced pairs, namely VO_i, C_iO_i, and C_iC_s.

Ge doping. The Ge doping leads to an enhanced production of all three pairs, i.e. VO_i, C_iO_i, and C_iC_s [77]. While thermal stability of C_iO_i and C_iC_s complexes has not been affected, that of VO_i is found to be reduced [78]. In addition, the reduced amount of VO complex is converted to VO_{i2} defects in Ge presence [79].

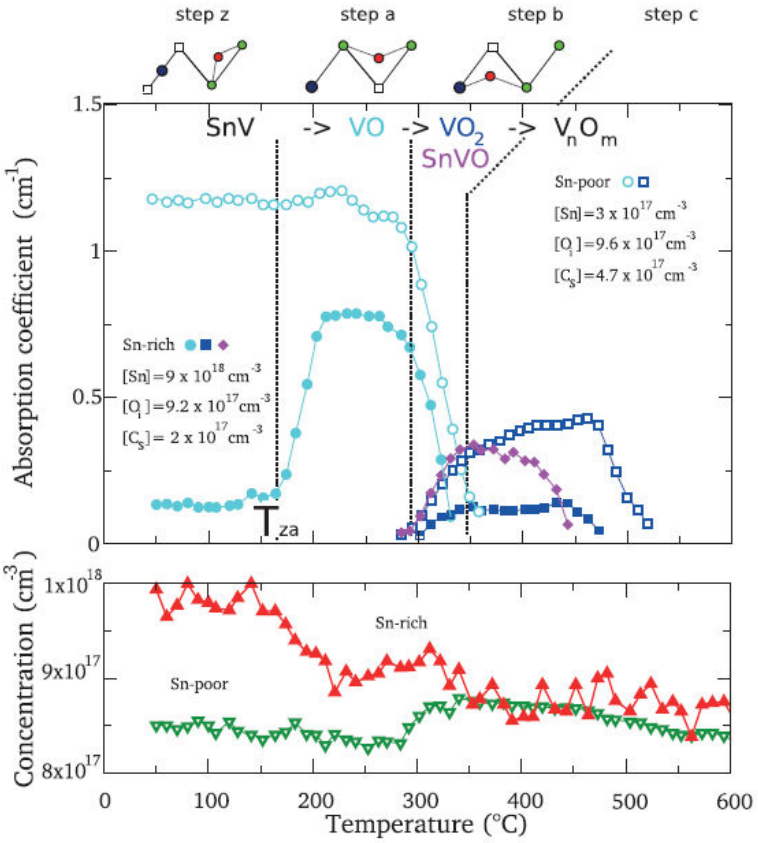

Figure 2.2: From reference [24].

Sn doping The Sn doping strongly impacts the VO_i pairs formation in the electron irradiated material [24]. As demonstrated in Figure 2.2, VO_i pair production is fully

suppressed in Sn-reach silicon sample during the irradiation course. However, the VO_i pairs emerge upon isochronal annealing at the $\sim 200 - 350$ ℃ temperature range, but their concentration is significantly reduced compare to the Sn-poor Si.

Pb doping . The Pb doping have been studied by electrical measurements. The measurements have suggested a partially suppressed production of both VO_i and C_iC_s pairs in the Pb doped silicon [31, 94]. However, the situation is less clear concerning other aspects: the C_iO_i defect production and all three pairs stability have not been investigated yet. No reports have been published on the $VO_i \rightarrow VO_{i2}$ conversion ratio.

In this thesis, we aimed to perform a systematic investigation of the irradiated isovalently doped and isovalently co-doped silicon. This is why we aimed the systematic experimental insight by means of IR absorption experiments as well as exhaustive theoretical study of possible defect complexes by means of DFT calculations.

2.3.5 Optical properties of C-C complex: G-center

C_iC_s is one of the secondary irradiation induced defects. The pair is associated to the light emitting G-center [8, 7]. The G-center is lasing at 0.97 eV (1280 nm) as illustrated in Figures 2.4 and 2.3. It was discovered in the 60's as a by-product in the silicon crystal caused by the radiation damage from the bombardment with high energy electrons, ions and gamma rays. In recent years, an important effort has been made in order to increase the G-centers concentration [90, 8, 7]. The methods are generally based on the silicon surface alteration, followed by a laser annealing. These technologies have promising applications in development of a silicon laser.

The structure of the C_iC_s pair has been debated for almost 40 years. Its configuration has been investigated by experimental as well as by theoretical techniques [17, 98, 121, 67, 69, 22, 66]. The summary of the experimental and theoretical studies on carbon-carbon complexes is listed in Table 2.5.

Two forms of carbon-carbon complexes, namely A and B forms, have been identified experimentally. Their vibrational modes have been experimentally obtained and are listed in Table 2.5. The G-centre is thought to be the B form of the C_iC_s pair. From the theory point of view, both A and B forms were found to be stable with a binding energy about $\sim 0.8 - 1.3$ eV [87, 141, 35]. The localized vibrational modes have been reproduced for the neutral and charged states for both forms [35, 69, 22].

Despite the A and B forms of C_iC_ss complex, there are one more experimental and one more theoretical investigations, which suggest C-C pair configurations, different from both A and B forms.

Technique	Property	Main results	References
Experimental works			
EPR	Structure	2C oriented in $\langle 111 \rangle$ in a V	[17]
ODMR	Structure	A- and B- forms	[98]
EPR, DLTS, PL	Charged states of A- and B-forms	A form is more stable than B form for all charge states, except neutral	[121]+ refs. therein
IR	LVM	A form: 594.6, 596.9, 722.4, 872.6, 953.0 cm^{-1} B form: 540.4, 543.3, 579.8, 640.6, 730.4 and 842.4 cm^{-1}	[67]
EPR	Configuration	Conf. 1: I + 2 identical C - monoclinic symmetry Conf. 2: I + 2 identical C - triclinic symmetry	[66]
PL	Optics	G-centre	[8]
PL	Optics	G-centre	[7]
Theoretical works			
ab initio	LVM		[69]
ab initio	LVM		[22]
ab initio	Structure	C-form: 2C oriented in $\langle 100 \rangle$ in a V	[74]
ab initio	C-form (NSP)	$E_b(\mathrm{B}) < E_b(\mathrm{A}) \sim E - b(\mathrm{C})$	[87]
ab initio	C-form (NSP)	$E_b(\mathrm{B}) < E_b(\mathrm{A}) < E - b(\mathrm{C}) <$	[35]
ab initio	Structure (SP)	$E_b(\mathrm{C}) < E_b(\mathrm{B}) < E - b(\mathrm{A}) <$	[141]

Table 2.5: The summary of experimental and theoretical studies of C_iC_s complex. We use following notations: EPR - Electronic Paramagnetic Resonance; ODMR - Optical Detection of Magnetic Resonance ; DLTS - Deep Level Transient Spectroscopy; PL - Photoluminescence; IR - Infrared spectroscopy.

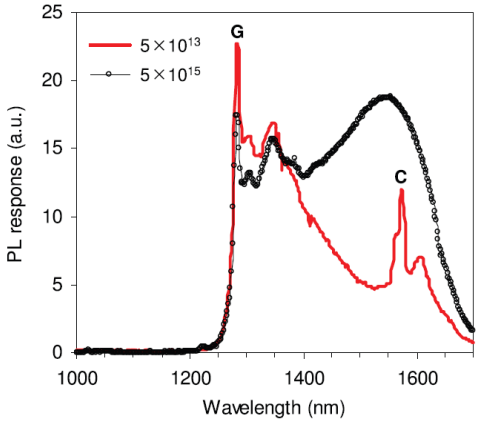

FIG. 1. Photoluminescence spectra, observed at 80 K, of pre-amorphised silicon samples A03 and A05 (2×10^{20} C cm^{-3} irradiated with 5×10^{13} and 5×10^{15} H$^+$ cm^{-2}, respectively). The positions of the G- and C-centres are also shown.

Figure 2.3: Experimental data from Reference [8].

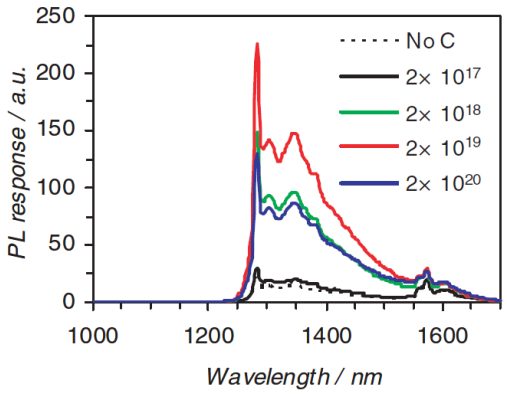

Figure 2. Photoluminescence spectra measured at 80 K of silicon samples implanted with different carbon doses and annealed at 1000 °C for 20 s, followed by proton irradiation at 5×10^{13} cm^{-2} at 2 MeV. The carbon concentrations (cm^{-3}) are indicated.

Figure 2.4: Experimental data from Reference [7].

In 2002, Laiho *et al* [66] used the spin-dependent microwave photoconductivity detection of EPR and detected a new low-symmetry configuration of a complex containing an interstital silicon and two identical carbon atoms. The Si-PT4 is not identified so far. It arises while the Si-PT1 (B-form of C_iC_s) goes down during annealing. The complex responsible for Si-PT4 contains two equivalent carbon atoms and one silicon atom (analogous to the B-form of C_iC_s). The Si-PT4 spin-1 EPR line (monoclinic symmetry) transforms at temperatures below 20 K to the new spin-1 spectrum Si-WL5 (triclinic symmtery).

Theoretical calculations predict the third form of the CiCs pair, denoted here as a C form. The complex has been initially proposed by Liu *et al* [74] and Mattoni *et al* [87] in 2002. And then reconsidered in more recent theoretical investigations [35, 141]. The spin-polarized calculations suggested the stable complex with binding energy of 1.28 eV [141], while the non-spin-polarized calculations suggested slightly lower value. The complex has never been experimentally observed.

In this thesis we aimed to clarify the configurational properties, as well as the relation of the complex with G-centre. In this work we focus on structural, vibrational, and optical properties of this pair, while we keep apart the problems of the complex formation and all the kinetic aspects for the future investigations.

2.4 Summary

In this Chapter, we have summarized the state of the art in the field of point defects in crystalline silicon. We pointed out the main open questions which will be studied later in this thesis. The first problem is related to the impact of heavy doping on the oxygen diffusivity at low temperature regime (see Chapter 4). The

second problem is related with the secondary irradiation induced complexes in isovalently doped and co-doped Cz-Si (see Chapter 5). The last one consists in detailed investigation of C_iC_s complex forms. Particularly, we intend to assign one of these forms to the light-emitting G-centre.

Chapter 3

Computational Methodology

Among the atomistic simulation tools, Density Functional Theory (DFT) approach is of particular interest for the current study. It combines the fundamental quantum precision with an acceptable computational cost. DFT deals with the total energy of a system, which is the most fundamental property of any atomic system. Moreover, it is also possible to deduce some important observables, including some thermodynamic, kinetic, and vibrational characteristics of the system under investigation.

In this chapter, we introduce the insight into the DFT basic concepts. Along with the theoretical background, we consider the important ingredients of DFT: exchange correlation functional, pseudopotentials, the basis set functions, and the geometry optimization techniques. These are of a significant importance for the practical use of DFT.

A particular attention will be payed on point defect simulations within DFT. We will discuss the periodic boundary conditions, suitable for investigations of point defects as well as related observables. We will also provide some details on the vibrational property calculations of a point defect surrounded by bulk silicon.

Despite its powerfulness, DFT fails in describing the excited state properties. Hence, to study the optical properties of a system, we employed the GW approximation. In this chapter, we will not provide the theoretical background for this approximation, however, we refer the reader to Chapter 6. A brief description of method and tools, employed to calculate the excited state properties, are presented there along with obtained results and discussion.

3.1 Density Functional Theory related concepts

In this thesis, we will calculate the electronic properties of atomistic systems of a few hundreds of atoms, namely periodic Si supercell including one or two point defects in it. This is an atomistic structure, which is only a few nanometers big.

3.1.1 Schrödinger equation and Hartree-Fock Theory

To investigate the microscopic properties of an atomistic system, for example as one described just above, one needs to resolve a time-independent quantum mechanical Schrödinger equation for all electrons and ions of the system:

$$\hat{H}\Psi = E\Psi, \tag{3.1}$$

where the Hamiltonian $\hat{H}$ can be represented as a sum of the kinetic (T) and the potential (V) operators of the electrons (e) and ions (i):

$$\hat{H} = T_e(\vec{r}) + T_i(\vec{R}) + V_{i-i}(\vec{R}) + V_{e-i}(\vec{r},\vec{R}) + V_{e-e}(\vec{r}), \tag{3.2}$$

Here $\vec{r} = \{\vec{r_\alpha}\}_{\alpha=1,...,N_e}$ and $\vec{R} = \{\vec{R_A}\}_{A=1,...,N_i}$ denote coordinates of electrons and ions, respectively.

The Schrödinger equation can be exactly solved only for several simplest systems; for more complex systems, it is impossible to integrate the Schrödinger equation and thus to obtain its exact analytic solution.

Therefore, a number of useful approximations is usually employed to simplify the problem. In this chapter, we will describe some useful approximations, theories, and techniques which make possible the first principles calculations of big and complex systems.

Primarily, we employ the Born-Oppenheimer approximation. It assumes, that nucleus and electronic wave functions are independent variables and hence the total wavefunction $\Psi(\vec{r},\vec{R})$ can be denoted as the multiplication of its nucleus and electronic part $\Psi(\vec{r},\vec{R}) = \chi(\vec{R})\psi(\vec{r},\vec{R})$. As mass of the nucleus is much greater than that of the electron $m_i \gg m_e$, the electrons can immediately adjust to any nuclei orientation. Thus, we can consider the nuclei as classical particles and solve the equations for the electrons only. $\hat{H}_e$ then depends only on the nuclei positions:

$$\begin{aligned} \hat{H}_e &= T_e(\vec{r}) + V_{e-i}(\vec{r},\vec{R}) + V_{e-e}(\vec{r}) \\ &= -\hbar^2 \sum_\alpha \frac{1}{2m}\nabla^2 - \sum_{\alpha,A} \frac{e}{4\pi\varepsilon_0}\frac{Z_A}{|r_\alpha - r_A|} + \sum_{\alpha>\beta} \frac{e^2}{4\pi\varepsilon_0}\frac{1}{|r_\alpha - r_\beta|}. \end{aligned} \tag{3.3}$$

Taking into account the Pauli principle as proposed by Fock to describe the manybody wavefunction in a Slater determinant form $\Psi_S = \frac{1}{\sqrt{N}} det|\phi_\alpha(\vec{r})|$, one obtains the Hartree-Fock equation. The derived energy becomes a functional of the orthonormal single electron wavefunctions and can be expressed in the following form:

$$E_e^{HF}[\phi_1, ..., \phi_N] = \langle \Psi_s | \hat{H}_e | \Psi_s \rangle = \sum_{m=1}^{N} \langle \phi_m | - \frac{\hbar^2}{2m_e} \nabla^2 + v^{ext}(r) | \phi_m \rangle + \sum_{n>m=1}^{N} \{ \langle \phi_n \phi_m | \frac{e^2}{r_{nm}} | \phi_n \phi_m \rangle + \langle \phi_n \phi_m | \frac{e^2}{r_{nm}} | \phi_m \phi_n \rangle \}. \tag{3.4}$$

Here, $v^{ext}(r) = -\sum_A \frac{Z_A}{|r - r_A|}$ denotes the summarized external potential from the nuclei of the system. The last term denotes the Coulomb and the Exchange contributions of the electron-electron interaction.

The variational principle is used to find the minimum of the energy functional, which corresponds to the ground state of the system of interest.

The problem can be solved numerically. However, the computational effort scales exponentially with system size and systems of only several tens of atoms can be treated.

3.1.2 Density Functional Theory

To overpass the latter difficulty, Kohn and Hohenberg developed the Density Functional Theory (DFT) which was further extended by Kohn and Sham.

The key statement of the DFT is based on the fact, that the fundamental properties of the system of interacting particles can be expressed via the functional of the electronic density $n(\vec{r})$. Due to this reformulation, the many-body problem can be significantly simplified. Instead of dealing with many-body wavefunctions, depending on 3N spatial coordinates, in density functional theory we deal with the electronic density depending on only 3 spatial spacial coordinates.

The essence of the theory is the proof that the electron density $n(\vec{r})$ is a unique functional of the many-body wavefunction Ψ, and, therefore, the energy E is uniquely defined by $n(\vec{r})$.

Two theorems of Hohenberg and Kohn connect the electronic density and the external potential of the system.

Theorem 1. For a system of N_e interacting electrons in an external potential $v^{ext}(\vec{r})$, this potential is uniquely determined (up to an additive constant) by the electronic ground-state density $n_0(\vec{r})$.

Theorem 2. The functional $E[n]$, which delivers the ground state energy of the system for a given $v^{ext}(\vec{r})$, delivers the lowest energy if and only if the input density is the true ground state density $n(\vec{r}) = n_0(\vec{r})$.

The proofs of the theorems imply that the energy of the system can be represented as an electronic density functional:

$$E[n] = T_e[n] + V_{e-i}[n] + V_{e-e}[n]. \tag{3.5}$$

Unfortunately, the proofs of these theorems are not providing a practical scheme to find the correct ground-state energy. The problem is that although it is possible to exactly determine the V_{e-i} term as functional of electronic density $\int v(r) \cdot n(r)dr$, the kinetic and electron-electron interaction term cannot be directly expressed as a functional of $n(r)$.

The practical technique to calculate the density functional was developed by Kohn and Sham. The Kohn-Sham technique is based on two main assumptions:

1) The exact electronic density of the ground state can be substituted by the electronic density of noninteracting electrons in the following form:

$$n(\vec{r}) = \sum_{j=1}^{N_e} |\phi_j(\vec{r})|^2. \tag{3.6}$$

2) The energy functional can be expressed in the following form:

$$E[n] = T_e^{free}[n] + V_H[n] + E_{xc}[n], \tag{3.7}$$

where the first term is the kinetic energy of the noninteracting electrons; the second term is the Hartree potential, which accounts the Coulomb interaction of an electron with ions and surrounding electrons; and the last term accounts for remaining contribution. The latter term can be determined as a difference between the exact ground state energy and functional $E_{xc} = E^{exact} - E[n]$.

As it is impossible to define the kinetic energy term directly as a function of the charge density, it is necessary to break it into a set of orthonormal orbital functions. Then, the kinetic energy T_e^{free} of the non interacting system can be expressed as a functional of the single electron wavefunctions ϕ_i^{KS}.

$$T_e^{free} = -\frac{1}{2}\sum_{i=1}^{N} \int \phi_i^{KS}(r)\nabla\phi_i^{KS}(r)dr \tag{3.8}$$

In this approximation each electron moves in the effective single particle potential, which includes 3 components

$$v_{eff}(r) = -\sum_A \frac{Z_\alpha}{|r - R_A|} + \int dr' \frac{n(r')}{|r - r'|} + \frac{\delta E_{XC}[n]}{\delta n(\vec{r})}. \tag{3.9}$$

Here the first term describes the total potential of nuclei, whereas the second and the third ones describes the potential of all other electrons with a charge density $n(r)$.

To determine the ground state wavefunctions ϕ_i^{KS}, one should minimize the energy with respect to constrains on the basis set functions. More precisely, the Kohn-Sham orbitals should be maintained orthogonal and normalized. This can be

done by adding the Lagrange multiplier μ and minimizing the whole expression:

$$\delta\{E[n] + \mu[\int n(\vec{r})d\vec{r} - N]\} = 0 \tag{3.10}$$

Differentiation of Equation (3.10) with respect to $\phi^*_\lambda(\vec{r})$ (the star indicates a conjugation) gives the equation for the wavefunction j:

$$(-\frac{1}{2}\nabla^2 - \sum_\alpha \frac{Z_\alpha}{\vec{r} - \vec{R}_\alpha} + \int d\vec{r'}\frac{n(\vec{r'})}{|\vec{r} - \vec{r'}|} + \frac{\delta E_{XC}[n]}{\delta n(\vec{r})})\phi_j(\vec{r}) = \epsilon_j\phi_j, \tag{3.11}$$

where j runs over the spatial indexes and spin. The average electron density is determined as

$$n(\vec{r}) = \sum_j |\phi_j(\vec{r})|^2. \tag{3.12}$$

Equations (3.11)-(3.12) are so-called self consistent field equations or Kohn-Sham equations. Equation (3.11) is a single-particle Schrödinger equation for the noninteracting electrons, which moves in the effective external potential field $v_{eff}(\vec{r})$.

3.1.3 Exchange-correlation functionals

Generally speaking, the exact formulation of the exchange-correlation term of the energy is unknown. Therefore, an appropriate approximation should realize the Kohn-Sham theory in practice. The simplest one, but still one of the most remarkable ones, is the Local Density Approximation (LDA) [64]. Within the LDA, the exchange-correlation energy of an inhomogeneous system is locally approximated with that of the homogeneous electron gas at each point. Thus, the exchange-correlation functional can be approximated by

$$E^{LDA}_{XC}[n(\vec{r})] = \int v_{XC}(n(\vec{r})) \cdot n(\vec{r})d\vec{r}, \tag{3.13}$$

where $v_{XC}(n)$ is the exchange-correlation energy density of a homogeneous electron gas.

In this work we will use the Generalized Gradient Approximations (GGA), which is the logical improvement of the standard LDA. It accounts for an inhomogeneous distribution of the electronic density. Within GGA, the exchange-correlation energy accounts for the electronic density gradient on the top of the LDA:

$$E^{GGA}_{XC}[n(\vec{r})] = E^{LDA}_{XC}[n(\vec{r})] + \int f(n(\vec{r}), |\nabla n(\vec{r})|) \cdot n(\vec{r})dr. \tag{3.14}$$

Here, the function $f(n(r), |\nabla n(r)|)$ is an approximate expression to an exact one. Several realizations of the GGA can be found in literature. For this study, we consider

the one described by Perdew, Burke, and Ernzerhof [102].

3.1.4 Pseudopotentials

In most of the cases, only the valence electrons participate in the chemical reaction process and atoms bonding, while the core electrons are tightly bound to their nucleus and are weakly affected by the electronic environment. That is why the exact strong potential near to nucleus can be replaced by an effective potential, or pseudopotential. Using the pseudopotentials considerably reduces the computational cost of DFT calculations.

Pseudopotentials are built to reproduce the true potential of the nucleus outside the sphere of a radius r_c, while inside that sphere, they are artificially smoothed as illustrated in Figure 3.1 As a result, we deal with nicely smoothed wavefunctions.

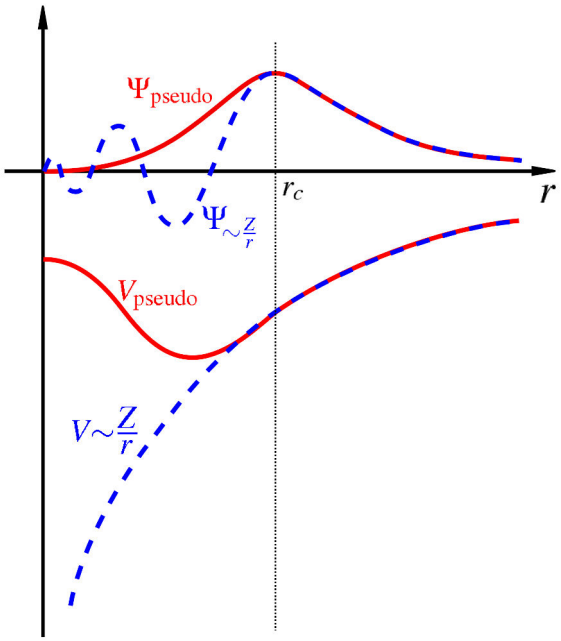

Figure 3.1: Schematic representation of true potential V of nucleus and corresponding fast oscillating wavefunction Ψ (dashed blue line). Pseudopotential V_{pseudo} and corresponding wavefunction Ψ_{pseudo} (plane red line) reproduce true potential outside a sphere of radius r_c.

The many-electrons problem is now reduced to a problem of only valence electrons. The calculations of this work have been done using the norm-conserving Hartwigsen-Goedeker-Hutter pseudopotentials [65].

3.1.5 Choice of a basis set

The choice of a basis set is crucial for the DFT calculations, as it results in accuracy and in reliability of the outputs. The basis set should meet particular

requirements, which generally depend on the system under investigation. All DFT codes can be classified in three categories: the real space localized basis sets with a strong physical meaning; a Fourier space representation (the Plane Waves basis set), and the real space systematic basis sets. The first basis sets are usually formed from Gaussians, which are localized orbital-like functions. They are suitable for non-homogeneous or localized systems, like molecules or nanostructures. However, they form a non-systematic basis set, which means that over-completeness of the basis functions is reached before the convergence. The second basis set is systematic and orthogonal. Periodicity makes this basis set highly suitable for homogeneous and/or periodical systems. For example, such basis sets are widely used in solid state physics. But to calculate inhomogeneous systems with reliable precision, a high energy cut-off is required, which significantly increases the computational cost. Finally, the systematic real space basis sets consist of localized function replicated on uniform grid in real space. The accuracy can be increased by decreasing the grid spacing (called *hgrid* later on). As a "mother" function, sinc or wavelets are of frequent use. Such basis set is suitable for both inhomogeneous and homogeneous systems.

Figure 3.2 compares the plane waves and the real space basis sets. Assuming the same pseudopotentials, the convergence performances for the two basis sets are shown with respect to the degrees of freedom (DOF). It refers to the number of independent coefficients describing the projection of an arbitrary function on the basis set. As representative systems, we consider a pure silicon supercell and a supercell including a carbon interstitial defect. The variation of the core electrons potential is faster for the carbon atom compare to the silicon atom. This is the reason why, to achieve the same energy precision, we need a higher energy cut-off for the Plane Waves basis set. Contrary to the latter case, the wavelet basis set convergence performances are independent on the system homogeneity. That property is attractive to the study of point defects, as we can deal with different point defects keeping the same total energy precision by employing the same calculation parameters.

This work has been done using the BigDFT code, which is based on a Daubechies wavelets basis set. The scaling function ϕ and the wavelet ψ satisfy the following refinement equations:

$$\begin{aligned} \phi(x) &= \sqrt{2} \sum_{j=1-m}^{m} h_j \phi(2x-j) \\ \psi(x) &= \sqrt{2} \sum_{j=1-m}^{m} g_j \phi(2x-j). \end{aligned} \tag{3.15}$$

The refinement equations (3.15) relate two levels of scaling functions with grid spacing h and $h/2$. The elements of a filter h_j and $g_j = (-1)^j h_{-j+1}$ characterize the wavelet family, whereas m is the order of the scaling function-wavelet family. Figure 3.3

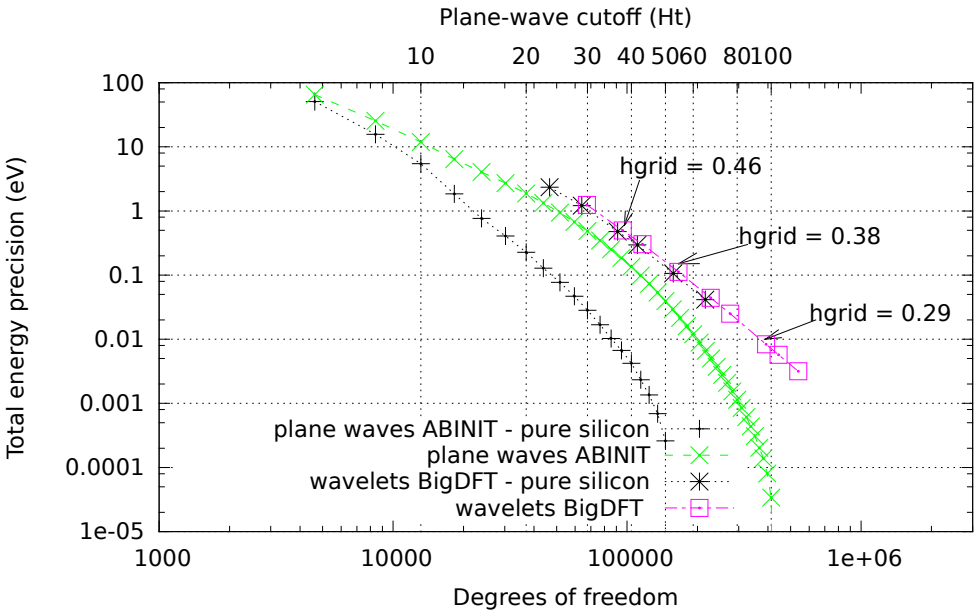

Figure 3.2: The convergence performances of the plane waves and the wavelets basis sets. The dumbbell Si-C [001] defect in silicon (65 atoms) is calculated with Γ-point. The wavelet basis set convergence performances are independent on the system homogeneity, whereas it is not the case for the plane waves basis set.

shows a scaling function and a wavelet of order of 16 of the Daubechies family, which are primarily used in the BigDFT code. Daubechies wavelets are localized in both Fourier and Real space and are orthogonal by definition.

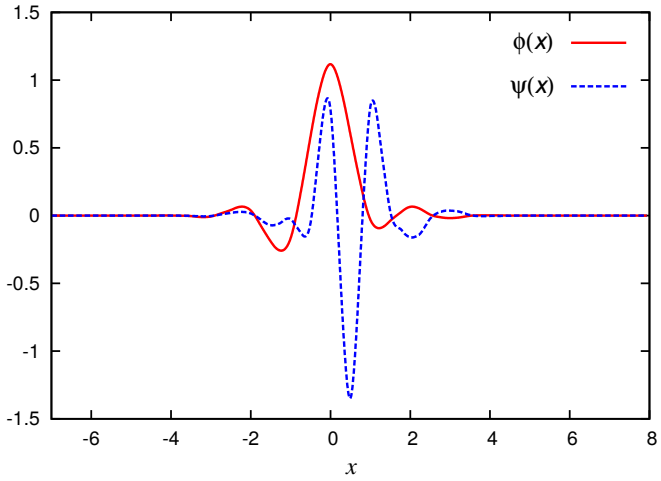

Figure 3.3: ϕ is a Daubechies scaling function and ψ is a Daubechies wavelet of order 16. Such wavelet family is used to construct basis sets in BigDFT code [45].

To choose the appropriate value of the *hgrid* parameter, we consider the energy difference between two model configurations of the interstitial oxygen defect in a 64 Si supercell. We consider this value variation for the total energy precision. As a reference energy, we take the energy, calculated with $hgrid = 0.26$ Bohr. Figure 3.4

shows that for $hgrid < 0.45$ Bohr, basis set provide results with an accuracy of less than 20 meV. This is an appropriate value for the observable energetic characteristics. For the calculations presented in this work, we chose $hgrid = 0.42$ Bohr, as it gives reasonable compromise between the accuracy and the computational cost of single point calculations.

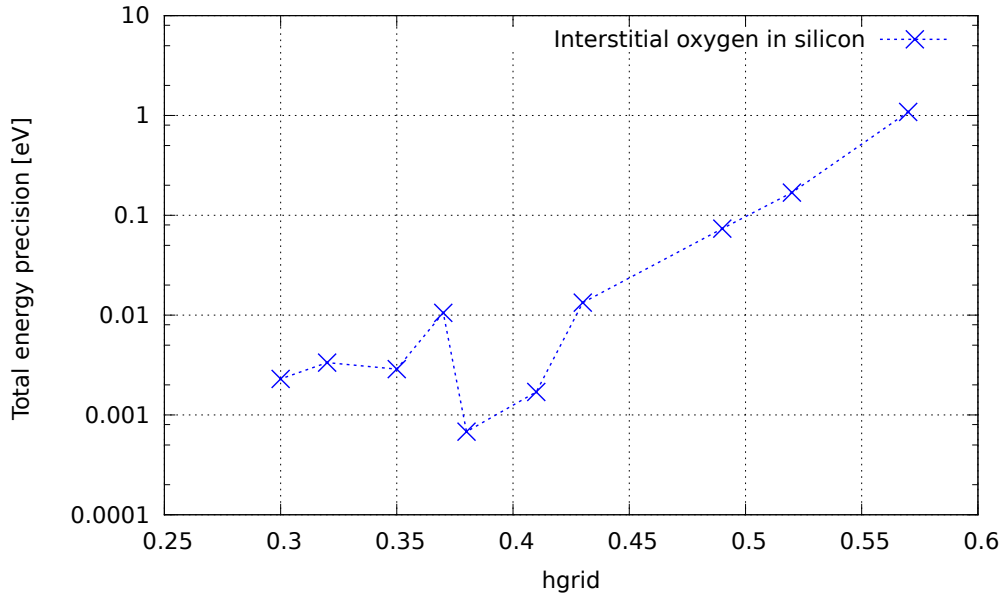

Figure 3.4: The total energy precision convergence test for the wavelet basis set. The representative system is interstitial oxygen atom in 64 Si supercell. k-point sampling include Γ-point only. The $hgrid = 0.42$ gives the reasonable compromise between the accuracy and the computational cose of DFT calculations.

3.1.6 Geometry optimization algorithms

Once we obtained a solution for the system of Kohn-Sham equations, it is possible to investigate the Potential Energy Surface (PES) of the system of interest. While studying point defects, we are particularly interested in Ground State (GS), Transition State (TS) configurations, as well as in minimum energy paths between two neighboring GS. The latter can be found by employing the corresponding optimization methods.

The optimization methods can be classified in two groups: the energy gradient based and the Hessian based algorithms. The first group requires the first energy derivatives with respect to the space coordinates, which, by definition, are the forces, acting on each atom of current atomistic configuration:

$$F_i = -\frac{\delta E(R_1, ..., R_N)}{\delta R_i}. \tag{3.16}$$

The second group of methods requires the matrix of the second energy derivatives,

or the Hessian matrix. The Hessian based methods are much more efficient, as they provide the not only the energy value but also a slope of PES at given point; however, their computation is often too consuming. That is why, for this study we used only the gradient based optimization algorithms, which will be described below in details.

Minimization. Minimization algorithms allows exploring the bottom of the local minimum valley of the PES and provides the GS configurations of the atomistic system.

For this study, we use the fast inertial relaxation engine (FIRE) [11] method, which employs a molecular dynamics scheme. This algorithm accelerates the atom motion in the direction, which is steeper than the current motion direction. If the atom feels an uphill motion, it stops moving in that direction and continues an accelerated movement downhill, until it reaches the minimum. The equation of the motion can be described by the following expression:

$$\dot{\mathbf{v}}(t) = \mathbf{F}(t)/m - \gamma(t)|\mathbf{v}(t)|[\hat{\mathbf{v}}(t) - \hat{\mathbf{F}}(t)], \tag{3.17}$$

where m is the mass, $\mathbf{v} = \dot{\mathbf{x}}$, and $\mathbf{F} = -\nabla E(\mathbf{x})$ is the force, $\hat{\mathbf{v}}$ and $\hat{\mathbf{F}}$ are the unit vectors, indicating the velocity and the force directions. The function $\gamma(t)$ manages the trajectory acceleration and the trajectory direction.

TS optimization. The TS optimization is performed by employing the Direct Inversion in the Iterative Subspace (DIIS) algorithm [109, 110]. Actually, the algorithm minimizes the forces of the atomistic configuration. Hence, it allows reaching both GS and TS configurations, and therefore, may lead to a confusion. To reach a reliable TS configuration, an initial guess should be in a quadratic region of the first-order saddle point. That is why, the method can be applied, only if the saddle point configuration can be deduced from the symmetry with a high precision. As a test, the Hessian matrix calculation of the final structure can be performed. The sufficient criterion is the existence of one and only one negative eigenvalue.

Transition path minimization. Nudged Elastic Band (NEB) algorithm allows finding the minimum energy path between two local minima [39]. The idea of the method is the following. Firstly, a set of images, or replicas, connecting two adjacent minima is created. Replicas are connected with spring forces, which forces to keep images equidistantly indented from each other along the path.

The spring forces of the image i are applied along the tangent of the current

migration trajectory τ_i:

$$\tau_i = \frac{\mathbf{R}_i - \mathbf{R}_{i-1}}{|\mathbf{R}_i - \mathbf{R}_{i-1}|} + \frac{\mathbf{R}_{i+1} - \mathbf{R}_i}{|\mathbf{R}_{i+1} - \mathbf{R}_i|}. \tag{3.18}$$

The true calculated forces of the replica i is expanded on their parallel and perpendicular components:

$$\mathbf{F}_i = \nabla E(R_i) = \nabla E(R_i)|_\perp + \nabla E(R_i)|_\parallel, \tag{3.19}$$

and only the perpendicular component of the true forces is taken into account. The expression for the forces of the image i can be then expressed as

$$\mathbf{F}_i = \mathbf{F}_i^s|_\parallel + \mathbf{F}_i^t|_\perp = k[(\mathbf{R}_{i+1} - \mathbf{R}_i) - (\mathbf{R}_i - \mathbf{R}_{i-1})] \cdot \hat{\boldsymbol{\tau}}_i - \nabla E(\mathbf{R}_i)|_\perp, \tag{3.20}$$

where $\hat{\boldsymbol{\tau}}_i$ is the unit vector of a tangent $\boldsymbol{\tau}_i$.

This method allows obtaining the initial guess for the TS configuration, especially, when the latter is impossible otherwise (for example by using the DIIS scheme).

3.2 DFT for point defects studies

3.2.1 Boundary conditions

A point defect in silicon crystal is a particular system to model, because the periodicity of the bulk crystal is broken by its presence. Such systems can be studied via either finite cluster or supercell approach. Both have advantages and disadvantages and none of them is perfect.

The finite cluster method allows studying an isolated defect surrounded by silicon cluster of size L. Both the limited size and the surface effects are sources of errors in the finite cluster approach. In addition, the edges of the cluster are usually passivated by hydrogen atoms, the surface shape and the passivation are known to affect point-defect properties [34].

The supercell approach eliminates the surface problems, but the supercell size restricts the concentration of point defects. By using of both a supercell and a finite cluster approaches, most of modern simulations of point defects in silicon largely (by several orders of magnitude) overestimates their solubility limits. Despite those difficulties, both approaches provide quantitatively reliable results for the neutral point defects, which are the subjects of the present study. However, to avoid undesired electronic impact from the passivated surface of the cluster, we used the periodic boundary conditions for all calculations.

3.2.2 Chemical potential

The chemical potential of a bulk silicon atom can be obtained through single point energy calculations of the perfect crystal. If we assume that we deal with a supercell of N atoms, the chemical potential can be defined as:

$$\mu(Si) = E^{tot}(NSi)/N \tag{3.21}$$

Then the chemical potential of any substitutional atom A and interstitial B can be obtained via:

$$\begin{aligned} \mu(A) &= E^{tot}((N-1)Si + A) - (N-1)\mu(Si) \\ \mu(B) &= E^{tot}(NSi + B) - N\mu(Si) \end{aligned} \tag{3.22}$$

3.2.3 Binding energy

The binding energy of a complex of two compounds, for example a substitutional A and an interstitial B, can be obtained as:

$$E_b(AB) = -E^{tot}(AB) + (N-1)\mu(Si) + \mu(A) + \mu(B). \tag{3.23}$$

The positive binding energy of a complex AB means that this complex formation is energetically preferable. In this case, the probability of two species A and B to be in a complex is higher than being separated. The negative binding energy means, that the complex simply cannot be formed.

3.3 Frequencies calculations

Another important characteristic of the point defects is their local vibrational modes. Atoms in a perfect crystal collectively oscillate around their equilibrium sites that results in quantized vibrational modes or phonons. Phonons, also considered as excitations of a crystal, are collective vibrations.

The defect or an impurity can introduce one or more additional vibrational modes. If the defect replaces a heavier host atom or occupies an interstitial position, it raises the vibrational modes with elevated frequency modes compare to the crystal phonons. Unlike the phonon, the vibrational mode of defect is localized in space. Therefore, they are called the Localized Vibrational Modes (LVM).

The phonon spectra of a bulk as well as LVM of a defected structure obtained in *ab initio* simulations can be directly compared with experimental data. The phonon frequencies ω versus wavevector dispersion q can be experimentally determined via neutron scattering. The possible techniques to identify LVM of defects include: measuring of IR absorption spectra using Fourier Transform Infrared Spectroscopy

(FTIR), photoluminescence (PL) absorption, and Raman Spectroscopy for the Raman active modes.

3.3.1 The frozen-phonon approximation

The vibrational modes of an atomic structure can be obtained from the second derivative of the energy with respect to a displacement of the atoms. The values, scaled with the relevant roots of the masses, give the dynamical matrix. Its eigenvalues are the square of the frequency modes. Two principle approaches to calculate the second energy derivatives are the linear response of electronic density and frozen phonon approximations. The latter was used in present work.

To calculate the second derivatives in the frozen phonon approximation, we first need the fully relaxed structure. The forces in such structure are by construction equal to zero. Then, a small shift of $\pm h$, chosen to be 0.007 Bohr of one given atom N, is applied along one of the axis $i \in \{x, y, z\}$. Finally, the corresponding electronic density and forces are recalculated. The forces on the atoms are no longer negligible. For example, an atom M feels the force $F^{\pm}_{iN}(jM)$ in a direction $j \in x, y, z$. Finally, the dynamical matrix elements can be calculated as

$$D_{iN,jM} = \frac{1}{\sqrt{m_N m_M}} \frac{F^{+}_{j,M}(i,N) - F^{-}_{j,M}(i,N)}{2h}. \tag{3.24}$$

The calculations of a complete dynamical matrix of a defected structure is a computationally heavy task. For a N-atoms system, such calculation is $6N$ times more expensive than a simple single-point energy calculation. However, the symmetry of the crystal and the locality of the defect allow reducing the computational cost of the vibrational frequencies identification almost without losses in precision. In brief, the defect and its closest surrounding were calculated exactly, while remote atoms were considered as unperturbed bulk atoms. Below, we give the details of the LVM calculations of the point defects in more details.

3.3.2 Frequencies of the bulk silicon

The silicon crystal has the diamond crystallographic structure with two atoms supercell and the face centered cubic symmetry. The atoms are equivalent with respect to the symmetry transformation, for example, inversion or rotation by $\pi/4$ plus the translation by $a(1/4, 1/4, 1/4)$. Thus, it is enough to perturb only one atom from its equilibrium position to restore the whole dynamical matrix of the perfect supercell.

Displacement of a single atom N gives one column (or line) of elements of the

dynamical matrix $D_{iN} = D_{Ni}, i \in 1, ..., N_{max}$, where

$$D_{ij} = \begin{pmatrix} d_{xx}^{ij} & d_{xy}^{ij} & d_{xz}^{ij} \\ d_{yx}^{ij} & d_{yy}^{ij} & d_{yz}^{ij} \\ d_{zx}^{ij} & d_{zy}^{ij} & d_{zz}^{ij} \end{pmatrix} \tag{3.25}$$

Note, that the dynamical matrix is symmetric $D_{ij} = D_{ji}$.

The other elements can be obtained taking into account the relative arrangement of atoms. For example, atom 5 on Figure 3.5 will feel exactly the same impact from displacement of atom 1, as atom 6 will feel from atom 4, and so on. In other words, the pairs of atoms {1, 5}, {4, 6}, {3, 8}, and {2, 7} are equivalent. In the same manner, other equivalent pairs can be identified.

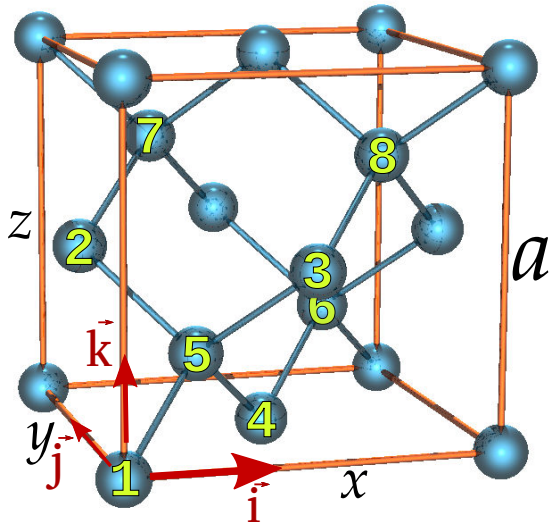

Figure 3.5: 8 numbered atoms compose the silicon unit cell with the cell parameter a.

The relative distance between two atoms N and M can be described by the vector $\vec{V} = \frac{a}{4}(n_x\vec{i} + n_y\vec{j} + n_z\vec{k})$, where a is the size of the unit cell, n_x, n_y, n_z are integers. Each dynamical matrix element D_{NM} corresponds to a particular set of coefficients (n_x, n_y, n_z).

Thus the construction of the dynamical matrix was done in three steps: 1) we calculate the part of the dynamical matrix, which corresponds to a single atom movement, 2) we associate the existing matrix elements with the displacement coefficient, and 3) we determine the displacement coefficient for the remaining part of the dynamical matrix and fill it with corresponding elements.

In this study we deal with two types of supercells, which frame of references are rotated around [001] axis by $\pi/4$ with respect to each other. The first frame of references has its basis vectors $(\vec{a_1}, \vec{a_2}, \vec{a_3})$ collinear with crystallographic directions ([100], [010], [001]), while the second frame of references has its basis vectors $(\vec{b_1}, \vec{b_2}, \vec{b_3})$

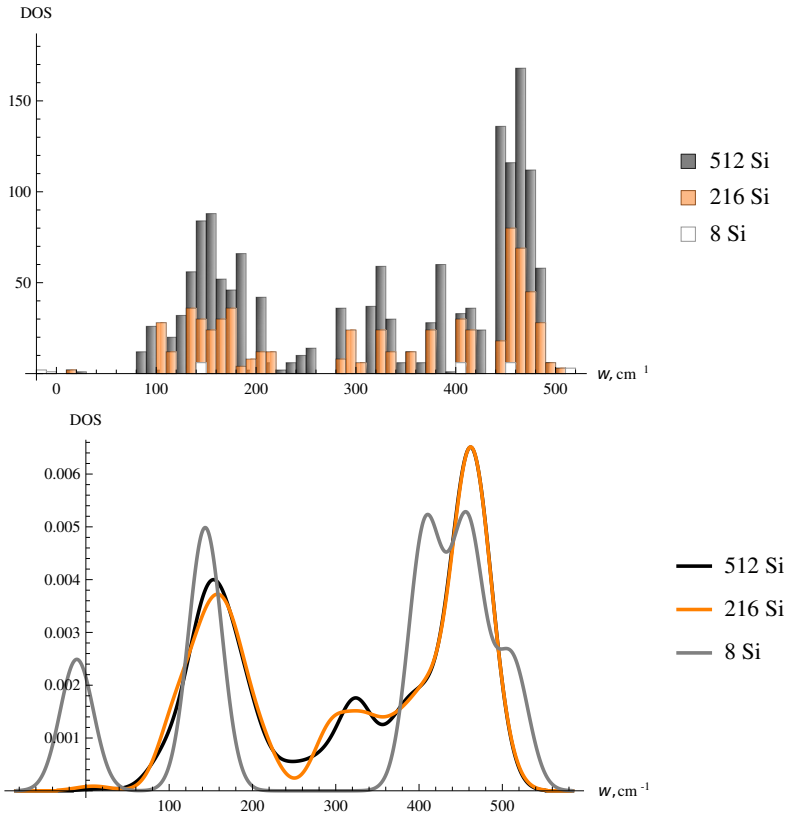

Figure 3.6: The phonon dispersion as a function of the supercell size. 8 Si, 216 Si, and 512 Si supercells are considered. The top graph shows the histogram of the calculated frequencies, while the bottom image shows the smeared phonon dispersion.

collinear with ([110], [$\bar{1}$10], [001]) The symmetry conversions of the bulk silicon consist of the following elements:

- translation $(O, [x, y, z]) \to O', [x, y, z])$
- inversion $[x, y, z] \to [-x, -y, -z]$
- reflection in (100), (010), and (001) crystallographic planes. For the 1st frame of references (8 Si, 64 Si, 216 Si, 512 Si atoms supercells) such reflections correspond to $[x, y, z] \to [-x, y, z]$, $[x, y, z] \to [x, -y, z]$, and $[x, y, z] \to [x, y, -z]$, respectively. For the 2nd frame of references (192 Si atoms supercell) such reflections correspond to $[x, y, z] \to [y, x, z]$, $[x, y, z] \to [-y, -x, z]$, and $[x, y, z] \to [x, y, -z]$, respectively.
- translation together with rotations of $\pm\pi/4$ around one of the [100], [010], and [001] axes. For the 1st frame of references $[x, y, z] \to [y, -x, z]\&[-y, x, z]$, $[x, y, z] \to [x, -z, y]\&[x, z, -y]$, and $[x, y, z] \to [-z, y, x]\&[z, y, -x]$. For the 2nd frame of references conversion around [001] axis will be the same as in the previous case and is sufficient to provide all missing elements.

It is easy to show that the last two elements lead to the same conversions in the 1st frame of references. This manipulations are quite easy in the case of the small supercell, however, in our calculations we need the large supercell to properly account

for the q vectors. Therefore, we should carefully consider all the symmetry properties, to obtain correct results.

The phonon dispersion is restricted with the supercell size, which need to be converged in order to correctly reproduce the density of the states. In order to verify the method, we performed calculation on 8 Si, 216 Si, and 512 Si atoms supercells. The obtained frequencies dispersion are illustrated in Figure 3.6. All three supercells give the similar frequency range: three zero frequencies are obtained that corresponds to the translations in three Cartesian directions, the maximum frequency correspond to $\sim 510\ cm^{-1}$. It can be seen that the phonon DOS are similar in the cases of 216 Si and 512 Si supercells. This observation suggests that 216 Si atoms supercell allows obtaining converged frequency modes for the pristine supercell. In this work, to study the properties of defects and defect interactions, we will assume bigger supercell of 512 Si, being sure, that obtained frequencies are converged.

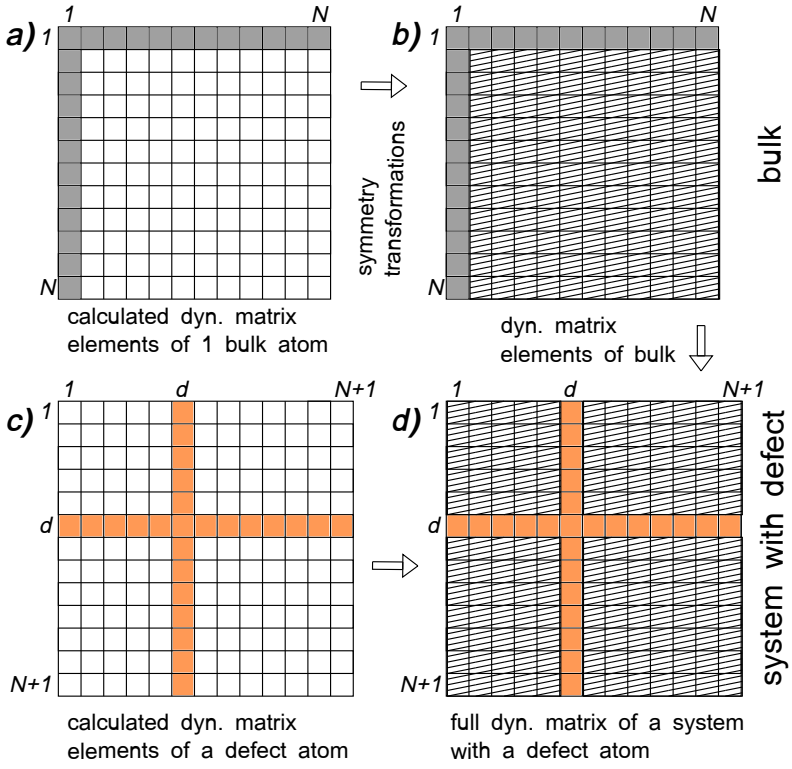

Figure 3.7: The used scheme to calculate the dynamical matrix of a structure with a defect. *a)* Step 1. We calculate one column (or one line) of a dynamical matrix for the perfect supercell. *b)* Step 2. We apply the symmetry rules and fill the whole dynamical matrix of the perfect supercell without performing any additional simulations. *c)* Step 3. We consider the system containing defect(s) d and calculate the matrix elements related with the defect atoms. *d)* Step 4. We fill the dynamical matrix of the system with the defect by the dynamical matrix elements of the perfect supercell.

3.3.3 Frequencies spectra for the defected structure

If the defect is added to a supercell, the symmetry of the bulk is perturbed. Moreover, there is an additional atom that interacts with all the atoms in the supercell through the long-range elastic interactions. However, the frequency modes from the light defects have a local nature. Thus, a sufficiently big shell of atoms should be calculated exactly, while the rest of the atoms can be considered as an unperturbed bulk atoms.

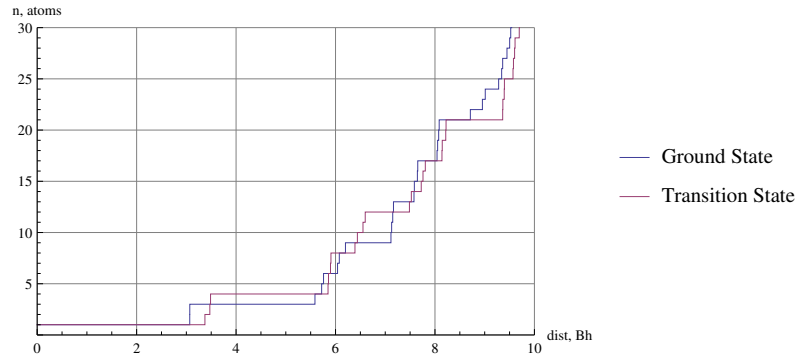

Figure 3.8: The number of atoms included in the spheres of radius *dist* around the interstitial oxygen, occupying GS and TS configurations.

In order to reduce the calculation time, we performed the calculations of the defected system according to the algorithm illustrated in Figure 3.7. We prepared the database for a bulk supercell as it was described above (see Figure 3.7 *a*-*b*). Then, we performed the calculation of the dynamical matrix elements of the defect atom(s) and a shell of neighbors around the defect(s) Figure 3.7 *c*. Finally, the residual parts of the dynamical matrix that corresponds to the bulk atoms and their interactions with each other are filled from the previously calculated database for the nondefected bulk supercell.

The number of the obtained frequencies is equal to the number of eigenvalues of the dynamical matrix. Thus it depends on the number of atoms in the system. Besides three zero modes and the spectrum of the bulk silicon, high frequency modes of the defect are represented in the frequency range.

We performed a test to check the convergence of the shell size around the defect atom. As an indicator of the convergence, we took the evolution of each individual frequency mode. We separately studied GS and TS configurations of interstitial oxygen. We introduced an interstitial oxygen and performed calculations by precisely taking into account the nearest neighbors of the oxygen atom. Then, we progressively added atoms, lying further inside the sphere of radius $r = 5.5, 6.0, 6.5, 7.0, 7.5, 8.0, 8.5$ Bohr. The number of atoms included in the calculations can be derived from Figure 3.8. We have calculated precisely all atoms, inside the sphere, while all other atoms

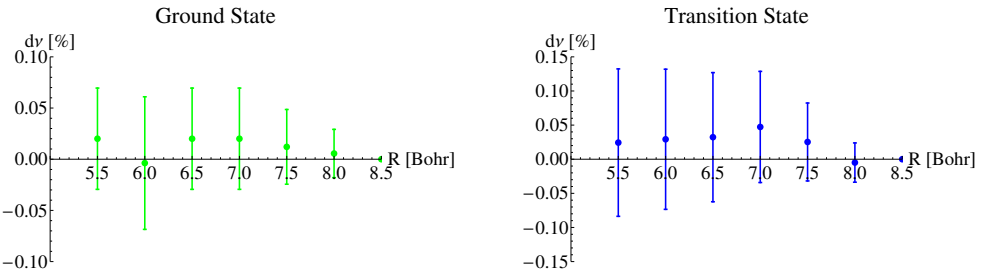

Figure 3.9: The average error $d\nu$ for the calculated vibrational frequency modes of both ground state (left image) and transition state (right image) configurations. The errors are represented as a function of radius R of the sphere around the oxygen atom. A region inside the sphere was precisely calculated. Frequencies, calculated with $R = 8.5$ Bohr, are considered as reference.

were considered as unperturbed bulk. As GS and TS configurations have different geometries, the numbers of atoms and their precise surroundings are different.

Figure 3.9 shows the deviation of every frequency from the most precise of them, which corresponds to the shell of radius 8.5 Bohr. The maximum deviation for the GS and TS configuration modes is less than 0.07 % and 0.14 %, respectively, for all spheres. We infer that the smallest sphere of 5.5 Bohr, corresponding to the first shell of neighbors, can be considered for the future calculations, as it provides the accurate modes for the whole spectrum of frequencies.

Chapter 4

Impact of heavy doping on structural and diffusion properties of oxygen impurity

Oxygen impurity in crystalline silicon has been widely studied using both experimental and theoretical techniques. Structure, vibrational characteristics, and diffusion mechanisms of oxygen species in low-doped material are well understood. Nevertheless, new questions keep raising. Several detrimental complexes contain oxygen species, among them are Thermal Donors and Boron-Oxygen complexes. The former affect electrical properties of silicon based electronic devices at 450-500 ℃ temperature range. While the latter degrade the efficiency of silicon based solar panels. The structure and the formation mechanisms of both kind of complexes are still debated. The formation of these complexes depend on the kinetic properties of oxygen species, particularly on oxygen diffusivity in crystalline silicon. The latter was found to be stronly affected by heavy doping at 300-700 ℃ temperature, as summarized in Chapter 2. Unfortunately, these experimental observations can not provide the underlying mechanisms, responsible for the changes in oxygen diffusivity.

In this chapter, we address the properties of oxygen impurity in bulk silicon at the atomistic level. Using the DFT supercell approach, we aim to study the microscopic mechanisms induced by heavy doping on the oxygen kinetic properties [1]. We start by describing some methodological details. Then we present the results of our investigations of structural and diffusion properties of interstitial oxygen in its neutral state. Next, we switch to the investigation of the impact of heavy doping on the diffusing properties of oxygen species, namely monomer and dimer.

It has been suggested [139], that heavy doping affects the transport properties of oxygen either by introduction of the internal strain or by changing of the Fermi

1. Results presented in in this Chapter have been partially published in Reference [129].

energy level. Here, we aimed to consider both effects. Particularly, to test the former hypothesis we will consider the effect of external strain applied to the supercell. While to test the latter hypothesis we will place the dopant atoms nearby diffusing oxygen species. In both cases the diffusion coefficient will be calculated and the results will be compared with experiments. Based on the obtained results, we will discuss the possible acceleration and retardation mechanisms of oxygen diffusion in heavily doped silicon.

4.1 Method

The computational tools, used to simulate the structural and vibrational characteristics of point defects in crystalline silicon, have been described in detail in Chapter 3. In this section, we will introduce some additional theoretical background for the diffusion coefficient calculations; we will also specify the techniques, which we employed for each particular study.

Diffusion coefficient The diffusion coefficient of the migrating species can be expressed in the most general form as

$$D = D_0 \times exp(-\frac{E_a}{kT}). \tag{4.1}$$

where E_a is the activation energy and D_0 is the pre-exponential factor. Both parameters can be calculated using first principles methods.

In the case of a simple defect diffusion, the activation energy is equal to the migration energy. The migration energy is the minimal energy needed to jump to a closest neighboring ground state (GS) through a transition state (TS): $E_a(A) \equiv E_m(A) = E^{TS} - E^{GS}$. An interstitial oxygen monomer is a classical example of such species. In the case of a diffusing defect complex, such as an oxygen dimer, the activation energy also depends on the binding energy E_b (see Equation 3.23 for definition of E_b) of the complex and can be expressed as:

$$E_a(AB) = E_m(AB) - E_b(AB). \tag{4.2}$$

The second parameter in Equation (4.1), the pre-exponential factor D_0, depends on the single jump length d, the number of equivalent paths p and the dimensionality of the space n. Taking into account the random walk theory and the vibrational entropy of the diffusion path as proposed by Vineyard *et al* [133] one gets the

expression for the pre-exponential factor value:

$$D_0 = \frac{d^2 p}{2n} \frac{\prod_i^N \nu_i^{GS}}{\prod_i^{N-1} \nu_i^{TS}}. \tag{4.3}$$

Here ν_i^{GS} and ν_i^{TS} are the frequencies of the vibrational modes of the ground state and transition state configurations, respectively. N is the number of the frequency modes, which is equal to the number of the atoms in the system multiplied to the dimensionality n minus n zero frequency modes related to the translations.

Calculation of diffusion coefficient with an external strain applied to a supercell A 192 Si atoms supercell was employed for the investigation of the impact of strain on the diffusing properties. A Monkhorst-Pack grid of 1x1x3 was employed for the k-point sampling. The X and Y axes of the supercell are collinear with $\langle 110 \rangle$ and $\langle 1\bar{1}0 \rangle$ crystallographic directions, while the Z axis is collinear with $\langle 001 \rangle$ direction. This orientation allows applying uniaxial and biaxial strain along the migration path of the interstitial oxygen monomer and dimer. The supercell was allowed relaxing in residual unconstrained axes. Then the diffusing species were introduced into the supercell and the calculations of migration energy as well as the pre-exponential factor value were performed. At this stage we do not introduce any dopant atoms into the supercell and we study the pure effect of uniaxial and biaxial strains. The applied strains, ranging from -1.0% to $+1.0\%$, largely cover the experimentally reachable values.

Calculation of diffusion coefficient with a dopant in a supercell To study the impact of doping on oxygen migrating properties, we used a 512 Si atoms supercell. First, we incorporated a substitutional dopant in the supercell and performed a full relaxation within the supercell. Then, an oxygen atom was introduced in the middle of the area, elastically unperturbed by the dopant presence. That procedure allowed us to avoid the elastic interaction between dopant and oxygen atoms.

Analysis of the charge transfer mechanism In Subsection 4.4.1, we employed the Nudged Elastic Band (NEB) calculations for a few representative cases to investigate the charge assisted diffusion. NEB paths of 41 images were converged with a convergence criteria of 0.005 Ha/Bohr on forces, which are perpendicular to the path direction.

Introduction of a p- or n-type dopant (atoms of both types have an odd number of electrons) into the supercell (atoms of silicon and oxygen have an even number of electrons) results in an odd number of electrons in the system. The electronic distribution of the unpaired electron can be derived as following $\rho^{unpaired}(\vec{r}) =$

$\rho_{\uparrow}(\vec{r}) - \rho_{\downarrow}(\vec{r})$.

Finally, the electronic structure of diffusion process was further investigated using The Maximally Localized Generalized Wannier Functions code [89], interfaced with BigDFT. The calculations were performed for the ground state and transition state configurations in the 512 Si supercell using the Perdew-Burke-Ernzernhof exchange-correlation energy functional [102].

4.2 Oxygen diffusion in low-doped material

The major part of oxygen impurities in silicon occupy interstitial sites between two neighboring Si atoms (sometimes called as bond-centered interstitial). The oxygen atom O_i is covalently bonded to them as shown in Figure 4.1(a). This defect will be referred to as *oxygen monomer* later on. The calculated Si-O bond lengths of 1.62 Å and Si-O-Si angle of 162° are in good agreement with previous calculations [49, 27, 105] , as summarized in Table 4.1. At low temperatures T<700 ℃, the interstitial oxygen atoms form dimers, which consist of two oxygen atoms occupying neighboring puckered bond-centered sites. As shown in Figure 4.1(c), oxygen atoms lie in one of the ⟨110⟩ crystallographic planes. The obtained Si-O bondlengths and Si-O-Si angles are listed in Table 4.1 and show a good agreement with recent reported *ab initio* investigations [27, 105, 97, 41, 113].

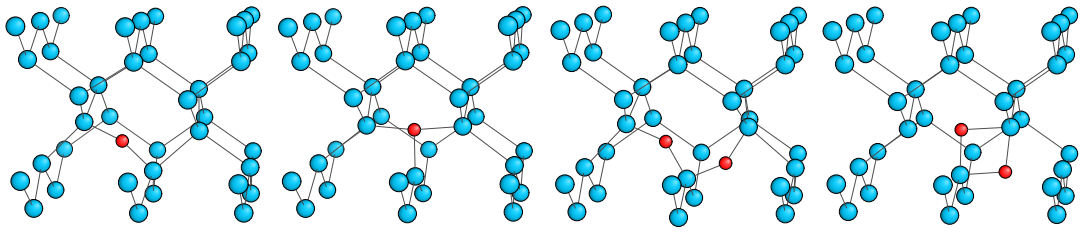

(a) O_i GS (b) O_i TS (c) O_{2i} GS (d) O_{2i} TS

Figure 4.1: The ground state (GS) and transition state (TS) configurations for oxygen monomer (O_i) and dimer (O_{2i}).

As it was reported above, the diffusion coefficient can be fully described by the two parameters, namely the activation energy and the pre-exponential factor. The activation energy has been theoretically considered in many *ab initio* studies (see Table 4.2), while the pre-exponential factor calculations have been performed only by Gusakov [50] and by Jiang *et al* [59]. While the latter have calculated diffusion coefficient using empirical potentials, Gusakov obtained pre-exponential factors for both monomer and dimer using *ab initio* approach. His D_0 of monomer are very close to the experimental values, while that of dimer deviates more significantly.

Monomer	Ex-C	$Si_{1,2}$-O [Å]		$\hat{a}$ [°]	
ab initio					
This work	PBE	1.62		162	
Coutinho [27]	PW	1.62-1.65		158	
Pesola [105]	PZ	1.63		127-154	
Ewels [41]	PZ	1.63			
Gusakov [49]	RHF	1.63		162	
Gusakov [50]	B3LYP	1.67		172	
Dimer	Ex-C	$Si_{1,2}$-O_I [Å]	$Si_{2,3}$-O_{II} [Å]	$\hat{a}$ [°]	$\hat{c}$ [°]
ab initio					
This work	PBE	1.63, 1.61	1.61, 1.63	143	145
Coutinho [27]	PW	1.66, 1.64	1.63, 1.67	130	127
Pesola [105]	PZ	1.62, 1.62	1.63, 1.67	157	154
Oberg [97]	PZ	1.62, 1.64	1.62, 1.65	144	144
Ewels [41]	PZ	1.52, 1.67	1.52, 1.67	166	166
Ramamoorthy [113]	LDA	1.65, 1.65	1.65, 1.65		

Table 4.1: Structural parameters of the oxygen monomer and dimer depicted from some recent *ab initio* investigations. See Figures 4.7 and 4.8 for notations. Here, Ex-C is a shortcut for the exchange-correlation functional. PBE (Perdew-Burke-Ernzernhof) Generalized Gradient Approximation [102]; PZ (Perdew-Zunger) Local Density Approximation [104]; PW (Perdew-Wang) Local Density Approximation [103]; revPBE (Revisited Perdew-Burke-Ernzernhof) Generalized Gradient Approximation [140]; RPBE (Revisited Perdew-Burke-Ernzernhof) Generalized Gradient Approximation [52]; B3LYP (Becke(3 parameter)-Lee-Yang-Parr) Hybrid functional [122].

In present study, we calculated both parameters, activation energy and pre-exponential factor, at absolute zero temperature. That allows obtaining the temperature dependence of the diffusion coefficient for the oxygen monomer and the dimer diffusion in pristine silicon. In the following sections, we consider the impact of external strain and heavy doping on these diffusion coefficients.

Monomer The diffusion of O_i proceeds in one of six equivalent $\langle 110 \rangle$ directions. The oxygen atom jumps to the neighboring bond-centered site by passing through the transition state, the so-called "y-lid" configuration. The latter is a highly symmetric threefold coordinated configuration as illustrated in Figure 4.1 (b). Thus, in Equation (4.1) we consider the number of equivalent paths equal to six $p = 6$. The corresponding jump length was measured as a distance between two neighboring GS configurations and is equal to $d = 2.83$ Bohr.

We analyzed the monomer's ground state and transition state configurations in terms of the valence electronic configuration around the oxygen atom. The centers of the Wannier functions are depicted in Fig. 4.2 *a-b*. In the ground state

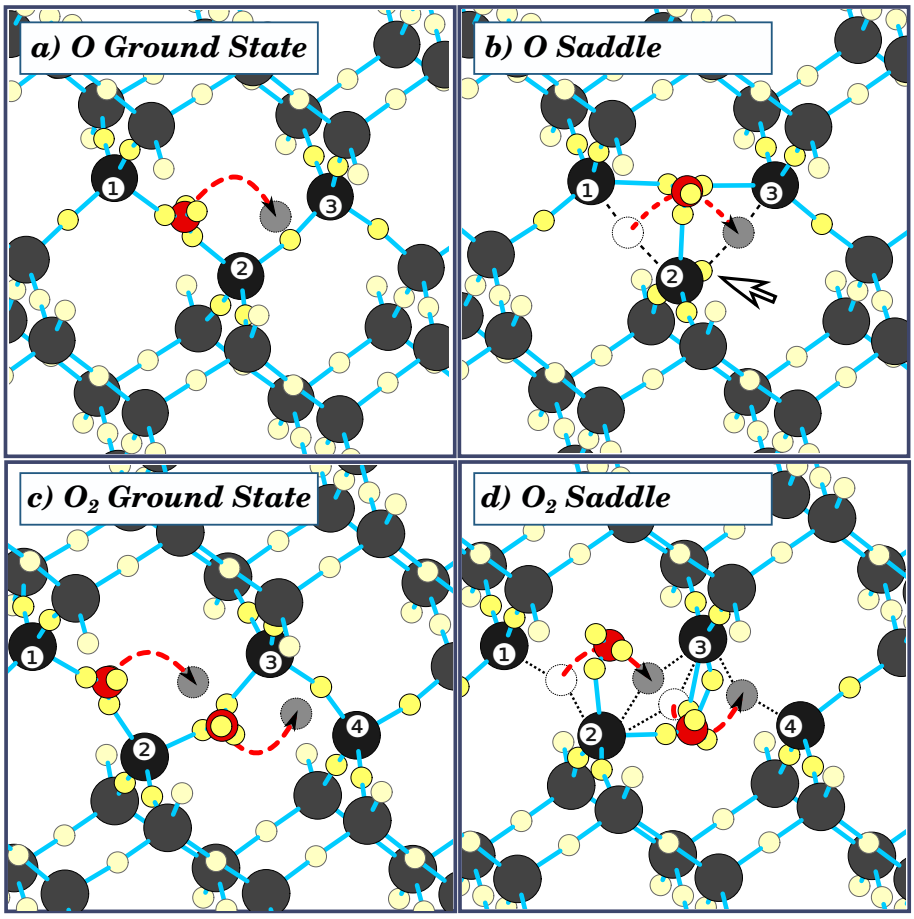

Figure 4.2: O_i and O_{2i} diffusion schemes. Big black and small red filled balls represent Si and O atoms, respectively. Yellow balls represent the positions of the Wannier Centers. The diffusion path(s) of O atom(s) is(are) schematically represented by a dashed arrow pointing to the final position(s) (gray shadows).

configuration, the oxygen atom is bonded to two neighboring Si atoms (Si^1 and Si^2). The remaining valence electrons form two lone pairs on the oxygen. In the transition state configuration, the oxygen is bonded to three Si atoms (Si^1, Si^2, and Si^3). Two of the remaining valence electrons form a lone pair on the oxygen while the last electron is localized in a lone pair near the Si^2 atom (arrow in Fig. 4.2 *b*).

The calculated migration energy and pre-exponential factor are listed in Table 4.2. A migration energy of 2.40 eV is in a good agreement with the value of 2.53 eV depicted from the fit of experimental data [60] (see Eq. (2.1)), whereas the calculated pre-exponential factor of 0.029 cm^2s^{-1} is underestimated compare to that of experiment (0.13 cm^2s^{-1}, see Eq. (2.1)). The calculated diffusion coefficient can be then expressed as

$$D_O^{calc.} = 0.029 \times \exp -\frac{2.40}{kT}\ \mathrm{cm^2 s^{-1}}. \tag{4.4}$$

Figure 4.3 reports the Arrhenius plot of calculated diffusion coefficient together with the experimental data from Reference [60]. Described by Eq. (2.1), the fit of experimental points is plotted with the dashed black line, whereas plain red line reproduces the results of the present calculations (Eq. (4.4)). The calculated diffusion coefficient lies excellently on the measured experimental points. The obtained results will be further discussed later in Section 4.4.2 together with obtained results on dimer diffusion, and with the effect of doping on these values.

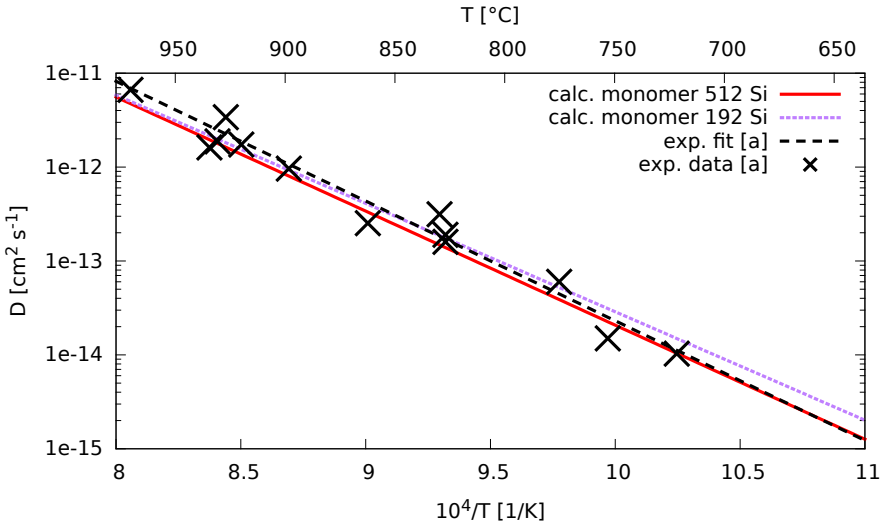

Figure 4.3: Arrhenius plot of the oxygen monomer's diffusion coefficient. Calculated parameters of pre-exponential factor and migration energy lead to an excellent accordance of diffusion coefficient with experimental data. [a] Reference [60].

Dimer In the literature, dimers are suggested to be the primary migrating species at temperatures below 700 ℃ [1, 125, 88, 117]. Murin *et al* [91] have provided

Monomer	Ex-C	$E_a = E_m$	D_0
ab initio			
This work	PBE	2.41	$2.9 \cdot 10^{-2}$
Ramamoorthy [112]	PZ	2.5	
Coutinho [27]	PW	2.2	
Lee [71]	PZ	2.3	
Gusakov [50]	LDA	2.59	0.28
Dzelme [38]	—	2.73	
Estreicher [40]	LDA	1.79	
	PBE	2.01	
	revPBE	2.12	
	RPBE	2.18	
Snyder [120]		2.49	
Ewels [41]	PZ	2.5	
Hoshino [56]	B3LYP	2.7	
Binder [10]	GGA	2.3	
Jiang [59]	emp. pot.	2.43	0.025
Experiment			
Mikkelsen *et al* [60]		2.53	0.13

Dimer	Ex-C	E_a	E_m	E_b	D_0	D^{lt}_{0eff}
ab initio						
This work	PBE	1.48	1.62	0.14	$1.27 \cdot 10^{-25}$	$2.54 \cdot 10^{-7}$
Coutinho [27]	PW		1.4	0.44-0.58		
Pesola [105]	PZ		0.2			
Ewels [41]	PZ		2.4			
Ramamoorthy [113]	PZ		1.5	0.3		
Gusakov [50]	LDA	2.05			0.023	
Snyder [120]			1.36	0.1		
Lee [71]	PZ		0.95, 1.8			
Experiment						
Giannattasio [46]		1.55				$2.16 \cdot 10^{-6}$
Murin et al [91]				0.2, 0.3		

Table 4.2: The calculated migration energies (E_m), binding energies (E_b), activation energies ($E_a = E_m - E_b$) in eV, and pre-exponential factors (D_0) in cm^2s^{-1} for oxygen monomer's and dimer's diffusion. The low temperature pre-exponential factor D^{lt}_{0eff} is described by Eq. 4.6 and depends on the oxygen monomers concentration. Notations for the exchange-correlation functional (Ex-C) are the same as in Table 4.1.

the experimental evidence for fast diffusing dimer via IR absorption experiment. According to numerous first principles calculations [27, 71], the dimers are two oxygen monomers placed on neighboring Si-Si bonds as illustrated in Figure 4.1 (*c*). In the present study, such configuration of the dimer was also the most preferable among others. The list of considered configurations is represented in Table 4.3. The binding energy of a dimer is obtained as follows

$$E_b(O_{2i}) = -E(512Si + O_{2i}) - \\ -E(512Si) + 2E(512Si + O_i). \tag{4.5}$$

The expression above gives a value of 0.14 eV, while an experimental binding is equal to 0.3 eV [91]. We attribute a discrepancy of about 0.16 eV between calculations and experiment with the minor inaccuracies, which are coming from both pseudopotential approximation of our calculations and experimental set up abilities and error bars.

	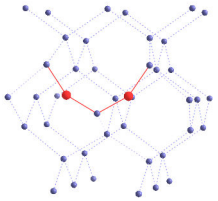	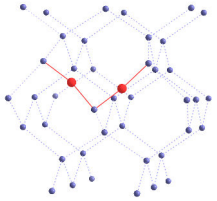	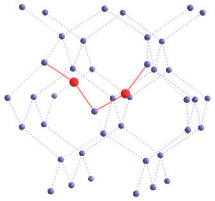	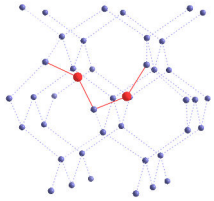
$\hat{a}$	206.3°	167.0°	158.7°	141.9°
$\hat{b}$	152.8°	168.3°	156.5°	143.3°
Si_1-O_I	3.101	3.035	3.061	3.086
Si_2-O_I	3.088	3.016	3.022	3.055
Si_2-O_{II}	3.081	3.016	3.022	3.039
Si_3-O_{II}	3.106	3.032	3.070	3.102
E_b [eV]	-0.08	-0.16	0.08	0.14

Table 4.3: The schemes and geometry parameters of four considered configurations of interstitional dimer. The notations of bond lengths and angles are represented on Figure 4.8. The last geometry, so-called staggered configuration, is the most stable. It gives the binding energy of 0.14 eV and will be considered in all future calculations. These four configurations are close in energy that reveals the flat shape of the potential energy surface close to the minimum.

The dimer diffuses in two steps: first, it jumps through the square form (See Figure 4.1 (*d*) to the neighboring staggered configuration (Figures 4.2 *c*&*d*). Then, a nearly barrierless rotation around Si-Si bonds is required to continue the diffusion in the same direction. The activation energy, obtained using Equation (4.2), is equal to 1.48 eV, which is in an excellent agreement with the experimental data listed in Table 4.2.

The Wannier centers for the dimer's ground state and transition state configurations are depicted in Figure 4.2 *c*-*d*. In the ground state configuration, both

oxygen atoms are bonded to their two neighboring Si atoms similar to the monomer case. Each oxygen atom has a couple of lone pairs. The electronic distribution of the transition state configuration differs from the O_i case. It is more complex with three lone pairs on the first oxygen and two lone pairs on the second oxygen. The electronic configurations represented in Figure 4.2 will serve as references for the following analysis in doped Si.

Once the dimer is formed, it preferably diffuses forward and backward along the particular $\langle 110 \rangle$ direction because its reorientation to another (110) plane is an energetically unfavorable procedure. According to an *ab initio* study of Lee *et al* [71], it is as costly as an interstitial monomer migration ~ 2.5 eV. So we considered this process as rarely occurring and thus negligible in the low temperature regime. This is why, to calculate the pre-exponential factor value $D_0(O_2)$ using Equation (4.1), we considered a number of possible equivalent directions being equal to two $p = 2$. The single jump length was calculated to be $d = 2.46$ Bohr.

The effective diffusion coefficient at low temperatures depends not only on oxygen dimer diffusion coefficient, but also on the overall oxygen concentration and binding energy of a dimer. As it was shown by Murphy *et al* [93], it can be expressed as:

$$\begin{aligned} D^{lt}_{eff} \approx D(O) + 2C(O)D_0(O_2)exp(-\tfrac{E_m - E_b}{kT}) \approx \\ \approx D^{lt}_{0eff}exp(-\tfrac{E^{lt}_a}{kT}). \end{aligned} \tag{4.6}$$

At the low temperature regime ("lt"), the impact of monomers diffusion to the oxygen transport can be neglected, and the low temperature effective pre-exponential factor can be expressed as $D^{lt}_{0eff} = 2C(O)D_0(O_2)$.

Assuming the initial oxygen concentration being 10^{18} cm^{-3}, the obtained value of D^{lt}_{0eff} is 2.54×10^{-7} cm^{2}s^{-1}. Figure 4.4 shows the Arrhenius plot of calculated diffusion coefficient for the oxygen dimer at low temperature range, which is compared with DLTS experimental data fit from References [117, 46, 93]. Our results are in a fair agreement with the experimental fit.

Up to now, we have reproduced the diffusing properties of oxygen in the unperturbed pristine Si, we can consider how heavy doping can affect oxygen diffusing properties. We will test the two hypothesis proposed in literature for the enhanced and retarded oxygen diffusion: the effect of strain (Sec. 4.3) and the effect of the Fermi energy change due to the high doping concentration (Sec. 4.4) on the oxygen diffusion features.

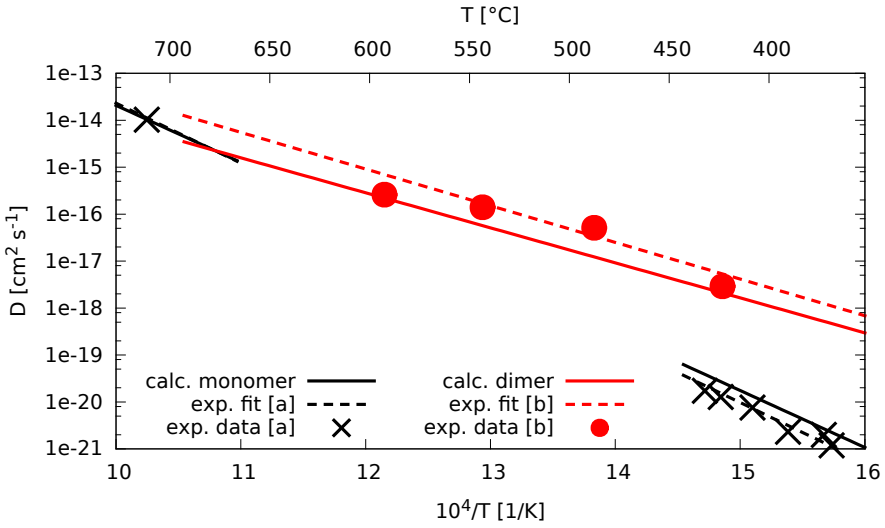

Figure 4.4: Oxygen dimer diffusion coefficient. [a] Reference [60] Below 450 °C, the stress-induced dichroism experiments, which are sensitive only to monomers diffusion, are well described by the extrapolation of the high temperature diffusion coefficient. These data also agrees with calculated diffusion coefficient for monomers. [b] Reference [117] The experimental data (red circles) is an effective oxygen diffusivity. This data agrees with the calculated diffusion coefficient for dimers.

4.3 Effect of strain on oxygen impurity

The first hypothesis of enhanced/retarded diffusion of oxygen in heavily doped silicon to check theoretically is the effect of strain on the oxygen diffusion coefficient.

These calculations were performed in a 192 Si atoms supercell, which frame of references can be obtained through rotation by 45° around Z axis of that of 216 Si atoms supercell. In this new frame of references, we let the monomer locate and diffuse in $\langle 110 \rangle$ crystallographic plane along the $(1\bar{1}0)$ direction.

First of all, we comment on the migration energy and pre-exponential factor values obtained in the 192 Si supercell. The migration energy and the pre-exponential factor were calculated to be 2.29 eV and 0.010 cm^2s^{-1}, respectively, compare with 2.40 and 0.029 obtained using the 512 Si supercell. As follows from Figure 4.3, calculations in 192 Si supercell is sufficiently large to accurately reproduce oxygen's diffusion properties. The effect of applied strain on the monomer's migration energy is illustrated in Figure 4.5.

External compressive strain tends to reduce the migration energy, while the external tensile strain tends to increase it almost in all cases except when it is uniaxially applied in (110) direction, i.e. perpendicular to the diffusion direction. The effect of uniaxial strain is maximum when it is applied along the migration direction. A variation of less than 0.1 eV is obtained for 1% of deformation. The biaxial strain applied in the diffusion plane gives a variation of 0.15 eV for the

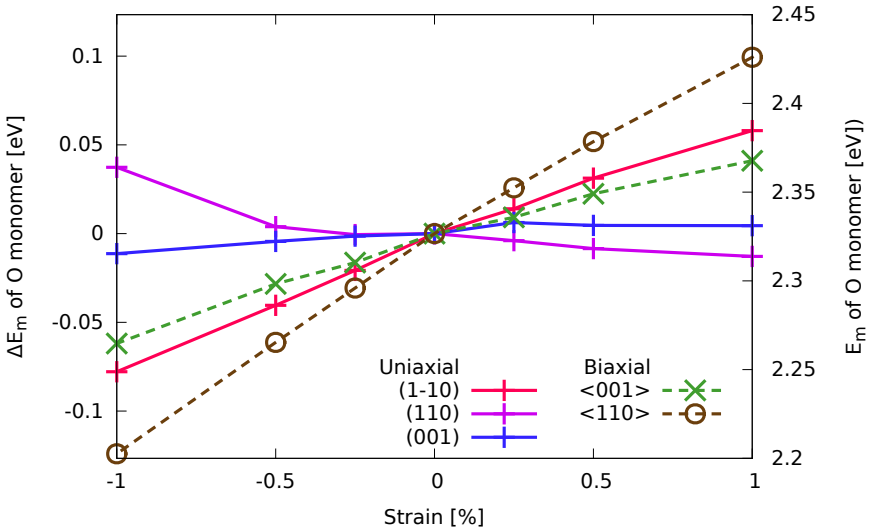

Figure 4.5: The effect of the unaixial and biaxial strains. Oxygen monomer migrates along X direction and staying in XZ plane. The variation in energy is less than 0.1 eV for all tested strains.

monomer migration energy at 1%.

However, a strain of ±1.0 % can barely be realized due to the dopant's presence. A change of -7×10^{-3} % was reported in Reference [139] in a heavily Ge doped sample, while for heavy doping with other elements the average absolute strain is below 8×10^{-4}%. Thus, we conclude that neither uniaxial nor biaxial strain will cause noticeable changes in migration energy value.

Strain	E_m [eV]	$D_0(O_i)$ [cm^{2}s^{-1}]
$-$**0.5** %	2.22	0.002
0.0 %	2.29	0.010
$+$**0.5** %	2.37	0.009

Table 4.4: The effect of biaxial strain, applied in ⟨110⟩ plane, on E_m and D_0 of oxygen monomer diffusion. Strains of ±0.5% applied in ⟨110⟩ plane are chosen as an example, as it gives the maximal effect on migration energy. Results suggest a negligible effect on both parameters.

Regarding the impact of strain on a pre-exponential factor value, we performed calculations of the diffusion coefficient for ±0.5% biaxial ⟨110⟩ strains. We chose this plane as it causes the maximal effect on migration energy value, while ±0.5% strain values should give an idea of the deviation range. Table 4.4 lists the corresponding pre-exponential factor and migration energy parameters. Figure 4.6 represents the diffusion coefficients for these cases. It shows the negligible effect of external strain on the diffusivity properties of interstitial oxygen. Especially, if we take into consideration that the studied strains are far beyond the experimentally reachable values with doping. The effect of strain on dimer's migration energy and on binding

energy was found to be smaller than 0.1 eV for all cases. Assuming that the same responses to the external strain take place in the case of dimers, we have not computed of the pre-exponential factors for those. However, we conclude that neither monomer's nor dimer's migration energies can be affected by neither uniaxial nor biaxial external strain.

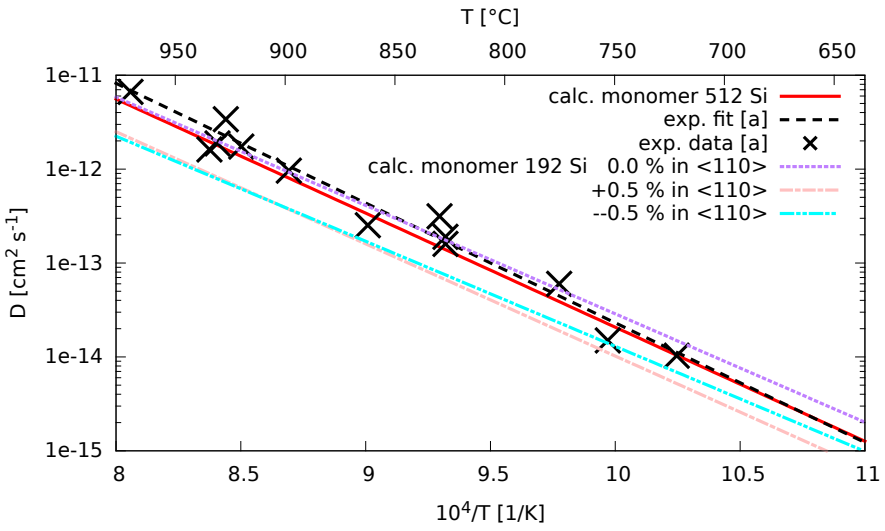

Figure 4.6: Arrhenius plot of the oxygen monomer's diffusion coefficient calculated for the fully relaxed and strained supercells. [a] Reference [60].

4.4 Doped silicon

We have ruled out the effect of external strain to explain the reported enhancement or retardation of oxygen diffusion. The second hypothesis is that oxygen diffusion is sensitive to the Fermi energy level. The latter can be considerable affected by the heavy doping with p- or n-type elements.

To investigate the impact of doping, we performed calculations of the diffusion coefficient of both monomer and dimer in proximity of a dopant atom. In other words, we introduce both the dopant and oxygen in supercell at the same time. The two defects were distanced by 15 Å in a 512 Si atoms supercell to minimize their elastic interaction.

Geometries. The effect of dopants on the geometries of the ground state and transition state configurations are listed in Tables 4.5 and 4.6 for monomer and dimer, respectively. Figures 4.7 and 4.8 reproduce the corresponding geometry schemes of their ground state and transition state configurations. The ground state geometries of both oxygen species are not affected by any of three tested dopants.

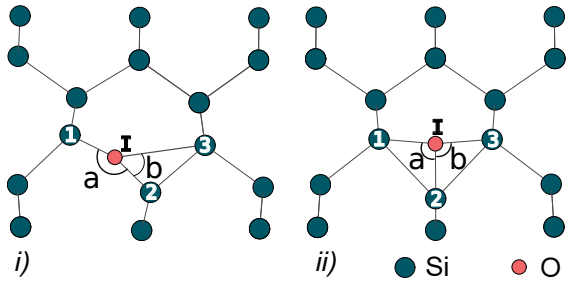

Figure 4.7: Oxygen monomer's *i)* ground state and *ii)* transition state schematic configurations. In Table 4.5, $\hat{\text{Si}}_{123}$ stands for an angle between Si_1-Si_2 and Si_2-Si_3 bonds.

pristine	conf.	$\hat{a}$	$\hat{b}$	$\hat{\text{Si}}_{123}$	Si_1-O	Si_2-O	Si_3-O	Si_1-Si_2	Si_2-Si_3
intrinsic	GS	161.9	52.0	103.9	3.069	3.068	5.586	6.061	4.415
B	GS	162.0	51.9	103.9	3.068	3.068	5.589	6.060	4.416
Ge	GS	162.1	51.9	103.9	3.068	3.068	5.590	6.061	4.414
As	GS	162.1	51.9	103.9	3.068	3.068	5.590	6.061	4.415
pristine	TS	94.9	94.0	87.2	3.472	3.374	3.487	5.045	5.018
B	TS	101.2	94.8	85.9	3.528	3.304	3.611	5.280	5.096
Ge	TS	94.5	94.5	87.0	3.481	3.581	4.477	5.041	5.036
As	TS	93.4	91.7	91.7	3.544	3.294	3.572	4.979	4.931

Table 4.5: Geometry parameters of the oxygen monomer ground state (GS) and transition state (TS) configurations (see Figure 4.7 for notations). The length values are in Bohrs, the angles are in degrees. The bulk Si-Si bond length is 4.468 Bohr.

However, significant changes in the transition state geometries were observed. Both boron and arsenic presence in the supercell leads to the same changes in the monomer geometries. The Si_1-O and Si_3-O bond lengths are increased from ~ 3.480 Bohr to $\sim 3.530 - 3.610$ Bohr, while the Si_2-O bond length is reduced from ~ 3.370 Bohr to ~ 3.300 Bohr in both cases. Ge presence does not affect much the transition state geometry of the monomer.

In the case of the dimer, the most significant deviation of transition state geometry occurs in the case of As, while the other dopants cause only minor changes, which can be neglected.

In brief, we observe no impact on ground state configurations of both the monomer and the dimer, however, both B and As doping significantly impacts the transition state configurations of the monomer, while As impacts that of the dimer.

Migration and binding energies. The effect of dopants on the migration energies of diffusing oxygen species is represented in Table 4.7. The migration energy of the oxygen monomer is reduced by ~ 0.4 eV due to the presence of p-type dopants. Notably, n-type dopants also lead to a reduced migration energy but at a smaller

doping	Conf.	$\hat{a}$	$\hat{b}$	$\hat{c}$	$\hat{d}$	$\hat{\mathrm{Si}}_{123}$	$\hat{\mathrm{Si}}_{234}$	$\mathrm{Si_1}$-$\mathrm{O_I}$	$\mathrm{Si_2}$-$\mathrm{O_I}$	$\mathrm{Si_3}$-$\mathrm{O_I}$	$\mathrm{Si_2}$-$\mathrm{O_{II}}$	$\mathrm{Si_3}$-$\mathrm{O_{II}}$	$\mathrm{Si_4}$-$\mathrm{O_{II}}$
–	GS	142.7	71.6	145.1	60.9	97.2	98.6	3.093	3.053	6.040	3.037	3.088	4.985
B	GS	142.5	70.9	146.2	59.5	98.3	100.2	3.090	3.061	6.090	3.035	3.085	5.090
Ge	GS	142.6	71.0	146.6	59.4	98.2	100.3	3.093	3.067	6.094	3.038	3.083	5.100
As	GS	142.6	71.0	146.6	59.4	98.2	100.3	3.093	3.067	6.095	3.038	3.083	5.101
–	TS	88.2	95.7	101.5	79.8	95.0	97.4	3.834	3.257	3.536	3.262	3.244	4.098
B	TS	83.6	99.0	98.1	84.4	95.7	95.6	3.962	3.257	3.357	3.393	3.265	3.936
Ge	TS	83.4	98.7	99.4	82.3	95.8	96.7	3.956	3.261	3.363	3.339	3.256	4.040
As	TS	76.8	102.6	95.6	85.6	99.4	96.7	4.111	3.225	3.298	3.603	3.249	3.769

Table 4.6: Geometry parameters of the oxygen dimer ground state (GS) and transition state (TS) configurations (see Figure 4.8 for notations). The length values are in Bohrs, the angles are in degrees.

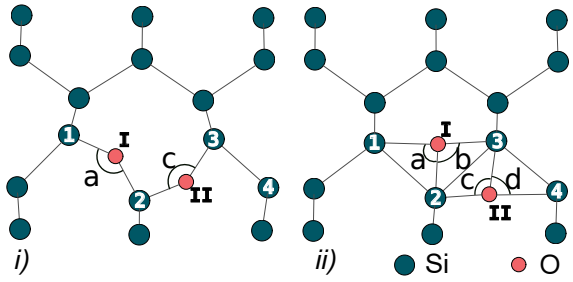

Figure 4.8: Oxygen dimer's *i)* ground state and *ii)* transition state configurations. In Table 4.6, $\hat{\text{Si}}_{123}$ and $\hat{\text{Si}}_{234}$ angles are defined in the same manner as in Figure 4.7.

extent of ~ 0.15 eV. Germanium presence does not affect the monomer's migration energy.

dopant	–	B	Al	Ga	Ge	P	As	Sb
$E_m(O)$ [eV]	2.41	2.01	2.04	2.05	2.39	2.26	2.29	2.24
$E_m(O_2)$ [eV]	1.62	1.66	1.63	1.62	1.74	1.75	1.71	1.74
$E_b(O_2)$ [eV]	0.14	0.15	0.15	0.14	0.14	0.14	0.14	−0.39

Table 4.7: The calculated migration and binding energies of oxygen species in proximity of various dopants.

The effect of dopants on the dimer's energy barrier has the opposite trends. There is almost no effect of p-type dopants, while there is slight increase by ~ 0.1 eV caused by n-dopant and isovalent dopants.

There is no significant changes in the dimer's binding energy, being 0.14 ± 0.001 eV in most tested cases. The impact of these dopants will be discussed in more detail in Subsection 4.4.2, whereas here we will focus on a specific case of antimony doping.

In the latter case, we obtained a negative binding energy of -0.39 eV for dimers, suggesting that they should not be formed in proximity of antimony and thus the O_{2i} concentration should decrease significantly. We also observe that Sb atom traps the oxygen monomer with a trapping energy of 0.52 eV, whereas no trapping is observed for the other dopants for the same dopant-O_i distance (15 Å). Thus, we suggest, that in the heavily Sb doped case, the primary migrating particle is the oxygen monomer. The effective activation energy is a function of the migration and binding energies of O_i and O_{2i}, as well as the O-dopant trapping or binding energies.

The exact quantification of this effective diffusion would require an exhaustive study of the sink strength of the dopant, including the possible formation of oxygen-dopant complexes. This is beyond the scope of the present study that aims to identify the involved mechanisms only. Still a lower bond of 2.76 eV, can be given for antimony case as the sum of monomer migration and trapping energies. This value is close to the reported increase of migration energy in Sb-doped samples [126]. With

this mechanism, the Sb-retarded oxygen diffusion originates from two thermodynamic effects coming together: *i)* negative binding energy of O dimers, and *ii)* long-range trapping of O monomers by Sb atoms. Such trapping mechanism will lead to an increased activation energy. Moreover, the retardation should be sensitive to the ratio between dopant and oxygen and should vanish at high enough temperature.

Pre-exponential factors. To have a full picture of diffusing properties and to make the final conclusions, we lack the calculation of the pre-exponential factors calculations. These values for representative cases of B, Ge, and As are listed in Table 4.8. For the dimer case, we represent the low temperature effective pre-exponential factor, which is derived using Expression (4.6). The oxygen monomer concentration was considered as 10^{18} cm^2s^{-1} in all cases. Note, that $D_0(O_2)$ is proportional to the oxygen concentration. Thus, the reduction of the latter by one order in magnitude will cause the same one order reduction in the pre-exponential factor.

dopant	–	B	Ge	As
$D_0(O)$ $[cm^2s^{-1}]$	$2.9 \cdot 10^{-2}$	$3.2 \cdot 10^{-2}$	$4.0 \cdot 10^{-3}$	$9.0 \cdot 10^{-3}$
$D_0(O_2)$ $[cm^2s^{-1}]$	$2.54 \cdot 10^{-7}$	$0.55 \cdot 10^{-7}$	$2.62 \cdot 10^{-7}$	$4.85 \cdot 10^{-7}$

Table 4.8: Calculated pre-exponential factor values

Boron leads to an important impact on the migration energy, but we only observed a slight change in the prefactor value. The effects of germanium and arsenic are more pronounced. Our calculations suggest, that in germanium doped case the pre-exponential factor is lower by a factor of 8, whereas As suggests the reduction by a factor of 4. The corresponding values are 0.004 $cm^{-2}s^{-1}$ and 0.009 $cm^{-2}s^{-1}$ in the case of germanium and arsenic doping, respectively. The doping effect on the dimer's pre-exponential factor shows an inverse trend. The isovalent doping nearly does not impact the pre-exponential factor, whereas arsenic slightly increases it by a factor of 2, and boron reduces it by a factor of 5.

4.4.1 Charge transfer mechanism

Prior to discuss the calculated diffusion coefficient as a function of temperature in heavily doped material, we consider the physical insight responsible for the changes in diffusion properties of oxygen species. For this purpose we performed NEB calculations to find the minimum energy diffusion path of oxygen monomer in the 216 Si supercell. This supercell size indicates a good balance between the accuracy and the computational cost: NEB calculations in our case are 41 (number of images along the diffusion path) times more expensive than the single point optimization,

that is why we avoid doing such calculations in the 512 Si supercell. We compared the diffusion in proximity of boron and arsenic dopants with diffusion in nondoped supercell. The boron and arsenic are chosen as two prototypes for p- and n-type dopants. In the 216 Si supercell, the migration energies obtained with DIIS scheme and using the NEB technique are 2.41 eV and 2.35 eV, respectively. The slightly lower value obtained using NEB technique is related to the elastic bands that restrict the images along the migration path. The path of 41 images resulted in a highly symmetric curve with a transition state situated very close to the middle of the path. Moreover, the identical results in 216 Si and 512 Si (2.41 eV and 2.40 eV, respectively) prove that 216 Si supercell is a good model for a 512 Si box.

	216 Si		512 Si	192 Si
	DIIS	NEB	DIIS	DIIS
E_m [eV]	2.41	2.35	2.40	2.29

Table 4.9: The calculated migration energies depending on the supercell size and the transition state optimization technique.

The obtained NEB paths as a function of reaction coordinates are represented in Figure 4.9 for pristine, boron and arsenic containing silicon. The changes of the barrier height due to the dopants presence also agree well with previously obtained values. The NEB values are systematically underestimated by 0.1-0.2 eV compare to the results of DIIS optimization. The three curves of Figure 4.9 are merged starting from the ground state and they start splitting after the inflection point. To analyze the electronic distribution of the treated supercells, we have mapped the electronic density of the unpaired electron for the cases of B and As doped supercells (see Figure 4.10). Numbered points correspond to the NEB image numbers labeled in Figure 4.9.

Indeed, Figure 4.10 represents the electronic density of an odd electron, mapped along the NEB paths. It clearly indicates that starting from the ground state and up to the image number 4 oxygen diffuses as a neutral species. At the points number 5 in Figure 4.9, the charge is already located around the oxygen. This finding indicates, that monomer diffusion in heavily doped silicon is assisted by a charge transfer. This charge is a hole in the B doped case and electron in the As doped case.

We now use the Wannier analysis to get more detailed insight for the electronic distribution and charge transfer mechanism. We only performed the analysis of ground state and transition states configurations, skipping other configurations along the path. For the ground state configuration, the electronic distribution around oxygen is similar to the intrinsic case for all tested dopants (see Figure 4.2 *a*). This fact is in line with previous observations of ground state geometry parameters, which were not affected by any of tested dopants. Thus the effect should lie in the transition

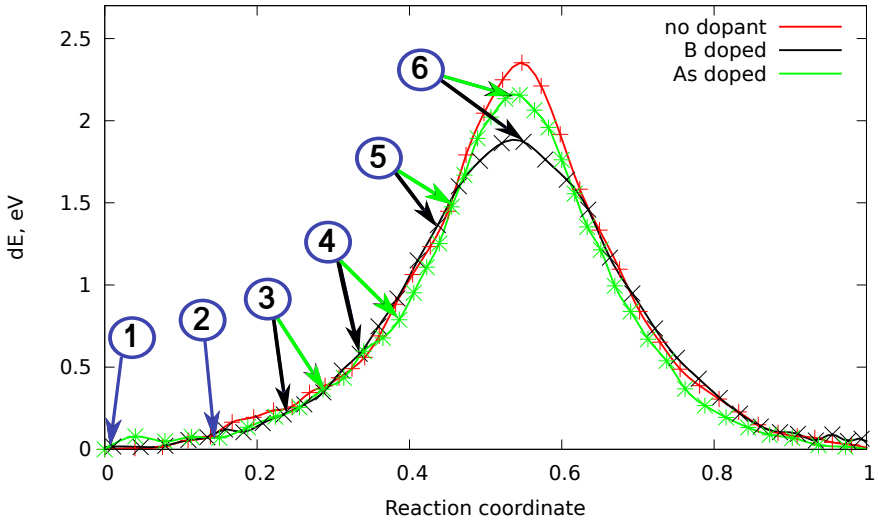

Figure 4.9: The 41 images NEB paths of oxygen monomer in 216 Si atoms supercells. Results for B and As doped supercells are compared with undoped supercell. Figure 4.10 illustrates the snapshots of up-down electronic density corresponding to *1)* 1^{st}, *2)* 5^{th}, *3)* 9^{th}, *4)* 13^{th}, *5)* 17^{th}, and *6)* 21^{st} images of B and As doped cases.

state configuration.

The rearrangement of the electronic structure of oxygen in the *Y-lid* configuration is reported in Fig. 4.11, where Wannier centers for spin up and spin down electronic density are depicted separately. In the B-doped case, the relative arrangement of spin-up Wannier centers is very similar to the intrinsic case: a lone pair is near the Si^2 atom, while it is not the case for the spin-down electrons (Fig. 4.11 *a-b*). Indeed, the corresponding spin-down center of Si^2 is now empty as the electron is located on the B atom. The addition of a second boron has the same effect on the spin-down center of Si^2: its lone pair disappears completely. The relocation of the second electron results in an decrease of E_m by 0.08 eV. In the As-doped case, the relative arrangement of the Wannier centers with spin-down is similar to the intrinsic case. spin-up Wannier centers display a more complicated figure: the Wannier center nearby Si^2 is suppressed and all three silicon atoms are bond to each other (Fig. 4.11 *e-f*). An additional electron provided by a second As atom leads to an almost identical symmetric state for spin down (Fig. 4.11 *g-h*). The corresponding electronic rearrangement does not cause changes in the migration energy. The above Wannier analysis demonstrates that the E_m reduction is driven by a charge transfer (hole or electron) between the dopant and the oxygen at the transition state configuration.

The charge transfer mechanism occurs in the dimer diffusion as well, but causing only slight increase in its migration energy. The reason for that could lie in the electronic configuration of the transition state of the dimer. Contrary to the monomer

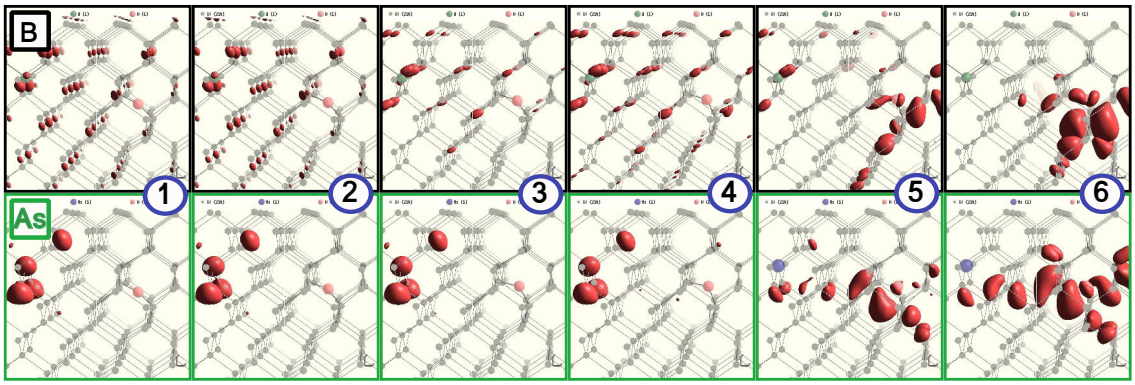

Figure 4.10: The up-down electronic density $\rho^{unpaired}(\vec{r})$ ($\rho^{unpaired}(\vec{r}) = \rho_{\uparrow}(\vec{r}) - \rho_{\downarrow}(\vec{r})$) mapped along the oxygen monomer migration path for B and As dopant cases (see Figure 4.9). Number *1* corresponds to the ground state of oxygen monomer, while number *6* is related with the transition state. The dopant atom is located on the right side of each snapshot, while the migrating oxygen is on the left side. The electron density transfers from the dopant vicinity (numbers *1-4*) towards the migrating oxygen (numbers *5-6*).

case, it is less active. During the migration process, two hopping bonds of two oxygen atoms can be neutralized by each other, causing a lower migration barrier, which is less sensitive to the charge transfer mechanism.

4.4.2 Discussion on effect of doping on oxygen diffusivity

Our *ab initio* calculations provide migration energy values, which are in excellent agreement with experimental data. The results were obtained in 512 Si supercell by employing a DIIS optimization scheme for the saddle point optimization. For the oxygen monomer diffusion we performed a highly accurate NEB calculations in 216 Si supercell. The obtained geometries and the energies of the saddle point configuration are in a good agreement with those of DIIS optimization scheme.

Recently, in 2014, Binder *et al* [10] have performed an *ab initio* study of oxygen migration path in pristine silicon. By employing the NEB techniques, they have obtained an asymmetric path for oxygen monomer diffusion, which contradicts with our highly symmetric path for the same case. The reason of the disagreement between two studies lies in methods that were used to construct and optimize the migration path. Binder *et al* have optimized the path in 64 Si atoms supercell. Such a supercell size causes an artificial interactions between periodical images. Thus, the obtained path cannot reproduce the potential energy surface of the realistic diffusion jump. Although they have performed calculations in bigger supercells (216 Si and 512 Si), they have adopted the constrained geometry of the NEB images from the 64 Si supercell, and therefore all the errors from the artificial interactions with periodical images have been adopted as well.

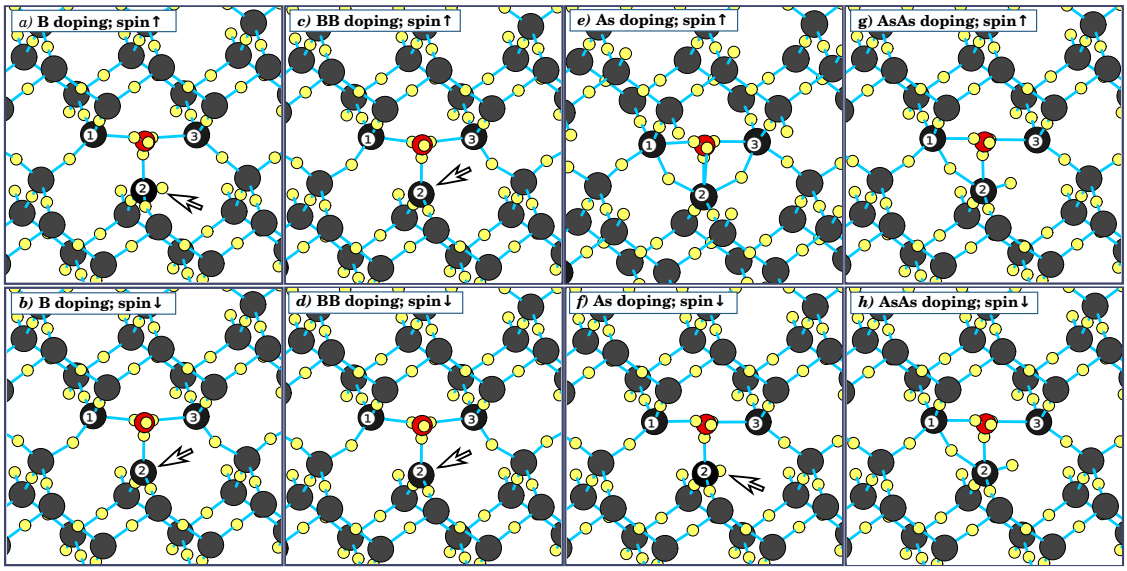

Figure 4.11: Saddle configurations of O_i monomer with additional dopant(s) in the supercell a) B b) B + B c) As d) As + As. The dopants and oxygen atoms are separated by about 15 Å within supercell, thus the dopants are not visible in the figure. Atoms and Wannier centers use the same schematic conventions as in Figure 4.2. The upper line of configurations represents spin up while the line below is used for the spin down channel. We can observe that B-doping suppresses lone-pairs around Si_2, while As-doping creates additional bonding between Si_1, Si_2 and Si_3.

Contrary to the just described case, in the present study, we optimized the whole supercell without any constrains on any of atoms. For pristine silicon, the calculated values reproduce the experiments, the monomer diffusion at high temperature regime and dimer diffusion at low temperature regime. In addition, our results show that strain cannot affect oxygen diffusivity. However, we observed that heavy doping can impact the oxygen diffusivity by electronic interaction, specifically by the charge transfer mechanism. This effect is demonstrated in Figure 4.10. Indeed, a dopant belonging to the III column of the periodic table introduces a hole into the supercell. The latter can be spread over a wide area around. The electronic density of this hole is revealed by the $\rho^{unpaired}(\vec{r})$ map obtained from DFT calculations 1 top in Figure 4.10. In the case of the n-type dopant, the supercell has also an odd number of electrons. Here, the unpaired electron belongs to the dopant atom and is localized in a small sphere around it. If we map the $\rho^{unpaired}(\vec{r})$ electronic density, we get the distribution of the additional electron of the V column element, as reported in the bottom image 1 in Figure 4.10.

The binding energy between the oxygen monomer and a dopant, being B or As, is equal to zero in both cases. These results are in line with the fact that geometry parameters of the interstitial oxygen are the same in these cases and in pristine silicon. The potential energy surface has exactly the same shape, according to the shape of the NEB curves. The NEB paths in all three cases, namely pristine, B-containing,

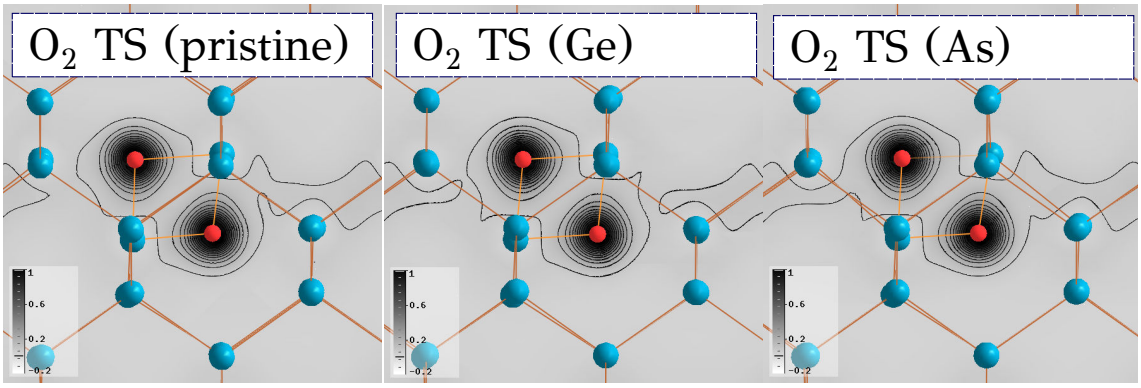

Figure 4.12: The electronic density distribution around transition state of the oxygen dimer in pristine silicon supercell, as well as in Ge and As containing ones.

and As-containing, are merged in ranges of 0.0-0.4 and 0.6-1.0 of reaction coordinates.

Once the oxygen approaches the transition state, it becomes electrically active and attracts the electronic density towards itself. This effect is illustrated by the $\rho^{unpaired}(\vec{r})$ distribution: top and bottom images (5) and (6) on Figure 4.10. A hole is attracted in B doped case and an electron is attracted in As doped case. Once the oxygen atom overpasses the transition state, the electron goes back to the dopant.

Such a charge transfer mechanism allows reducing the migration energy barrier, if a charge electron detaches easily from its source. In the case of B doping, we obtained a reduction of monomer migration energy by 0.4 eV. However as we showed, the second B added to the system leads only to a slight reduction in migration energy of 0.08 eV. Thus we conclude, that $\sim$ 0.4 eV is the highest possible reduction for the oxygen monomer's migration energy. Our calculations predict the same effect on migration energy in the presence of the other p-type dopants. If the element is a n-type dopant, the charge transfer leads to a smaller reduction of the migration energy of only 0.15 eV.

In proximity of p- and n-type dopants, the dimer diffusion is also charge assisted, according to our results. However we did not register a considerable changes of the migration energy in proximity p-type dopants, and we detect only a slight increase of 0.15 eV in proximity of As dopant.

Doping with germanium does not affect the migration energy of the monomer, however it leads to an increase of 0.15 eV of that of dimer. The exploration of the electronic density around the transition state of the dimer shows a slight difference between pristine and Ge-doped cases 4.12. Therefore, we attribute the difference in the migration energies to the electronic effect of Ge presence.

4.5 Mechanisms of enhanced and retarded oxygen diffusion

The complete comprehension of diffusing properties implies the investigation of the temperature dependence of the calculated diffusion coefficients. In Figure 4.13, the calculated diffusion coefficients of the oxygen monomers and dimers are plotted together with experimental data from References [60, 93, 139] with respect to inverse temperature.

First, it is worth to notice, that Ge and As doping should affect diffusion coefficients of monomer and dimer in the same extent. An impact of both dopants on the migration energy and pre-exponential factor of oxygen dimer lead to a similar reduction in the diffusion coefficient that fully agrees with experimental trends from Reference [139]. More specifically, in both cases, slight increase in migration energies leads to a steeper slope of Arrhenius plot and results in lowered diffusion coefficient of oxygen dimer at low temperatures. At high temperatures, we obtained slightly reduced monomer's diffusion coefficients in proximity of Ge and As. This effect is related with the decrease in pre-exponential factor of monomer with respect to pristine silicon, while migration energies is not affected.

In thermodynamic equilibrium, the diffusion of the oxygen dimer in proximity of boron proceeds with lower diffusion coefficient. That suggests retarded dimer diffusion (see Figure 4.13). This finding is reverse to the experimentally observed enhanced oxygen diffusion in the heavily boron doped samples. However, the calculated diffusion coefficient for the monomer is enhanced and passes through the experimental points (see Figure 4.13). These results states for the significantly enhanced monomer diffusion at low temperature regime, which is driven by the charge transfer mechanism.

This finding raises a question how monomers diffuse in the high temperature regime in heavily B-doped silicon. According to our calculations, the diffusion should be enhanced in a large extent; however, recent experiments suggest "normal" diffusion at high temperatures in heavily B-doped sample [138, 131]. Thus, we suggest that potential energy profile can be temperature dependent. As a result, at high temperatures, "normal" diffusion can take place in heavily boron-doped samples. In other words, the oxygen monomers diffuse via the charge assisted mechanism in cases, when the thermal energy is not enough to proceed through the "normal" diffusion mechanism.

It is important to notice, that the reduction of the migration energy, assisted by a charge, can be a reason of the enhanced oxygen diffusion in a hydrogen enriched samples as well as in samples with metallic impurities. Weakly binded electrons can participate in the diffusion process, causing a reduced migration energy.

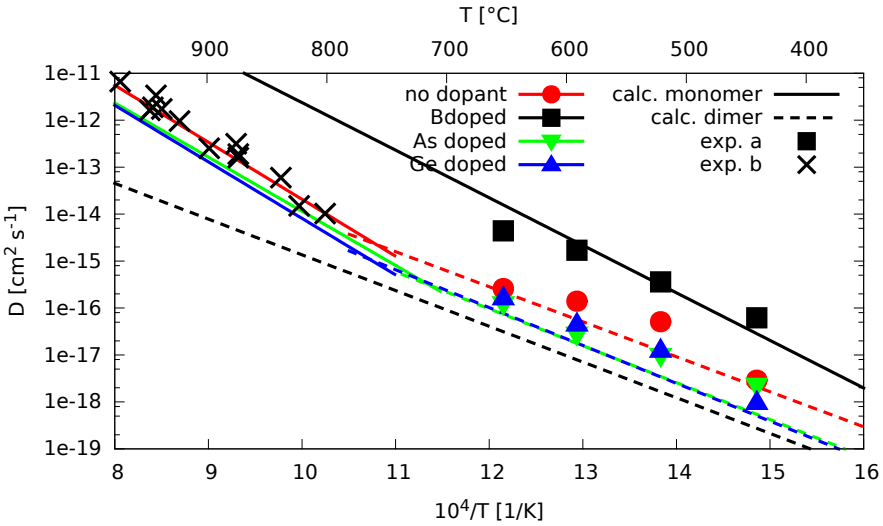

Figure 4.13: Calculated diffusion coefficients of oxygen monomers and dimers. [a] Reference [60]; [b] Reference [117].

Experimentally, migration energies of about 2 eV have been obtained in hydrogen and metallic impurities presence [85, 96, 130]. This value is equal to the lowest migration energy of monomer obtained in our calculations and it can be related to the similar effects.

4.6 Conclusions

In this study, we have investigated the diffusion properties of oxygen species through DFT based calculations. Firstly, we calculated the diffusion coefficients of oxygen monomers and dimers in pristine Si. Then we studied the impact of uxiaxial and biaxial external strain on the monomer's and dimer's migration energies. We have also calculated the diffusion coefficients of oxygen monomer for the two representative external biaxial strains. And finally, we investigated the impact of heavy p-type, n-type, and isovalent doping on diffusion coefficient of both monomers and dimers.

We showed that DFT can effectively reproduce the experimentally obtained diffusion coefficient at high and low temperature regimes. Our calculations supports the idea that oxygen monomers diffuses at high temperatures, while dimer is responsible for the transport of oxygen at low temperatures.

We also showed that external strain, uniaxial or biaxial, does not impact the migration energy. Strains of ±1% lead to a maximal effect of about ±0.1 eV. Thus strains introduced by high content of dopants cannot cause remarkable changes in the oxygen diffusing properties.

The impact of dopants on electronic properties is more significant. At low

temperatures, the dimers diffusion dominates in the presence of most dopants with two exceptions: boron and antimony. As far as the migration energy of monomer close to Al and Ga is also reduced, we assume that the same effects as in B case takes place for the monomer's diffusion coefficient. We have also found a reduced diffusivity of dimers in the presence of germanium and arsenic that is caused by a slight increase in dimer migration energy of 0.15 eV. Moreover, we infer that other n-type dopants, phosphorus and antimony, behave similarly, as the same effect on migration energies was observed.

In the proximity of boron, a reduction of the pre-exponential factor results in retarded diffusion coefficient of dimer. However, the monomer diffusion is significantly enhanced due to a charge transfer mechanism. Thus we conclude, that monomers enhanced diffusivity is responsible for an enhanced transport in heavily boron doped silicon. In order to verify this theoretical observation, we suggest the following experiment: the oxygen transport at low temperatures should be measured, by keeping the same boron concentration and varying that of oxygen. Diffusivity of oxygen monomer should not vary, as it does not depend on concentration contrary to that of dimer.

Chapter 5

On carbon doped and isovalently co-doped electron irradiated silicon

This chapter addresses the questions of the population and the thermal evolution of secondary radiation induced defects in isovalently doped (C, Ge) co-doped (C-Ge, C-Sn, C-Pb) crystalline Cz-Si [1]. Experiments cannot provide the exhaustive registration and identification of all complexes, therefore some vacancy-, interstitial-, and carbon-related defects can be missing. Possible defect associations and their thermodynamic properties can be identified by means of DFT calculations, whereas temperature evolution of the these complexes can be calculated by using the kinetic mass action low. Here, we consider the thermodynamic and kinetic aspects of complexes formation through IR absorption experiments as well as through multiscale simulations. This work has been done in collaboration with researches from the University of Athens [2], who provided all the IR experimental data for this study, and with Gilles Brenet [3], who has implemented and applied the kinetic mass action law (KMAL) to study the temperature evolution of the complexes population in irradiated samples.

5.1 Introduction

The investigation of electron irradiated silicon is important due to several reasons. First of all, physics of electron irradiated material is crucial for specific operational environment, such as space, medical laboratories, and particle accelerators. Second, the investigation of defect interactions is important for photovoltaics (PV) and microelectronics (ME) industry. Indeed, PV and ME devices are suffering from the

1. Results presented in in this Chapter have been partially published in References [119, 118, 84].
2. Group of C.A. Londos from the Solid Physics Section of University of Athens (Greece)
3. PhD student from the L_Sim laboratory, CEA-Grenoble (France)

defect complexes. However, as concentration of defects is low, it is barely possible to detect them and study their impact on properties. For this reason, intentionally doped samples can be studied, while electron irradiation can be used to stimulate Frenkel pairs formation and to accelerate point defects interactions. Besides all practical reasons, this study gives a fundamental atomistic insight into defect interactions and complexes formation in crystalline silicon.

The scope of the present chapter is the following. Firstly, we experimentally investigate the effect of isovalent dopants (C, Ge, and Pb) on the production and the thermal stability of the complexes made of vacancies, interstitial oxygen, substitutional carbon, and interstitial carbon, namely VO_i, C_iO_i and C_iC_s pairs. We assess the hardening potential of isovalent dopants on these pairs. Secondly, we intend to obtain a microscopic insight into irradiation-caused defects formation and their stability. To that purpose, we perform a systematic theoretical study of most possible defect pairs formation and their temperature evolution.

5.2 Experimental data

In this work, we have investigated five groups of Cz-silicon samples [4]:

1. a low carbon concentration sample labeled $C_L\,CzSi$;
2. a low carbon concentration germanium doped sample labeled $C_L\,CzSi{:}Ge$;
3. a high carbon concentration sample labeled $C_H\,CzSi$;
4. a germanium-carbon co-doped sample labeled $C_H\,CzSi{:}Ge$;
5. a lead-carbon co-doped sample labeled $C_H\,CzSi{:}Pb$.

All samples were irradiated with 2 MeV electrons at about ~ 80℃, with a fluence of $1 \cdot 10^{18}\ cm^{-2}$. Table 5.1 represents the concentrations of O_i and C measured prior and after the irradiation course as well as concentrations of Ge and Pb dopants.

Sample	$[O_i]_{bi}$	$[O_i]_{ai}$	$[C]_{bi}$	$[C]_{ai}$	[Ge]	[Pb]
$C_L\,CzSi$	95	91	5.0	< 2.0	—	—
$C_L\,CzSi{:}Ge$	52	43	4.4	< 1	400	—
$C_H\,CzSi$	93	90	22	13.2	—	—
$C_H\,CzSi{:}Ge$	...	...	10	2.9	400	—
$C_H\,CzSi{:}Pb$	21	15	19	< 1	—	100

Table 5.1: The concentrations of Ge and Pb ([Ge] and [Pb]) as well as the concentrations of O_i and C before irradiation (bi) ($[O_i]_{bi}$ and $[C]_{bi}$) and after irradiation (ai) ($[O_i]_{ai}$ and $[C]_{ai}$). Concentrations are given in 10^{16} cm^{-3}.

4. The experimental data have been provided by our Greek colleagues, but presented analysis of these data was done by myself.

Figures 5.1 show the IR spectra of the *C_LCzSi*, *C_LCzSi:Ge*, *C_HCzSi*, *C_HCzSi:Ge*, and *C_HCzSi:Pb* samples respectively recorded prior and after irradiation. Bands at 830 cm^{-1} (VO_i), at 862 cm^{-1} (C_iO_i), at 546 cm^{-1} (C_iC_s) as well as the pair of bands at 936, 1020 cm^{-1} related to the (C_iO_iI) are present as expected in all the samples. However, for the *C_LCzSi:Ge* sample the spectral range below 600 cm^{-1} is very noisy and the 546 cm^{-1} band is obscured by this noise. Instead, the concentration of C_iC_s complex was measured using the 7819 cm^{-1} band, which is out of the range of Figure 5.1. The concentrations of a point defects is proportional to the intensity of its absorption band, the proportionality coefficient is empirical and is generally called as a calibration coefficient. A calibration coefficient of $4.2 \cdot 10^{16}$ cm^{-2} has been applied in the case of the 7819 cm^{-1} band. The rest of coefficients are usual and can be found in the corresponding literature [119, 84, 79, 76, 32, 26, 67, 82]. Figures 5.2 present the thermal evolution of the VO_i, C_iO_i, and C_iC_s pairs, respectively. The thermal evolution of the 546 cm^{-1} band cannot be monitored properly. The band disappears above $\sim$ 300 ℃ but its decay cannot be followed because of the noise and therefore it is not presented in Figure 5.2 *(c)*.

	$[VO_i]$	$[C_iO_i]$	$[C_iC_s]$	$[C_iO_iI]$	$R_{V/I}$
C_LCzSi	5.80	3.00	0.56	0.23	1.53
C_LCzSi:Ge	4.94	2.53	0.80	0.49	1.29
C_HCzSi	6.06	5.72	1.01	0.46	0.84
C_HCzSi:Ge	3.75	2.86	0.34	0.30	1.07
C_HCzSi:Pb	3.31	1.87	0.45	0.30	1.26

Table 5.2: The final concentrations, or production, of the VO_i, C_iO_i and C_iC_s pairs for the various samples, measured immediately after the electron irradiation. $R_{V/I}$ presents the calculated ratio of vacancy-related pairs (VO_i) to interstitial related detected clusters (C_iO_i, C_iC_s, and C_iO_iI). Concentrations are given in $10^{16} cm^{-3}$.

Table 5.2 represents the production of VO_i, C_iO_i, and C_iC_s pairs in all considered samples, while Figures 5.2 represent their temperature evolution. Hereafter, we consider these samples in detail and will derive some important conclusions.

5.2.1 Carbon-poor and carbon-rich samples. Impact of carbon on irradiation caused defects

Let us first consider carbon and oxygen containing silicon (*C_LCzSi* and *C_HCzSi*). The concentrations of the detected oxygen and carbon-related complexes are reported in Table 5.2. Upon irradiation, most of the vacancies, which survive annihilation with self-interstitials, are captured by oxygen atoms to form VO_i pairs. In a first approximation, we neglect that some of the produced vacancies pair together to form di-vacancies. The concentration of VO_i defects can thus be taken as a measure of

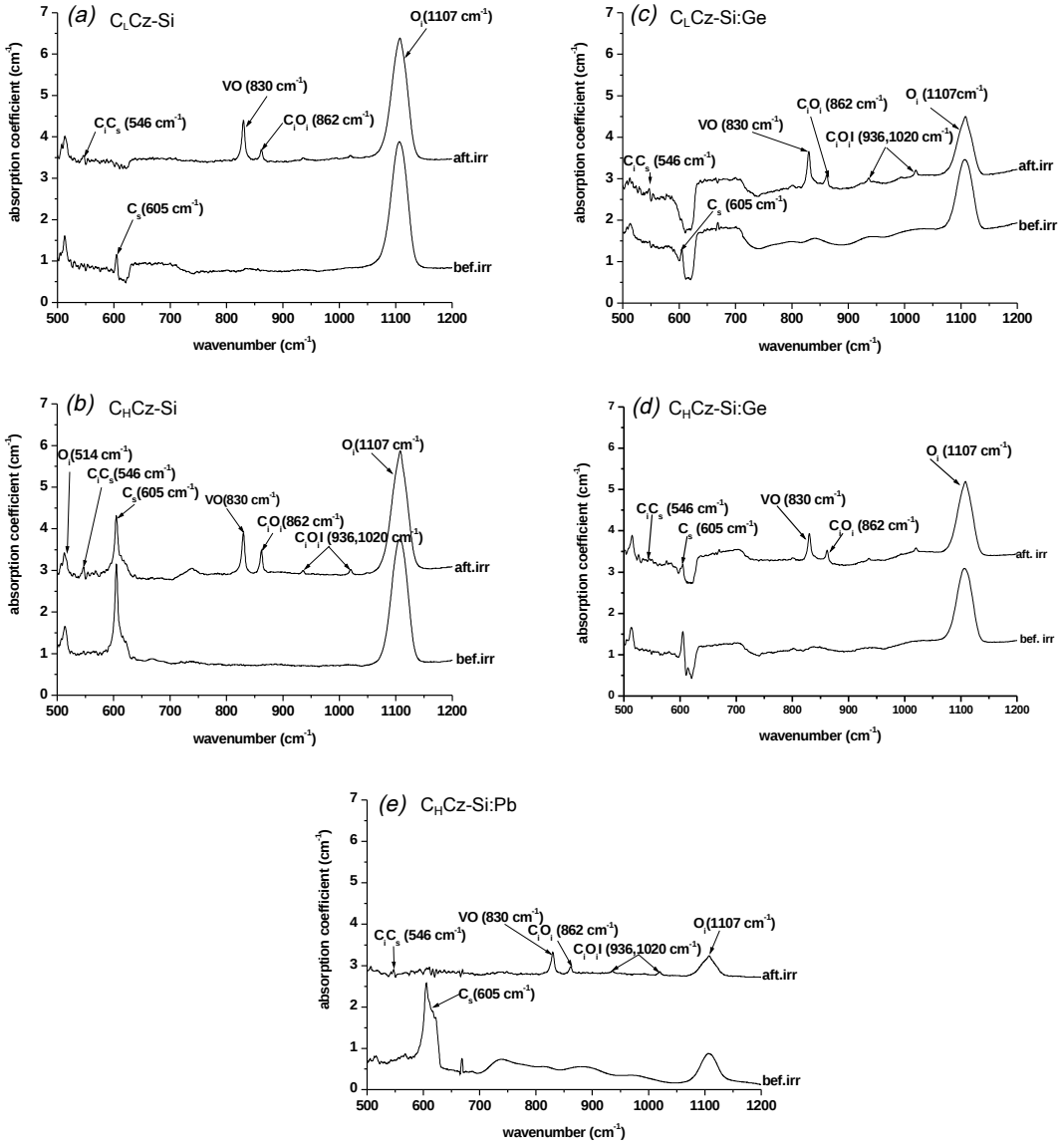

Figure 5.1: IR absorption spectra of the (a) $C_L CzSi$, (b) $C_H CzSi$, (c) $C_L CzSi{:}Ge$, (d) $C_H CzSi{:}Ge$, and (e) $C_H CzSi{:}Pb$ samples recorded prior and after electron irradiation. Spectra after irradiation are shifted for the sake of clarity.

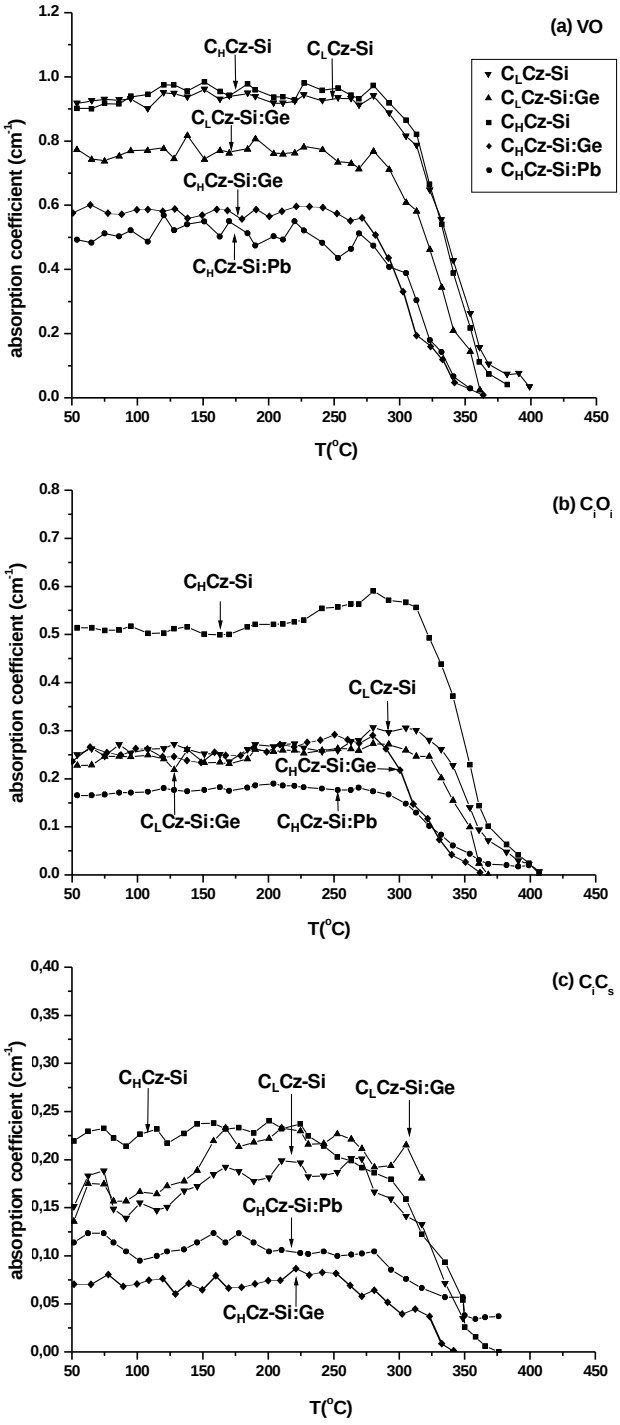

Figure 5.2: The production of the (a) VO, (b) C_iO_i, (c) C_iC_s pairs for *C_LCzSi*, *C_HCzSi*, *C_LCzSi:Ge*, *C_HCzSi:Ge*, and *C_HCzSi:Pb* samples.

the surviving vacancies concentration. At the same time, the same number of self-interstitials survives annihilation with vacancies. And most of the silicon interstitials I can be captured by substitutional carbon atoms, that leads to the formation of carbon interstitials (C_i). C_i atoms are very mobile at room temperature and interact promptly with remaining O_i and C_s to form C_iO_i, C_iC_s, and C_iO_iI defects. Three defect complexes, namely VO_i, C_iO_i, and C_iC_s, are the main irradiation induced complexes (secondary irradiation induced defects), which production rates will be investigated below. The concentration of the C_iO_iI complex is comparatively small, it fully depends on C_iO_i concentration, thus it is not of a particular attention hereafter.

VO_i The VO_i complex formation and the temperature evolution of its concentration are independent from carbon content in the sample. The complex is stable up to 250 ℃. Above 350 ℃ the complete dissociation of VO_i pairs is observed (Fig. 5.2).

C_iO_i Contrary to the previous complex, C_iO_i formation is by definition sensitive to carbon concentration in the sample. While carbon concentrations in *C_H CzSi* sample is four times higher than in *C_L CzSi*, the C_iO_i concentration in the former sample is about twice higher than that of the latter sample. The temperature evolution of the corresponding band shows that the complex is stable up to 320 ℃. Notably, lasting from 250 to 350 ℃ a small bump takes place on both temperature evolution curves. The origin of this phenomenon is obscure and is not discussed in literature, so far.

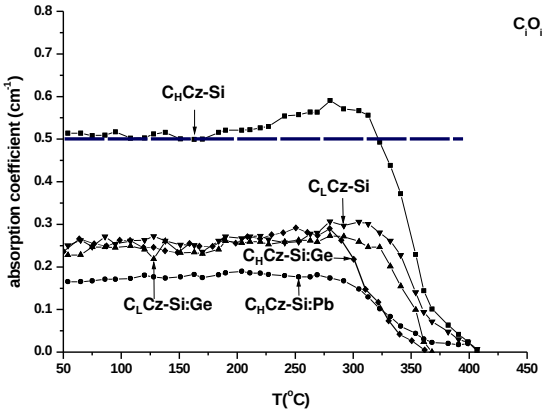

Figure 5.3: Temperature evolution of C_iO_i complex.

C_iC_s As in the previous case, the C_iC_s complex formation obviously depends on carbon concentration. It is twice higher in *C_H CzSi* sample than in *C_L CzSi*. Moreover, C_iC_s bands vary differently with temperature, although the reason of this phenomenon is not clear. In the *C_H CzSi* sample, the C_iC_s concentration remains stable up to 250 ℃. It starts to dissociate slowly above this temperature and reaches

the full dissociation at about 370 ℃. In the *C_LCzSi* sample, the C_iC_s band gradually increases with temperature until 320 ℃ and then slowly disappears.

5.2.2 Carbon-germanium co-doped silicon samples

The impact of Ge doping of Si samples will be studied using two germanium containing samples: *C_LCzSi:Ge* and *C_HCzSi:Ge*. The former sample only contains Ge, while the latter one is isovalently co-doped. The first sample allows to study the pure effect of Ge presence, while the second allows comparing the C-Ge and C-Pb doped samples and their impact on secondary electron-irradiation induces point defects.

VO_i Ge presence leads to a reduced production of VO_i pairs. Interestingly, the reduction rate depends on carbon concentration. Thus we conclude, that not only the absolute concentrations of dopants are significant, but also the relative ratio of co-dopants concentrations. The impact of carbon concentration in carbon-germanium containing samples have been investigated by our experimental colleagues in Ref. [77] in details. Particularly, it was reported that annealing temperature of VO_i pair is substantially lowered, and it was related to the pair of reactions: $VO_i + I \rightarrow O_i$ and $VO_i + O_i \rightarrow VO_{i2}$.

C_iO_i The production of C_iO_i pair is similar in two cases. However, in *C_HCzSi:Ge* sample, the C_iO_i dissociation starts at lower temperatures of about 270 ℃ compare to *C_LCzSi:Ge* sample. This observation can not be disentangled easily, as far as carbon and germanium contents are different in these two samples.

C_iC_s The formation rate differs by a factor of 2 in these two samples. Depending on carbon content, qualitatively different temperature evolution curves were obtained. In *C_HCzSi:Ge* sample, the number of complexes is reduced and remains unchanged up to 250 ℃. When the temperature is further increased, C_iC_s concentration slowly reduces and reaches zero at 350 ℃. In *C_LCzSi:Ge* sample, the same monotonic increase in C_iC_s concentration appears with temperature increase as in *C_LCzSi*. The corresponding band quenches at about 350 ℃.

5.2.3 Carbon-lead co-doped silicon samples

The covalent radius of Pb is significantly bigger than that of Si atoms. Therefore, Pb introduces compressive elastic strains in silicon crystal and it cannot be present in significant concentrations. To overcome this difficulty, silicon can be co-doped

with lead and carbon. Compressive and tensile strains of two dopants compensate and desired concentrations of lead can be reached.

VO_i The VO_i production in Pb-C co-doped sample is the lowest among studied samples, showing that heavy C-Pb incorporation can be used to reduce the undesired VO_i.

C_iO_i C_iO_i production is almost 3 times lower than in *C_H CzSi* sample and is also the lowest among other samples. The concentration of the complex remains stable below 300 ℃ and no remarkable bump is visible before the full dissociation of the complex.

C_iC_s The C_iC_s complex production is slightly higher than that of *C_H CzSi:Ge* sample and twice lower than that of *C_H CzSi* sample, but it shows a similar qualitative behavior.

5.2.4 Discussion and analysis of experimental data

It is important to note that the initial concentrations of oxygen and carbon are not the same in all the considered samples. Carbon and oxygen impurities serve as traps for the primary radiation defects (I and V respectively). Their concentrations are expected to affect the introduction rates of the vacancy- and the interstitial-related secondary radiation induced defects. Hence the direct comparison of the samples is not possible. In addition, it has been reported that carbon concentration has a strong effect in Ge-doped samples [77]. This effect is also observed in the two present Ge containing samples. Nevertheless, in the present analysis, we aimed to derive conclusions from the analysis of the relative concentration of the various defect clusters made of carbon and vacancies/interstitials.

We start our analysis with the two reference samples, which contain low and high concentration of C, namely *C_L CzSi* and *C_H CzSi*. When the oxygen concentration is larger than that of carbon, as in these two samples, the concentration of the C_iO_i defects is dominating over other interstitials containing pairs. For the *C_L CzSi* sample, it corresponds to more than 80 % of the detected interstitial-related defects. By inspection of the results in Table 5.2 and particularly the ratio of vacancy related defects to interstitial related defects ($R_{V/I}$), one gets a value of 1.5, indicating that one third of interstitials is not detected. These interstitials either were annihilated, for example on the sample edges, or they have formed undetected complexes.

Regarding now the sample containing high carbon content *C_H CzSi* (see Table 5.2), the $R_{V/I}$ ratio shows a value of 0.84, indicating that interstitials were efficiently trapped during the irradiation course, while at least one fifth of vacancies is missing.

The elevated carbon content leads to an efficient interstitials containing complexes formation.

From the above described carbon containing samples it follows that C presence in the sample leads to a higher production of C_iO_i, C_iC_s, and C_iO_iI complexes. Carbon atoms effectively captures interstitials what results in the following prompt interaction of C_i with remaining C and O_I.

Contrary to carbon, which covalent radius $r_c(C) = 0.77$Å is smaller than that of silicon $r_c(Si) = 1.11$Å, germanium and lead have larger covalent radii, which are equal to 1.22Å and 1.47Å, respectively. In the case of the Ge and Pb-doped samples the concentration of the C_iO_i defects is substantially lower than that of the VO_i defects (see Table 5.2) suggesting that isovalent dopants play a key role in the reduction of the detected defect clusters. Interestingly, the $R_{V/I}$ is balanced in *C_L CzSi:Ge* and is over-balanced for both *C_H CzSi:Ge* and *C_H CzSi:Pb*. This result indicates the same kind of behavior for two latter samples, although dopant interactions with vacancies and interstitials are expected to be different for the two dopants.

Carbon associated defects: carbon balance before and after irradiation. To further investigate the possible clustering within our co-doped samples we analyze the carbon distribution before and after irradiation. The data are reported in Table 5.3. In the C-doped and the C-Ge co-doped samples, the situation is rather clear as about 85-95% of the initial substitutional carbon is dispatched between substitutional carbon and the three carbon interstitial related clusters. But for the C-Pb co-doped sample only about 20 % of the initial substitutional carbon is detected after irradiation. This lead us to a conclusion, that most of the carbon related complexes were detected in C and C-Ge co-doped samples. However in the Pb-doped sample, some carbon-containing complexes, which were not detected by FTIR, can be present in the sample. These complexes could be vacancy-/interstitial-related and purely substitutional.

	$[C_s]_{bi}$	$[C_iO_i]$	$[C_iC_s]$	$[C_iO_iI]$	$[C_s]_{ai}$	$\sum[C_{ai}]$	$[C_s]_{bi} - \sum[C_{ai}]$
C_L CzSi	5.0	3.0	0.56	0.23	1.0	4.79	0.21 (4.2%)
C_L CzSi:Ge	4.4	2.53	0.80	0.49	0.5	4.32	0.08 (1.8%)
C_H CzSi	22.0	5.72	1.01	0.46	13.2	20.39	1.62 (7.3%)
C_H CzSi:Ge	10.0	2.86	0.34	0.30	1.0	8.40	1.60 (16.0%)
C_H CzSi:Pb	19.0	1.87	0.45	0.30	0.5	3.12	15.88 (83.6%)

Table 5.3: Concentrations of carbon-related defects before and after irradiation given in $10^{16} cm^{-3}$

.

Since some vacancy-, interstitial-, and carbon-related defects were not detected by FTIR, we decide to perform DFT calculation to identify possible missing complexes.

5.3 Theoretical investigation of secondary radiation induced defects in carbon doped and isovalently co-doped silicon

Our goal is to perform a systematic theoretical investigation of possible associations of point defects and defect complexes in irradiated silicon. In a first approximation, we aimed to study mainly thermodynamic properties without considering defects formation and migration kinetics.

Point defects in electron-irradiated Cz-silicon can be organized depending on their origin and type in five groups:

1. natural impurities (C and O_i related impurities introduced to the crystal during the growth process),
2. primary radiation defects (Frenkel pair: V and I),
3. secondary radiation defects (various combinations of previous items),
4. isovalent dopants: C, Ge, Sn, Pb (we consider tin (Sn) doping for the sake of completeness, although we have not presented corresponding experimental data),
5. complexes containing isovalent dopants.

All impurities and complexes, considered in this thesis are summarized in Table 5.4 and placed in one of the groups described above.

Point defects of the first four columns of the Table are widely studied in literature using experimental [24, 67, 68, 92] and theoretical [53, 44, 27, 9, 28, 22, 87, 20, 21] approaches, whereas defects of the last column received less attention so far. Nevertheless, for consistency reasons, we performed DFT calculations for all the listed defects in Table 5.4.

For the calculations, we used a 216 Si supercell and Γ-point sampling. All defect structures were optimized to their minima and their corresponding energy characteristics, such as chemical potential (calculated using Eq. (3.21) and (3.22)) and binding energies (calculated using Eq. (3.23)), are given [5]. The results for the simple defects (columns I, II, and IV of Table 5.4), such as substitutional isovalent atoms, O_i, V and I are represented in Table 5.5, along with the schemes of optimized geometry configurations. These defects are well known and have been widely studied in literature [20, 21, 27], that is why we will not consider them in more detail. However these configurations will serve as references for further calculations of binding energies of more complex point defects.

5. The total energies of all considered structures are listed in Appendix A.

Naturally present isolated impurities	Primary radiation defects	Secondary radiation defects and complexes	Isovalent dopants (D)	Associations of D with radiation defects
O_i	V	VO_i	C	DV
O_{i2}	(V_n)	VO_{i2}	Ge	DVO_i
			Sn	
C	I	V_2O_i	Pb	DC
		V_2O_{i2}		
				DI
		C_iO_i		D_i
		C_iO_{i2}		
		C_iO_iI		
		C_sO_i		
		C_sO_{i2}		
		C_i		
		C_iC_s		
		C_iC_i		

Table 5.4: Possible defect complexes are grouped by their origin. Notation D stands for one of the four isovalent dopants.

	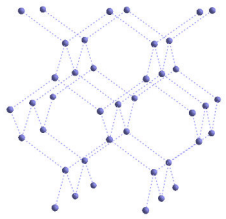	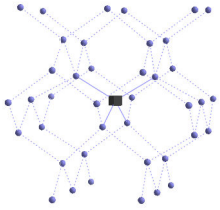	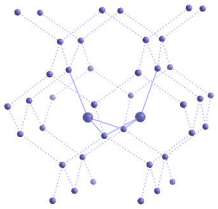
Structure	Si	V	I
μ $[eV]$	-107.162	3.472	-103.978

	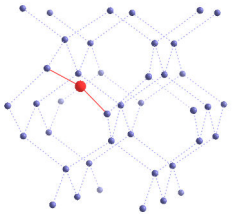	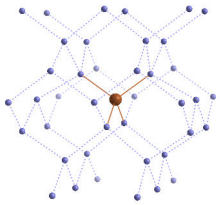	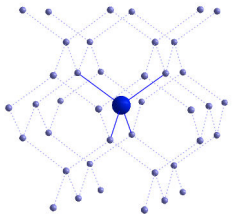
Structure	O_i	C	Ge
μ $[eV]$	-437.02766	-153.598	-106.940

	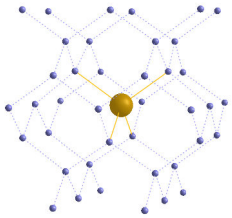	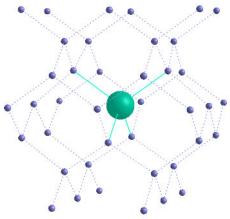
Structure	Sn	Pb
μ $[eV]$	-95.892	-94.482

Table 5.5: Geometries and chemical potentials of simple point defects in crystalline silicon. Note that chemical potential for substitutional, vacancy, and interstitial atoms were calculated in a different manner, as described in Section 3.2.2

5.3.1 Carbon containing silicon

Table 5.6 represents the obtained binding energies E_b for direct reactions leading to the secondary irradiation induced complexes formation in C and O_i containing Si (III column of Table 5.4). We adopted the structures of these complexes from reports on previously performed *ab inito* investigations [53, 44, 27, 9, 28, 22, 87, 20, 21]. A particular case of C_iC_s complex was studied in more detail. The problematics of this complex have been introduced in Chapter 2; and a careful consideration of this complex properties will be presented in Chapter 6. Here, we will give the four geometries of this complex with their corresponding E_b.

Once we obtained the optimized geometry of a point defect complex and extracted

the total energy of this structure, we have to investigate, how this complex can form and dissociate. In other words, we are interested in the possible defects interactions that could lead to the complex formation and possible dissociation schemes. Note that in general case, the former and the latter processes are non-unique and can be described by different reactions.

Here, we aimed to derive all possible reactions resulting in each considered complex. To achieve this goal, we always considered all possible combinations of two ingredients. However, not all of them are favorable, only those with $E_b > 0$ are likely to occur. The reverse reactions describe the possible dissociations of a complex. The latter is possible, if the corresponding binding energy is negative.

Another limitation is the mobility of the initial ingredients at considered temperature range. During the electron-irradiation flow, the production of secondary irradiation induced point defects happens at 80 ℃. At this low temperature, the thermodynamic equilibrium can be achieved in years timescale. Therefore, the possible direct and inverse reactions are those including fast diffusing species, which are mobile at that temperature. These reactions are typed in bold in Table 5.6 for both associations and dissociations.

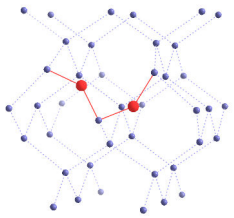
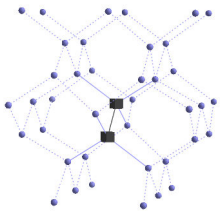
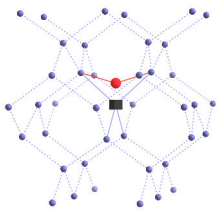

Structure	O_{i2}	V_2	VO_i
E_b $[eV]$	$O_i + O_i$ 0.138	**$V + V$ 1.832**	**$V + O_i$ 1.500**

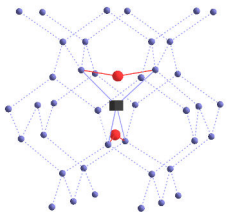
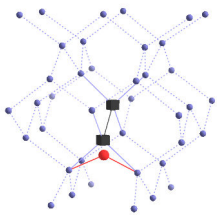
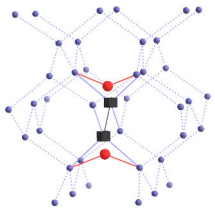

Structure	VO_{i2}	V_2O_i	V_2O_{i2}
E_b $[eV]$	$VO_i + O_i$ 1.204 **$V + O_{i2}$ 2.567**	$V_2 + O_i$ 1.104 **$V + VO_i$ 1.435**	$V_2 + O_{i2}$ 2.284 $VO_i + VO_i$ 1.253 **$V + VO_{i2}$ 1.549** $V_2O_i + O_i$ 1.318

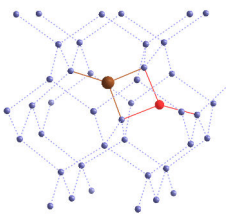
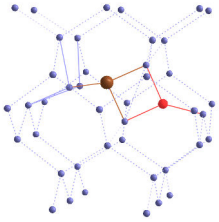
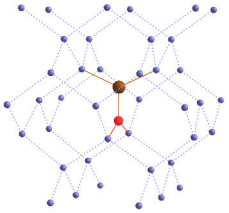

Structure	C_iO_i		C_iO_iI		C_sO_i	
					$C + O_i$	-2.077
E_b $[eV]$	$\mathbf{C_i + O_i}$	**1.293**	$\mathbf{C_iO_i + I}$	**1.090**	$\mathbf{C_iO_i + V}$	**1.803**
					$\mathbf{C_i + VO_i}$	**1.596**

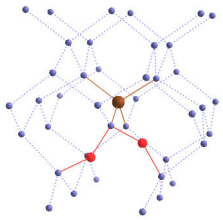
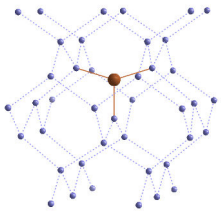
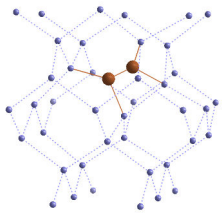

Structure	C_sO_{i2}		C_i		C_iC_i	
	$C + O_{i2}$	0.731			$\mathbf{C_i + C_i}$	**2.280**
E_b $[eV]$	$\mathbf{C_i + VO_{i2}}$	**3.339**	$\mathbf{C + I}$	**1.45**	$\mathbf{I + C_sC_i(B)}$	**2.798**
	$C_iO_i + VO_i$	3.250			$\mathbf{I + C_sC_i(C)}$	**2.450**

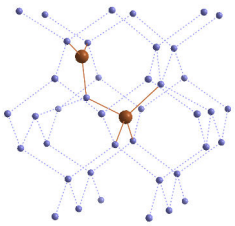
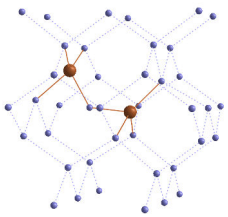
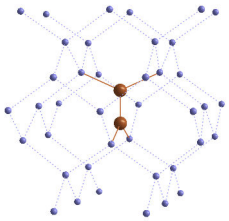

Structure	C_sC_i A-form		C_sC_i B-form		C_sC_i C-form	
E_b $[eV]$	$\mathbf{C_i + C}$	**0.864**	$\mathbf{C_i + C}$	**0.931**	$\mathbf{C_i + C}$	**1.114**
	$\mathbf{C_iC_i + V}$	**3.758**	$\mathbf{C_iC_i + V}$	**3.825**	$\mathbf{C_iC_i + V}$	**4.008**
E_b^{SP} $[eV]$					$\mathbf{C_i + C}$	**1.282**
					$\mathbf{C_iC_i + V}$	**4.176**

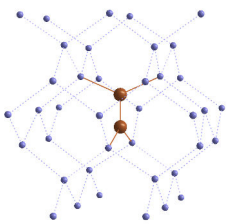

Structure	C_sC_i D-form

E_b $[eV]$	C_i + C	0.884
	C_iC_i + V	3.778

Table 5.6: Geometry schemes, total energies and binding energies for various possible defect complexes in carbon and oxygen containing Cz-Si. Reactions, by which a complex formation or dissociation proceed through the fast-diffusing species, are typed in bold. The last two complexes, namely C- and D-forms of C_iC_s, have the similar, but not equivalent structures. For more details, concerning the C_iC_s pair, the reader is referred to Chapter 6.

Although, all reactions in bold are possible at that temperature range, production of each defect complex will be limited by the concentrations of the ingredients in unbound state. That is why, although we have a source of vacancies, there are very few of them in a free state, as they immediately bound to oxygen, and there is a low probability to two vacancies to meet. This fact is related with a significant concentration of oxygen in Cz-Si: an interstitial oxygen atom immediately captures a vacancy causing a negligible probability of two vacancies to meet. The same happens with C_i fast diffusing species. A lot of them appear during the irradiation flow, however their chance to meet each other is low, because they are trapped by interstitial oxygen and by substitutional carbon atoms.

The rest of the reactions in Table 5.6 can happen at elevated temperatures and are very important to consider for the temperature evolution of point defect complexes. Thus, the computation of each complex concentration and its temperature evolution is a stand-alone task, requiring consideration of the kinetic aspect of complexes formation and will be considered in Section 5.3.3 by using Kinetic Mass Action Law. While in this section, we will focus on the possible reactions search.

To summarize, the results presented in the table show that VO_i, C_iO_i, C_iO_iI, C_sO_i, and C_iC_s complexes should be present in the electron-irradiated Cz-Si. These results agree well with experiments, that proves the validity of the approximation used in our DFT calculations. However, *ab initio* approach cannot provide the relative concentrations of these defects. The other complexes formation at irradiation temperature is limited either by the absence of one of the ingredients or by very low possibility of their meeting. Now, we will consider the case of isovalently co-doped Cz-Si.

5.3.2 Isovalently co-doped silicon

Isovalent dopants in silicon are electrically inactive as they belong to the same column of the periodic table and thus have the same valency. However, they introduce

internal strain into the crystal. The impact of isovalent point defect presence on the neighboring bondlengths is represented by Figure 5.4. It is shown, that perturbation of the bondlengths of the crystal is localized. It is less than 2% starting from the second nearest bond and decreases with distance. This lead us to a conclusion, that isovalent point defect presence cannot affect much the behavior of approaching species; and that the trapping radius of the isovalent dopant can be determined by the two first neighboring bonds.

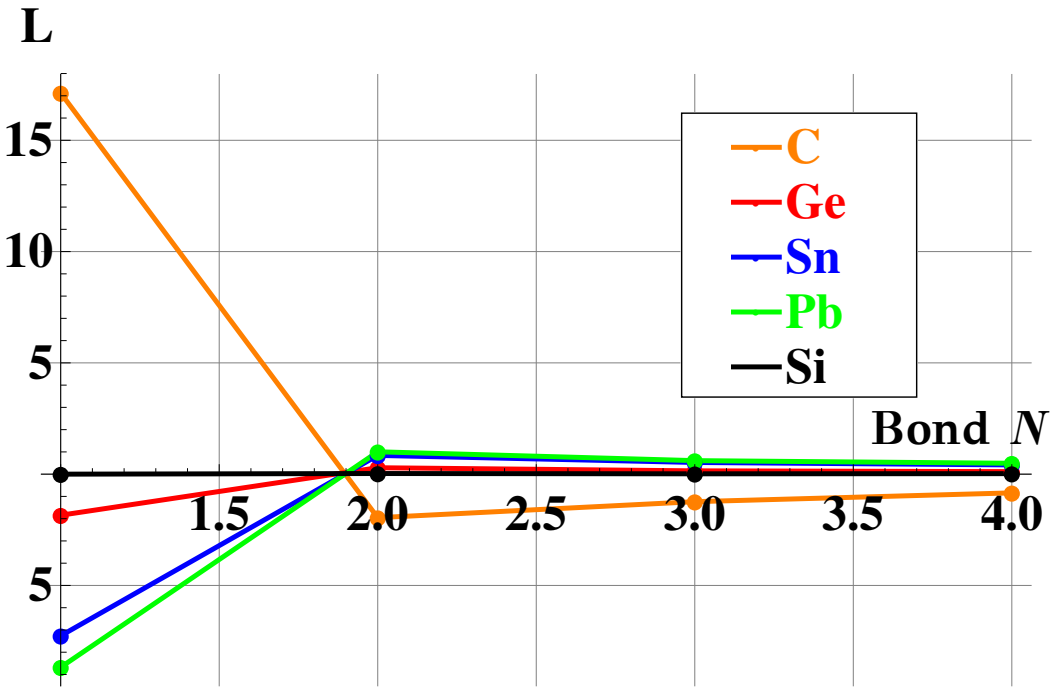

Figure 5.4: The decay of the internal strain around the substitutional isovalent atoms in crystalline silicon. Bond numbers counts along (100) direction.

Nevertheless, C is the only dopant, which introduces a tensile strain into the lattice, while all oversized dopants, namely Ge, Sn, and Pb, introduce compressive strains. Interaction with irradiation induced defects can compensate this strain, thus leading to a positive effect on reduction or a full suppression of some of detrimental complexes.

There can be several approaches to investigate which complexes can be formed in isovalently (co-)doped silicon. The first approach is an exhaustive search, considering all possible combinations of point defects. Although this is a straightforward way, it has disadvantages: the number of considered complexes can be huge leading to very resource demanding calculations. The second approach, is to limit the search by some kind of rational consideration. In our case, we start our investigation assuming only fast diffusing species, such as V, I, and C_i. Following this logic, as a result of

interaction of isovalent dopant D with vacancy, we get DV complex, while interaction of DV complex with C_i fast diffusing species gives CD complex.

Table 5.7 summarizes obtained results for the complexes containing isovalent dopants: C, Ge, Sn, and Pb. Along with considered defect complexes, the table lists the possible reactions, which were obtained as in the previous section (following the logic from the previous section).

Vacancy related defects To begin with, we consider vacancy-related defects in Ge, Sn, and Pb doped samples. These elements are isovalent impurities in Si with a covalent radius larger than that of Si. Therefore, they introduce local compressive strains in the Si lattice, which can be relieved by the association with vacancies. GeV, SnV, and PbV pairs have positive binding energies equal to 0.27 eV, 1.17 eV, and 1.38 eV, respectively. These values are in agreement with previous theoretical investigations [107] (+ Refs. therein).

For Ge-doped Si the formation of the GeV pair has been previously reported [15] in low temperature irradiated Si. GeV is stable up to about 200 K and then dissociates effectively liberating the trapped V. Although it is expected theoretically, the formation of SnV and PbV pairs has not been directly observed experimentally yet, and only indirect indications of PbV and SnV pairs have been reported[107]. The corresponding binding energies of the VO_i and GeV pairs are found to be 1.50 eV and 0.27 eV respectively. These values are indicating that when O_i and Ge compete for a V, the formation of the VO_i pair will be prevalent from a thermodynamic perspective. The $GeVO_i$ complex can be also effectively formed as a result of VO_i and Ge interaction. The process will be limited by VO_i mobility and therefore will occur at elevated temperature range. The thermal energy should be high enough for the VO_i migration and at the meantime the complex should be stable at such temperatures. This might be one of the reasons, why VO_i band in Ge containing samples starts to disappear at slightly lower temperatures than that of only carbon containing samples ($\sim$ 275 ℃ *vs* $\sim$ 300 ℃). The same effect can be observed for the Sn and Pb dopants, as corresponding $SnVO_i$ and $PbVO_i$ complexes are also stable.

Compare to germanium, tin and lead dopants associate with vacancies in more favorable manner due to their larger covalent radius, leading to a larger reduction of VO_i pairs. This implies that Sn and Pb will compete more efficiently for the available V than Ge and therefore, they have a more significant impact on the reduction of the concentration of VO_i pairs during the irradiation course. The $PbVO_i$ and $SnVO_i$ complexes formations are also favorable but it is constrained by VO_i pair diffusion-dissociation balance, as was explained just above.

Generic notation	Defect	formation	E_b $[eV]$
DV	CV	C + V	0.328
	GeV	Ge + V	0.270
	SnV	Sn + V	1.166
	PbV	Pb + V	1.376
DVO_i	CVO_i	C + V +O_i	1.884
		CV + O_i	1.556
		C + VO_i	0.384
	$GeVO_i$	Ge + V + O_i	1.748
		GeV + O_i	1.480
		Ge + VO_i	0.247
	$SnVO_i$	Sn + V + O_i	2.296
		SnV + O_i	1.130
		Sn + VO_i	0.796
	$PbVO_i$	Pb + V + O_i	2.525
		PbV + O_i	1.149
		Pb + VO_i	1.024
DC	CC	C + C	-1.438
		CV + C_i	3.409
	GeC	Ge + C	-0.065
		GeV + C_i	4.840
	SnC	Sn + C	0.312
		SnV + C_i	4.321
	PbC	Pb + C	0.333
		PbV + C_i	4.131
DI	CI site 1	I + C	0.875
	GeI site 1	I + Ge	-0.002
	SnI site 1	I + Sn	-0.152
	PbI site 1	I + Pb	0.008
D_i	C_i	I + C	1.448
	Ge_i	I + Ge	0.095
	Sn_i	I + Sn	-0.138
	Pb_i	I + Pb	0.049
C_iD	C_iC_s site 1	C_i + C	-0.275
	C_iC_s site 2 conf A	C_i + C	0.877
	C_iC_s site 2 conf B	C_i + C	0.947
	C_iC_s split conf C-SP	C_i + C	1.287
	C_iGe_s site 1	C_i + Ge	-0.440
	C_iGe_s site 2	C_i + Ge	-0.023
	C_iSn_s site 1	C_i + Sn	-0.491
	C_iSn_s site 2	C_i + Sn	-0.206
	C_iPb_s site 1	C_i + Pb	-0.598
	C_iPb_s site 2	C_i + Pb	-0.177

Table 5.7: Possible associations of defects in isovalently co-doped Cz-Si. Calculated total energies and binding energies are summarized. The binding energies of "DI site 2" (see Figure 5.5) complexes were found to be negative for Ge, Sn, and Pb case. Such configuration is less stable than "DI site 1" for all four dopants.

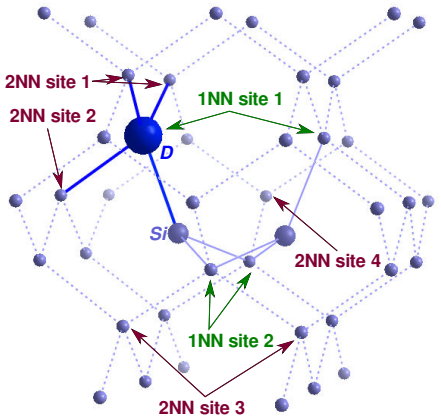

Figure 5.5: DI configuration scheme.

Interstitials related defects In the literature, interstitial-related defects in isovalently doped and co-doped samples are less studied and therefore less understood. To clarify this point, we considered the point defects made from interstitials and isovalent dopant atoms. Three types have been considered in the following: i) the carbon substitutional-dopant substitutional complex CD, ii) the dopant substitutional-silicon interstitial complex DI, which is the precursor of D_i point defect, and iii) the carbon interstitial-dopant substitutional complex C_iD_s.

As for the case of only carbon and oxygen containing complexes, we investigate possible point defect reactions by assuming fast diffusing species, such as I and C_i. Following this view point, the simple CD complex defect can be formed as a result of the reaction: $DV + C_i \rightarrow CD$. On one hand, the binding energy of the GeC pair formed from GeV and C_i is 4.84 eV, which means complex stability up to high temperatures. On the other hand, the $GeVO_i$ concentration is fully driven by the GeV concentration. In addition, a dissociation to substitutional Ge and C is favored from thermodynamic point of view. But this process requires either Ge or C migration, which is strongly unfavored from kinetic point of view. The same analysis can be applied for SnC and PbC complexes. They can be formed due to the interaction of fast diffusing C_i with SnV and PbV complexes, while their dissociations are kinetically constrained.

As far as CV complex is unfavored, we claim that CC pair is unlikely to form in isovalently doped silicon samples, as its binding energy is negative and as low as -1.44 eV.

Association of the substitutional dopant atom with a fast diffusing I is another possibility to form a complex. DI complex is a precursor for the D_i point defect. DI complexes geometry are ambiguous, as Si interstitial can approach the substitutional atom in several manner. Due to the symmetries of the configuration, all the possibilities are reducing to two inequivalent cases. On Figure 5.5, these two

configurations are represented with respect to I. "1NN - site 1" and "1NN - site 2" indicate the inequivalent first nearest neighbors of the Si split interstitial. Among the two configurations, the former case leads to lower energies for all dopants. More precisely, Table 5.7 lists these values. Only CI association is stable and it leads to a formation of C_i.

In addition, we considered four inequivalent configurations of DI complexes, when D and I were places as the second nearest neighbor relative to each other. All of them was found to be less stable than closer orientation.

The split interstitials (D_i) for all oversized isovalent dopants, namely Ge, Sn, and Pb, was found to be $\langle 110 \rangle$ oriented. Binding energies of these configurations are close to zero, which means that none of them can be stable at nonzero temperatures ($T > 0$ K). Only the binding energy of C_i oriented along $\langle 100 \rangle$ is positive and is equal to 1.45 eV.

Considering now possible association of fast-diffusing C_i with isovalent atoms in their substitutional positions, we get the complexes of C_iD_s type. Here, we have also different possibilities to form a complex. Accounting for symmetry, we get two irreducible possibilities, indicated as site 1 and site 2 in Figure 5.6. Nevertheless, the configurations was found to be unstable, indicating that isovalent dopant with radius bigger than that of silicon, cannot be an efficient traps for carbon interstitials. On the other hand, carbon substitutional atom traps efficiently C_i atoms and lead to a gain in energy of at least 0.88 eV according to our calculations.

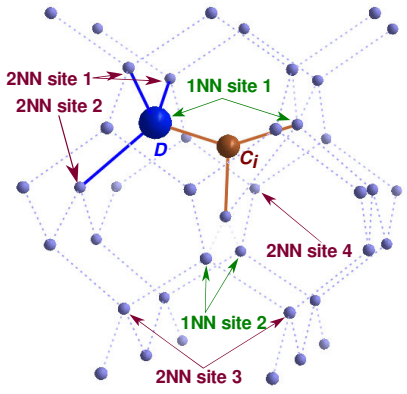

Figure 5.6: C_iD_s configuration scheme.

5.3.3 Missing complexes

Once we got all the trapping energies for carbon doped and isovalently co-doped Cz-silicon, we can come back to the analysis of experimental data, with respect to the obtained values. As we already considered kinetic aspect of complexes formation,

which proceeds through fast diffusing species, we can further focus only on purely thermodynamical aspects.

Complexes with negative binding energies cannot be formed at any temperature range, except particular cases, when formation and dissociation of a complex happen in different manner and dissociation is limited by kinetic aspects. For positive binding energies, the complex formation is controlled entirely by the pairing kinetics. Therefore, we will consider these complexes as favorable ones. However, the dissociation and hence a precise value of E_b, is essential. According to the Mass Action Law, at irradiation temperature of 80 ℃, defects, which binding energy is lower than ~ 0.4 eV, dissociate due to the thermal energy. This is the case for GeV and CV defect pairs, which binding energies are 0.27 eV and 0.33 eV, respectively. Consequently, these complexes may be considered as transient during the irradiation flow. Based on these precepts the following analysis of defect clustering has been performed.

From the values presented in Table 5.7, it is evident, that C tends to interact with I as well as with C_i. Regarding the effect of carbon doping on the VO_i production, high carbon contamination can affect VO_i production rate through the capturing of self-interstitials and preserving them from annihilation with vacancies during the irradiation flow. This is also supported by the experiment as the detected VO_i concentration in a low carbon doped sample is slightly reduced compare to the reference sample with high carbon concentration (see Table 5.2). Although, CVO_i and $GeVO_i$ complexes are stable, their formation is blocked by the CV and GeV complexes concentration, which should be negligible at irradiation temperature.

Pb and Sn dopants bind with vacancies, thus forming PbV and SnV complexes. Moreover, further associations with fast diffusing C_i can lead to PbC and SnC associations. Despite their low binding energies, their dissociation is unfavorable, as diffusion of substitutional atoms would require the formation of a Frenkel pair. This process is rather beneficial due o the following reasons. Firstly, PbV and SnV formation reduces the VO pairs formation in Cz-silicon irradiated with electrons. Secondly, it leads to an annihilation of vacancy and interstitial atom by forming an electrically inactive defect complex. As in the case of C and Ge, formation of PbVO and SnVO complexes is blocked by O_i and VO_i diffusion. In substitutional position, Pb and Sn do not associate with interstitials neither with I nor C_i.

Concerning the missing carbon in Pb-C co-doped sample, we can infer that it can be distributed between CPb and not detected forms of C_iC_s pairs. Instead, only one of the C_iC_s pair was considered in experiments, while four of them are possible according to DFT results. At the same time, the CPb complex has not been identified experimentally, so far, however its presence is favorable. In addition, it is possible, that CC complex can be formed during the irradiation flow from the transient CV complex and fast diffusing C_i.

Generally speaking, associations of isovalent dopants with interstitials and vacancies should be related with their covalent radius. Indeed, DFT-derived binding energies supports that idea. The relative trapping forces of isovalent dopants are summarized in Table 5.8. Indeed, for the dopant-V pairs there is a stronger binding energy for PbV and SnV, while CV and GeV pairs are less stable. Moreover, the DFT calculations have illustrated that the situation is opposite in the case of interstitial related defects as the binding energy of the interstitial with a Ge atom is stronger than that with a Pb atom.

	C	Ge	Sn	Pb	O_i
V	0.33	0.27	1.17	1.38	1.50
I	1.45	0.10	−0.14	0.05	—

Table 5.8: Relative trapping forces of I and V by isovalent dopants (C, Ge, Sn and Pb) and O_i.

Notably, the balance of vacancy/interstitial related defects is a very informative tools to study defect complexes formation in irradiated material. Moreover, the balance of the impurity species before and after irradiation is an important indicator of the point defect reactions occurred in the sample. Such kind of balance analysis together with calculations from first principles allows investigation of the complex behavior of defects and impurities as well as their fundamental properties in the material.

Nevertheless, pure thermodynamic analysis sometimes cannot explain some kinetics related features. This can be illustrated on the example of the C_sO_{i2} defect complex formation, during the annealing of the sample. As far as C_iO_i and VO_i defects anneal out at about the same temperature around 300 ℃, both of them can lead to a C_sO_{2i} formation. Part of the migrating VO pairs can encounter C_iO_i defects leading to the following reaction:

$$C_iO_i + VO_i \rightarrow C_sO_{i2}. \tag{5.1}$$

Also it is possible that upon C_iO_i dissociation, some of the liberated interstitial carbon atoms interact with VO_{i2} centers to form C_sO_{i2} defects according to the reaction:

$$C_i + VO_{i2} \rightarrow C_sO_{i2}. \tag{5.2}$$

The both just mentioned reactions are favorable from thermodynamic point of view with close gain in energy of 3.25 eV and 3.34 eV. And both of them occur at the same temperature range. Along with these reactions, there is a plenty of others, like VO_{i2} formation, interaction of C_i with vacancy related defects, and many others. Their careful consideration requires a study, accounting for the kinetics aspect of

processes, occurring in competition with each other.

Kinetic Mass Action Law [6]

At the thermodynamic equilibrium, the stability of a complex depends on its binding energy, temperature and concentration of its components. Meanwhile, at low temperatures, the thermodynamic equilibrium is long to achieve. Therefore diffusion kinetics of the complexes themselves and their components can limit possible rearrangements. Such cases require careful consideration of the kinetic aspects of point defects diffusion and complexes formation, and requires a multiscale approach. In other words, atomistic and continuous scale simulations can be combined. The idea of such synthesis is to use the results of precise atomistic simulations, such as DFT, as an input to perform larger scale methods, such as Kinetic Monte Carlo, or continuous methods. This allows keeping the atomistic precision and, at the meantime, to deal with realistic scales while reasonable computational effort. Here the results of DFT and Kinetic Mass Action Law (KMAL) based model will be presented. The latter was applied and developed by Gilles Brenet, in order to analyze the DFT results presented in the previous sections.

In the KMAL based model, we deal with a system of N reactions described by

$$\sum_i \alpha_{ri} A_i \rightleftarrows \sum_j \gamma_{rj} C_j, r \in 1, ..., N. \tag{5.3}$$

Here, a forward reaction corresponds to the creation of a complex C_j, while the backward reaction corresponds to its dissociation. The reaction rates $k_{r\pm}$, for reaction r, are described by

$$\frac{\delta[A_l]_r}{\delta t} = k_{r+} \prod_i [A_i]^{\alpha_{ri}} - k_{r-} \prod_j [C_j]^{\gamma_{rj}}. \tag{5.4}$$

Here, $[A_i]$ and $[C_i]$ are the concentrations of the reactant and the product respectively; α_{ri} is the stoichiometric coefficient of reactant i for the forward reaction r, and γ are the coefficient for products. Particles were considered moving on a diamond type lattice. The reaction rates $k_{r\pm}$ are built on transition state theory:

$$\begin{aligned} k_{r+} &= p_0 \cdot s_i \cdot \nu_0 exp[-\beta E_m^r] = \frac{p_0 \cdot s_i}{<t_{move}>} \\ k_{r-} &= \nu_0 exp[-\beta(E_b^r) + E_m^r] = \frac{1}{<t_{diss.}>}, \end{aligned} \tag{5.5}$$

where $\nu_0 = 10^{-13}$ s^{-1} is the event frequency, E_m^r is the migration energy of the diffusing species and E_b^r is the binding energy of the complex. Factor s_i reproduces the defect attraction area and is equal to a number of "active" sites around, which

6. Thermal evolution curves have been obtained by Gilles Brenet, address the future paper [7] for further details on methodology and on calculation details.

means that once the first point defect reaches the active area of the second one, the interaction between them happens and a complex forms. Otherwise, they simply do not feel each other. Therefore, the probability to form a complex will increase with the increasing of the factor s_i. And finally, p_0 is an approximate probability multiplier, which is set to avoid for previously discovered sites ($p_0 = 3/4$ for silicon lattice).

The KMAL simulations of various point defect associations in crystalline silicon require two input parameters, namely migration E_m and binding E_b energies. Such simulations have been performed for the carbon and oxygen containing silicon samples, which were irradiated by electrons at 80 ℃. The required binding energies were taken from the DFT calculations, described in the previous sections. The energy landscape was completed by the experimental and theoretical migration energies of some diffusing species, namely V, I, VO_i, and VO_{i2} [137, 111, 20, 44]. A simulation of the irradiation process was followed by an isochronal annealing of 20 minutes up to 550 ℃ with a 10 ℃ step. To mimic the electron irradiation process, a constant term of Frenkel pairs formation has been added. The point defect interactions were considered through the reactions listed in Table 5.9.

Reaction	E_b	Migrating species	E_m (association)	$E_b + E_m$ (dissociation)	s_i
$I + C_s \leftrightarrow C_i$	1.45	I	0.40	1.85	4
$2C_i \leftrightarrow C_{i2}$	2.28	C_i	0.58	2.86	4
$C_i + C_s \leftrightarrow C_iC_s$	1.28	C_i	0.58	1.86	4
$C_i + O_i \leftrightarrow C_iO_i$	1.29	C_i	0.58	1.87	6
$I + C_iO_i \leftrightarrow C_iO_iI$	1.09	I	0.40	1.49	1
$C_iI + O_i \leftarrow C_iO_iI$		C_iI		1.49	
$2O_i \leftrightarrow O_{i2}$	0.14	O_i	2.38	2.52	6
$V + O \leftrightarrow VO$	1.5	V	0.45	1.95	6
$VO + O_i \leftrightarrow VO_2$	1.20	VO_i	1.47	2.67	6
$VO + C_iO_i \leftrightarrow C_sO_{i2}$	2.80	VO_i	1.47	4.27	6
$VO_2 + C_i \leftrightarrow C_sO_{i2}$	2.89	C_i	0.58	3.47	12
$C_s + O_{i2} \leftrightarrow C_sO_{i2}$	0.73	O_{i2}	1.59	2.32	4
$VO_2 + O_i \rightarrow VO_3$		VO_{i2}	1.98		12
$C_i + I \leftrightarrow C_iI$	1.24	I	0.40	1.64	4
$C_i + VO \rightarrow C_sO_i$		C_i	0.58		12

Table 5.9: This table presents the different equations and the energy associated in eV.

To consider correctly the redistribution of point defects during the annealing steps, it is important to account for trapping properties of each defect and for sinks. The trapping properties can be simply estimated as a number of nearest neighbors of the trap. This parameter is specified by the s_i value in Table 5.9 for all considered

species. The sinks account for the vacancy and interstitial losses related to the crystal imperfections, as dislocations or precipitates. The losses of vacancies-related defects are especially pronounced during $VO_i \rightarrow VO_{i2}$ transformation, as only about 50 % of vacancies are eliminated in sample with low concentration of carbon. The concentration of the sinks is calibrated with respect to the results of experiments from reference [84]: $7.0 \cdot 10^{-6}\text{cm}^{-3}$ and $5.0 \cdot 10^{-8}\text{cm}^{-3}$ for V/VO_i and C_i/I, respectively.

This model is able to reproduce far from equilibrium states, for instance it shows the gradual formation of VO_i, C_iO_i, which is followed by appearance of C_iO_iI complex. Moreover, the model also simulates the metastable states of the system during the isochronal annealing procedure as illustrated in Figure 5.7 *(b)*. The results of simulations perfectly agree with experiments that proves that the applied techniques fully describes the physical processes occurring in carbon-oxygen containing irradiated silicon. Therefore, such a multiscale simulation technique is able to predict the possible defect associations as well as the underlying chains of reactions.

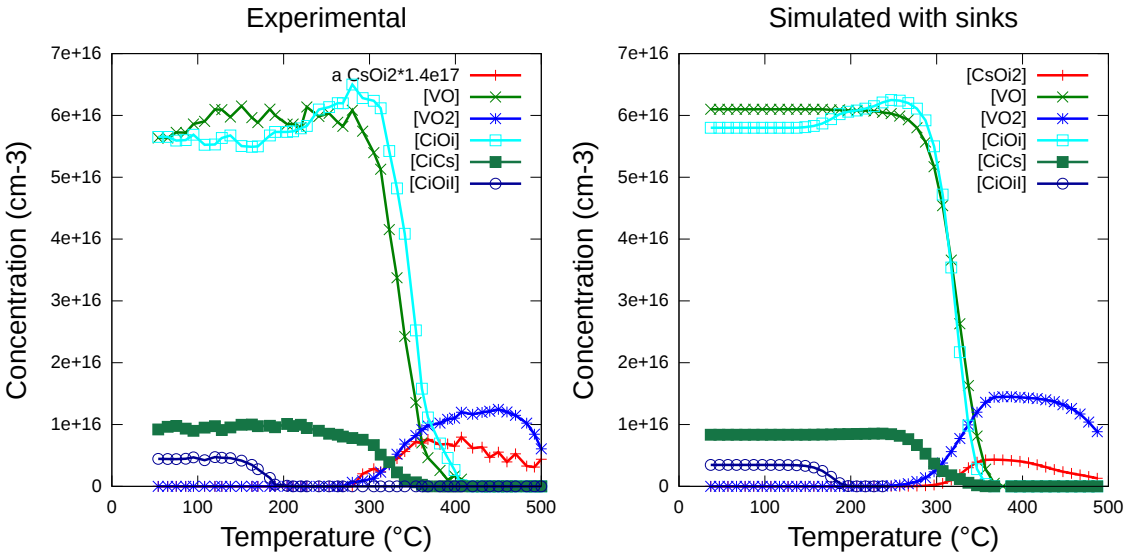

Figure 5.7: The population of several species for different temperatures during 20 min annealing: (a) The experimental results from [84], C_iC_s concentration has been multiplied by 30 to be visible. The absorption coefficient corresponding to C_sO_{i2} (1048 cm^{-1}) has been multiplied by $1.6 \cdot 10^{17}$ to be visible. (b) The results of KMAL simulations taking into account losses of V/VO_i and C_i/I species.

As it can be deduced from Figure 5.7, the kinetic model reproduces the main experimental features:

1. At 250-300 °C temperature range, a dip in the C_iC_s curve and a bump in the C_iO_i curve are related to each other. As follows from our *ab initio* calculations, fast diffusing C_i transfers from a weaker trap (C_iC_s) to a stronger trap (C_iO_i).
2. At 200-250 °C temperature range, the C_iO_i concentration is gradually raising.

This phenomenon is related with the dissociation of C_iO_iI, and thus an increase in the C_iO_i formation is observed. However, we have to take into account another possible reaction $C_iO_iI \rightarrow C_iI + O_i$ to reproduce the slope of the C_iO_i curve.

3. The VO_i to VO_{i2} transition ratio is equal to 1/4. The reduction is assigned to the release of C_i species from the dissociation of C_iC_s and C_iO_i complexes. Released C_i species recombine with both VO_i and VO_{i2} complexes causing such a low VO_i to VO_{i2} transition ratio.

Another important outcome from this study, is that to reproduce the experimental dissociation temperature of C_iC_s complexes, the binding energy of its C-form is essential. Whereas the binding energies of A- and B-forms lead to the discrepancy with the experiments. It should be noted, that the dissociation temperature of C_iO_i pair are perfectly reproduced by simulations, proving the validity of the obtained binding energies. This observation instigated us to further study the properties of the configurations of C_iC_s defect pair, namely its optical properties. It is widely accepted, that B-form is the most stable configuration of the complex, which is widely expected to be a light emitting defect. However, a number of *ab initio* investigations shows that the C-form is energetically the most favorable, as in our case. We will particularly address this issue in Chapter 6.

These are the main outcomes of the KMAL application to carbon-oxygen containing silicon. This model is very powerful and promising tool to explore complex defect interactions in Cz-Si, which will be soon applied for the cases of isovalently co-doped silicon.

5.4 Summary and conclusions

In this chapter we investigated the impact of electron irradiation on the formation and temperature evolution of point defects in carbon-doped and isovalently co-doped crystalline silicon. We aimed to decipher the processes of defect interactions and complexes reorganizations during the irradiation flow and while heating up to about 500 ℃. We used the IR absorption spectroscopy as an experimental tool to detect various point defects. In addition, we studied the complexes formation and stability by using the DFT-KMAL simulations. The main outcomes from this work can be grouped with respect to three main aspects, namely to experimental evidences, theoretical investigations, and validity of the applied methodological approach.

Experimentally, we examined the formation of the VO_i, C_iO_i and C_iC_s pairs, as they are known to strongly impact the properties of the silicon based devices. It was established that these pairs formation is substantially reduced in the C-Pb co-doped

Si as compared to the C_L doped sample. Regarding the thermal evolution of the above pairs, their annealing temperature is clearly lower in the case of the Pb-doped Si compare to all other samples. Therefore, C-Pb co-doping can be used to improve the radiation hardness of Si. Moreover, the analysis of the vacancy-, interstitial-, and carbon-related defects, derived from the FTIR measurements, revealed that in C-Pb co-doped sample, a large amount of carbon related defects are not detected after the electron irradiation. In order to identify the missing pairs, DFT simulations have been addressed.

By using first principle simulations, we performed a systematic analysis of various point defect complexes, which may exist in electron irradiated isovalently co-doped silicon. We derived the configurations of point defect complexes and their corresponding binding energies. This knowledge allowed us to construct a set of possible formation reactions, which were further analyzed. Concerning carbon, our DFT calculations prove that it is the strongest trap for the interstitials resulting to an increase of the VO_i concentration with the increase of C concentration. In Ge doped samples, we showed that Ge cannot trap interstitials at considered temperature ranges. That contradicts with the proposed mechanism of interstitial release in such Ge-doped samples [78, 135]. Therefore, further investigations is required to understand the reduced VO formation phenomenon in Ge doped samples. And finally, we obtained that the capture of C_i by PbV is a highly likely process, leading to a CPb complex formation.

According to the theoretical and experimental results, the isovalent dopants impacts drastically the production of vacancy- and interstitial-related defect complexes. The isovalent dopants interaction with vacancies and interstitials depends on their covalent radius. It can be concluded that the smaller the covalent radius is, the higher is the binding energy with interstitials and, vice versa, vacancies bind stronger to larger radius dopants. Of special interest is the Ge doped case where we obtained the medium values for both I and V. Such a case would be very sensitive to the dopant concentrations as it was shown previously in Ref. [77]. Other elements show more straightforward tendencies.

Although DFT can give clues for the most of possible reactions that can happen during the irradiation flow, it cannot mimic the temperature evolution of the samples under consideration, as kinetic aspects become of extreme importance. However, kinetics can be treated by KMAL, which was successfully applied for the case of carbon-doped silicon. As a result, the temperature evolution of the main irradiation induced pairs was fully reproduced, that allowed to decipher all reaction chains occurring in such samples. The application of the method for the isovalently co-doped cases will be soon performed.

To conclude, we would like to point out, that such a combined experimental-

theoretical study provides a very successful technique to study such complicated phenomena as point defect interactions. It allows reaching the atomistic scale and gives the full chains of occurring defect reactions.

Chapter 6

Optical properties of the C-C defect in silicon

6.1 Introduction

C_iC_s pairs can be formed during a high energy irradiation, not only with electrons, but also with ions, protons, or gamma-rays. This complex is a result of the interaction of a fast diffusing C_i with an immobile substitutional C_s.

The early EPR study [17] suggests that the complex consists of a vacancy occupied by two carbon atoms in a positive charge state, lying in $\langle 110 \rangle$ plane with a C-C bond oriented along (111) direction. Later based on optical detection of magnetic resonance study of O'Donnell *et al* [98] an optical 0.97 eV peak, so-called G-centre, was found to be related to C_iC_s complex in it's neutral state (see Figure 6.1). O'Donnell et

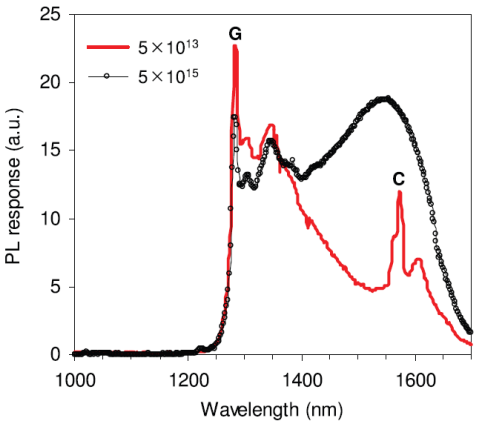

FIG. 1. Photoluminescence spectra, observed at 80 K, of pre-amorphised silicon samples A03 and A05 (2×10^{20} C cm^{-3} irradiated with 5×10^{13} and 5×10^{15} H$^+$ cm^{-2}, respectively). The positions of the G- and C-centres are also shown.

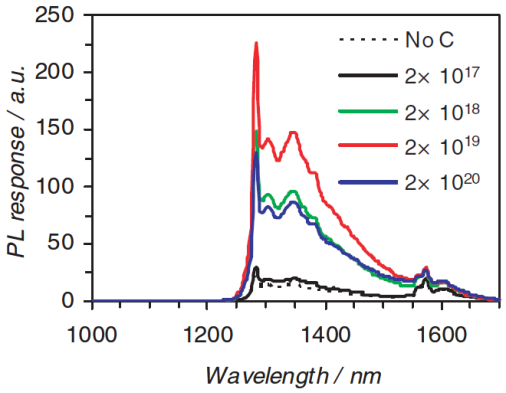

Figure 2. Photoluminescence spectra measured at 80 K of silicon samples implanted with different carbon doses and annealed at 1000 °C for 20 s, followed by proton irradiation at 5×10^{13} cm^{-2} at 2 MeV. The carbon concentrations (cm^{-3}) are indicated.

Figure 6.1: Experimental data from References [8] (left) and [7] (right). G-centre is a photoluminescent peak comping from the C_iC_s complex (B-form as it is widely accepted). C-centre is arising due to the interaction of carbon with residual oxygen atoms.

al. have proposed another model for C_iC_s complex where the substitutional carbon atoms are separated with an interstitial silicon atom. Two modification of the latter complex are possible: A-form, where the interstitial silicon is a three bonded, and B-form, where the Si is bonded only to two neighboring C_s atoms. This bistable C_iC_s

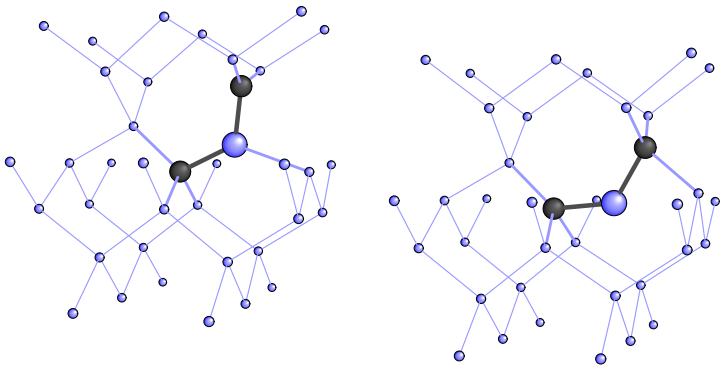

Figure 6.2: The A- and B-forms of C_iC_s complex are represented on the left and right sides of the figure, respectively.

complex (A- and B-forms) and it's charged states has been studies experimentally by Song *et al* [121](+ refs. therein). They have performed a wide analysis of the bistable C_iC_s complexes in p- and n-doped silicon by means of EPR, DLTS and PL techniques and provided a complete configurational-coordinate energy diagram. The A-form is found to be lower in energy for all the charged states, except the neutral, where the B-form is slightly lower in energy. Later the LVM of the bistable complex have been identified by means of IR spectroscopy [67]. Represented in Table 6.2, the obtained spectra of B-form and A-form are in fair agreement with values obtained by *ab initio* calculations [69, 22].

In 2002, Laiho *et al* [66] by means of EPR have detected a new low-symmetry configurations of a complex containing an interstitial silicon and two identical carbon atoms (see Chapter 2 for more details). These signals, named as Si-PT4 and Si-WL5, have not been identified so far, however their presence suggest several forms of C_iC_s complex. These forms appear during the cooling procedure and possess the varying magnetic properties. The exact geometry configurations of carbon-pair can be investigated by first principles studies.

A few theoretical attempts have been performed in the recent years. By means of DFT calculations, Liu *et al* [74] proposed a third configuration of C_iC_s complex, the C-form: two carbon atoms are situated in a vacancy and oriented in (100) direction. Although, the configuration was found to be at least 0.2 eV more stable than A and B for all charge states, there is no experimental observations proving this form presence so far.

Since then, most of the theoretical works investigate the three forms of C_iC_s complexes [87, 141, 35]. However, their results are not in agreement with each other.

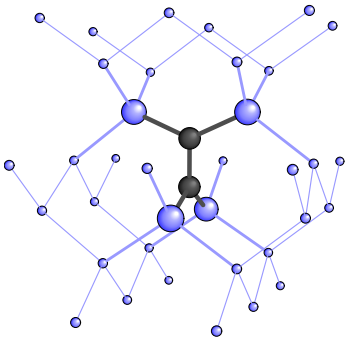

Figure 6.3: C-form: Two carbon atoms occupy one crystal site.

Reported by Mattoni *et al* [87] and Docaj *et al* [35], the binding of A-form is as strong as that of C-form, however both of the forms are less stable than B in neutral state. In these two studies, non spin polarized calculations have been performed. In contrary, Zirkelbach *et al* [141] have calculated the stability of dicarbon pairs by taking into account of the spin. In this case, the binding energy of the C complex was found to be the most stable among all.

In this chapter, we present our investigation of the structure, vibrational properties, and optical absorption spectra by means of first-principles calculations in order to determine and characterize the different forms of this C_iC_s complex. Moreover, we make an attempt to obtain the ground state (geometries, binding energies) and excited state properties (band gaps and optical absorption/emission spectra) of all the three forms. The latter property could allow us to assign which of three forms corresponds to the light-emitting G-centre.

6.2 Method

DFT as described in Chapter 3 is a method, which gives an access to the ground state properties of an atomistic system. This method covers the structural and vibrational characteristics, it successively reproduces the density of states of the occupied energy levels, and provides the correct total energies of a wide range of atomistic systems. However, this level of theory in principle fails to describe the excited state properties. Thus we need another level of approximation, in order to reproduce and predict light absorption and emission experiments. This becomes crucial if we want to calculate the optical spectra of the different forms of C_iC_s complex to compare them with the photoluminescence signal of the G-centre shown in Figure 6.1.

Fortunately, the green function's theory provides a proper method to calculate

single-particle excitation energies or quasiparticle energies. It was shown that the quasiparticle energies E_i can be obtained from the quasiparticle equation:

$$[-\frac{1}{2}\nabla V^H(\vec{r})]\Psi_i(\vec{r}) + \int d^3r'\Sigma(\vec{r},\vec{r'};E_i)\Psi_i(\vec{r'}) = E_i\Psi_i(\vec{r}) \tag{6.1}$$

Here Σ is the so-called self-energy operator, which is a non-local and energy dependent potential, accounting for the effects of exchange and correlations. In this extent, the DFT exchange-correlation functionals, such as LDA and GGA, are the single-particle approximations for Σ. The calculations of self-energy are very difficult even for the simplest systems, such as an electron gas, and thus need further approximations. The simplest one beyond the Hartree-Fock approximation is the GW approximation proposed by Hedin [54]. It is based on a set of coupled integro-differential Hedin equations [54, 55]:

$$\begin{gathered}
\Sigma(1,2) = i\int d(34)G(1,3^+)W(1,4)\Lambda(3,2,4) \\
G(1,2) = G_0(1,2) + \int d(34)G_0(1,3)\Sigma(3,4)G(4,2) \\
\Lambda(1,2,3) = \delta(1-2)\delta(2-3) + \int d(4567)\frac{\delta\Sigma(1,2)}{\delta G(4,5)}G(4,6)G(7,5)\lambda(6,7,3) \\
W(1,2) = v(1,2) + \int d(34)v(1,3)P(3,4)W(4,2).
\end{gathered} \tag{6.2}$$

Here, $G(1,2)$ states for the single particle non-local Green function, which is directly related to the excited states spectrum. Here, 1, 2, *etc* are the simplification for the space-time arguments $(\vec{r}_1,t_1)$, $(\vec{r}_2,t_2)$, *etc*. Starting from a given approximation for Σ, we can solve the set of equations self-consistently. The solution provides the energy spectrum.

The self-energy can be divided into a screened-exchange (SEX) and a Coulomb-hole (COH) terms, i.e. $\Sigma = \Sigma_{COH} + \Sigma_{SEX}$, which is thus called COHSEX formulation. While the former term is responsible for the electron-electron interactions, the COH term accounts for the interaction energy of the quasiparticle with the induced potential, arising due to the screening of the electrons around this quasiparticle [54, 55].

The GW approximation provides the correct quasiparticle energy spectra and correct band gap of a wide range of materials, including semiconductors. However, to obtain the correct emission-absorption spectra, the electron-hole interactions should be carefully taken into account. This is done in the Bethe-Salpeter approximation [115]. Here, we will not provide a more detailed explanation of the GW approximation and the Bethe-Salpeter equation. The reader is referred to the corresponding literature [19]. The excited state calculations were performed using the YAMBO plane wave code [86], is well suited for the calculations of the periodical systems.

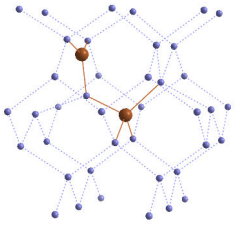

Figure 6.4: A-form

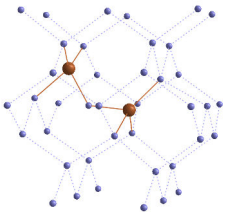

Figure 6.5: B-form

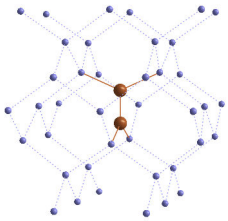

Figure 6.6: C-form

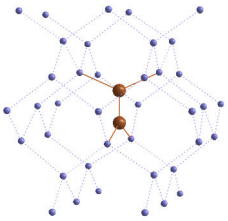

Figure 6.7: D-form

6.3 Results

Structure and binding energies of the forms of CiCs complex In Figures 6.4 - 6.7, the four obtained optimized configurations of C_iC_s complex are shown. In the A-form, carbon atoms occupy neighboring lattice sites, while the Si atom is an interstitial bonded to both carbon atoms and one silicon. The B-form is similar to A but the interstitial Si only bridges the two carbon atoms and are not bonded to another Si. The third configuration consists of two carbons in a vacancy aligned in a (100) crystallographic direction. D-form slightly differs from the previous configuration: all Si atoms bonded to two C atoms are slightly twisted around a C-C axis. D-form was obtained through non-spin-polarized geometry optimization. The initial configuration for this optimization was chosen to be slightly different from the C-form. Thus, we can conclude, that D-form is another local minima, which is similar to the C-form but almost 0.4 eV lower in energy.

The twisted shape of the D-form can result from the rotation of π-orbitals of two C atoms in order to form a π bond. In the C-form, the two corresponding π-orbitals are perpendicular to each other; each of them is occupied by one electron, making this complex paramagnetic.

All four forms of C_iC_s complex can be formed from very same ingredients, i.e. from mobile interstitial carbon and immobile substitutional carbon. Depending on the topology of the reaction, either A and B or C and D forms can be reached. In a neutral state, A will directly transform to B, as B is more stable. The A to B transformation barrier has been estimated to be as low as 0.1 eV [141]. Transformation from either A (or B) to C and backwards is less probable as the transformation barrier have been estimated to be as high as 2-3 eV [35]. Nevertheless, the kinetics of C_iC_s complex

formation and reorientation, *i.e.* various migration barriers, is out of the scope of present study, however certain aspects can be found in the paper of Zirkelbach *et al* [141].

The binding energies of the complex were calculated as $E_b^{C_iC_s} = -E_{tot}^{215SiC_iC_s} - E_{tot}^{216Si} + E_{tot}^{215SiC_s} + E_{tot}^{216SiC_i}$ and the obtained values are listed in Table 6.1. The C-form is found to be the most stable among all. This results are in contradiction with some recent theoretical studies [35, 87] however it is in agreement with findings of Zirkelbach *et al* [141] and Liu *et al* [74]. Accounting for the spin is crucial, as it increases the binding energy by about 0.17 eV compare to non-spin polarized calculations (0.2 eV in Ref.[141]). The D configuration has a binding energy of 0.88 eV, which is close to that of A-form and is lower than that of B-form.

complex	E_b, eV this study	E_b, eV other works
C_iC_s A-form	0.86	0.97
		0.93 [141]
		0.92 [35]
		w [87]
		x-0.35 [69]
		y-0.11 [22]
		z-0.2 [74]
C_iC_s B-form	0.93	0.95 [141]
		1.28 [35]
		w-0.4 [87]
		x [69]
		y [22]
		z-0.2 [74]
C_iC_s C-form (NSP)	1.11	0.90 [35]
		w-0.2 [87]
C_iC_s C-form (SP)	1.28	1.28 [141]
		z [74]
C_iC_s D-form (NSP)	0.88	

Table 6.1: Binding energies in eV for three configurations of C_iC_s. Some authors have not reported absolute binding energies of the three complexes, but stress out the energy difference between the studied forms. That is why here, the most stable configurations from References [87], [69], [22], and [74] are indicated with letters w, x, y, and z, respectively.

Generally speaking, all these forms can be present in a heavily carbon doped silicon, and their relative concentrations should depend on their binding energies. It should be also taken into account, that formation kinetics can impact significantly the balance between the three complexes concentrations. That is why, even if the A- and B-forms are indeed less stable that the C-form, they could be present in the sample and could be detected by various experimental techniques, such as IR and

EPR spectroscopy.

Coming back to the study of electron-irradiated silicon, that we have presented in Chapter 5, we remind that a band at 7819 cm^{-1} band was used to measure the C_iC_s complex concentration. This band is related with the electronic transition, corresponding to the formation of an electron-hole pair of G-centre [67]. Therefore, its calculations is out of the scope of present investigation. A dissociation temperature between $250 - 300$ ℃ was detected for this band. At the same time, the kinetic mass action law simulations clearly shows, that this dissociation temperature corresponds to the binding energy of the C-form, being as high as 1.28 eV. Moreover, considering the C-form by kinetic mass action law simulations reproduce the experimentally observed temperature evolution of of C_iC_s and C_iO_i pairs. After the decay of C_iC_s pairs, the liberation of the mobile C_i species cause the bump in C_iO_i temperature evolution curve as observed in the experiments.

The just described observation is a strong evidence for the presence of the C-form in irradiated silicon, but more detailed analysis of other properties should be performed in order to finally assign the observed properties of dicarbon pair to any of its form. While the situation is rather clear with LVM fingerprints, which is hard to misinterpret, more attention should be payed to the formation kinetics and optical properties of the forms of carbon-carbon pair. Hereafter, we will consider only three forms of C_iC_s pair, namely A-, B-, and magnetic C-forms, as far as they are the most interesting configurations. Particularly, we will define their vibrational and excited states properties.

Vibrational properties Calculated local vibrational modes of all three forms are presented in Table 6.2 along with the results of previous theoretical and experimental data, reported in literature. The values are in a good agreement with other works. Almost all frequencies of the A and the B complex differs from those of Docaj *et al* [35] for less than 30 cm^{-1}, except low frequency mode: 608 cm^{-1} in our study vs 663 cm^{-1} in the study of Docaj *et al.* For the C-form our results differs in larger extend. This can be related to the differing geometries of the C-form between our and Docaj's study. Spin polarization was not taken into account in the study of Docaj, thus they could deal with the D-form or another local minima. The obtained results can be a reference point for the future IR experiments, indicating the energy range for a possible LVM bands of the C-form. For example, in the study of Lavrov *et al* [67], there was an assumption, that only B form is existing in neutral form, that is why the reported IR spectra were ranged up to 1000 cm^{-1} and above 7000 cm^{-1}. While according to our calculations the highest frequency of C-form correspond to 1135 cm^{-1} and is obviously out of the scope of just mentioned work.

this study theory			Docaj [35] theory		
A	**B**	**C-SP**	A	B	C-NSP
933	**819**	**1135**	917	805	1181
861	**702**	**801**	912	704	810
699	**608**	**733**	710	663	806
572	**548**	**549**	598	567	580
566	**525**		591	563	
	521			549	
Leary [69] theory	Capaz [22] theory		Lavrov [67] experiment		Lavrov [68] experiment
B	A	B	A	B	N/A
838	890	841	953	842	527
715	874	716	873	730	749
649	722	643	722	641	
582	567	567	597	580	
552	557	514	594	543	
543		503		540	

Table 6.2: Frequencies in cm^{-1} of the three forms of C_iC_s pair.

Energetic properties First, we consider the electronic energy states distribution of the pristine silicon withing DFT-NSCF (non self consistent field) and GW approaches. We performed calculations within a 216 Si supercell with Γ-point sampling. From the obtained spectra we extracted band gap values, which are listed in Table 6.3. The obtained results clearly indicate the significantly underestimated band gap of about 0.75 eV for pristine silicon. The presence of a defect in the supercell causes a reduction of this band gap. The GW approximation, with Γ-point sampling, enlarged the band gap of the pristine silicon up to 1.14 eV. This value agrees well with the experimental value of silicon's bandgap of 1.1 eV [123]. The calculated band gaps for the supercells, containing the A-, B-, and C-forms of C_iC_s, were found to be reduced compare to the pristine case by 0.17 eV, 0.10 eV, and 0.49 eV, respectively.

complex	E_{gap}^{nscf}, eV	E_{gap}^{GW}, eV	GW defect levels, eV
Bulk	0.75	1.14	
C_iC_s A-form	0.63	0.97	-0.11; 0.64
C_iC_s B-form	0.66	1.04	-0.34; 0.77
C_iC_s C-form (SP)	0.72	0.65	-0.28,-0.29(↑);0.61,0.62(↓)

Table 6.3: Band gaps and defect levels obtained using NSCF-DFT and GW approximations for the bulk and the three forms of C_iC_s complex. Presented results correspond to the Γ-point calculations.

We have also calculated the density of states corresponding to the three forms of the C_iC_s complex. Calculated within the DFT-NSCF approach, they are represented

in Figure 6.8. To verify the convergence of the DOS spectra, we performed calculations for the three other k-point samplings: 2x2x2 and 3x3x3 meshes.

According to the DOS spectra, we infer the importance of the use of 2x2x2 mesh for GW calculations to obtain the proper excited states energy calculations. The peaks obtained using 2x2x2 and 3x3x3 k-points mesh, projected to the C atoms, are shifted with respect to Γ-point calculations. However, such calculations was found to be too heavy with respect to capacity of the supercomputer in terms of memory consumption ($>$ 4000 cores). That is why, as a first attempt, we performed only the $\Gamma-$point calculations of excited states properties using the GW approximation.

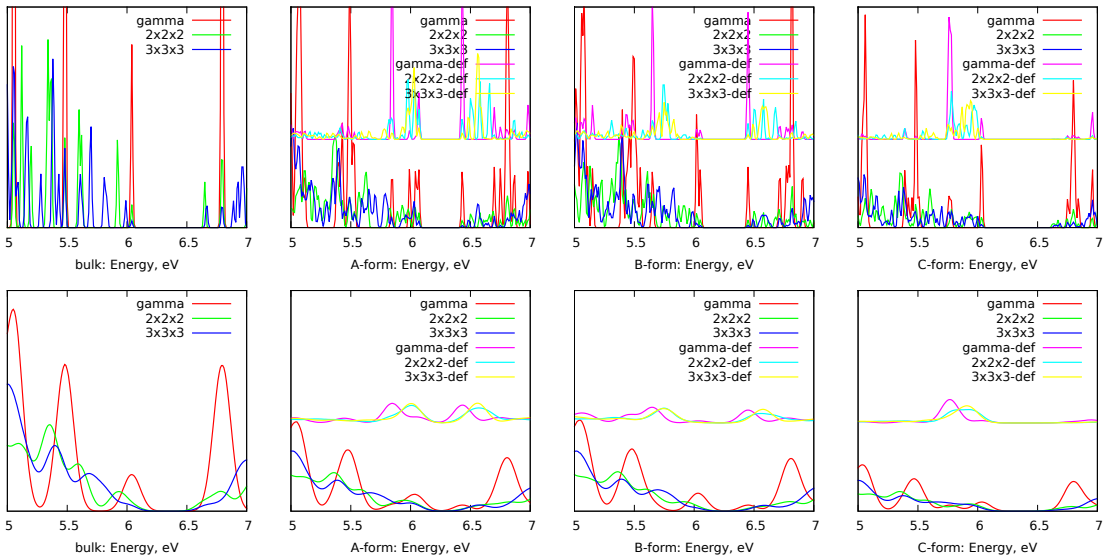

Figure 6.8: From left to right: k-point mesh convergence of the density of states for the bulk Si, A-form, B-form, and C-form. The top and the bottom figures are plotted with the fine and coarse smearing parameter, respectively. The density of states projected on C-C pair ("-def" spectra) are shifted upwards.

The GW approximation provides the excited states energy levels and gives a possibility to calculate the optical absorption/emission spectra. These spectra have been calculated using the quasiparticle and many-body Bethe-Salpeter approaches. The optical spectra for the three forms are illustrated in Figure 6.9. The spectrum of the pristine silicon is flat in the considered wavelength range between 1000 nm and 1700 nm. However, the three complexes introduce bands in that region. For the three cases, it is obvious that the electron-hole interaction are of great importance. Indeed, all the three spectra calculated using the Bethe-Salpeter equation, accounting for the electron-hole interactions, differs significantly from the quasiparticle approximation (QPA).

In the Bethe-Salpeter approximation, each of them introduce a band with the wavelength close to 1280 nm (0.97 eV), the band of G-centre. This finding makes difficult to assign any of these complex responsible for the signal from the G-centre,

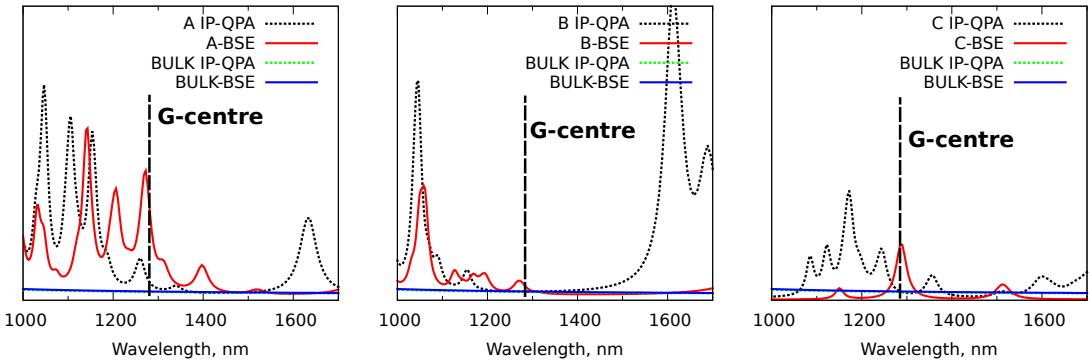

Figure 6.9: The calculated absorbtion/emission spectra corresponding for the three forms of C_iC_s pair.

as all of them are good candidates. Figure 6.9 demonstrates qualitatively different spectra for three cases. All of them have peaks close to required 1280 nm. We observe, several peaks on the spectrum of the A-form, with a quite intensive peak in the 1250-1300 nm region. The smaller peaks are also visible for the B- and C-forms. Regarding these peaks positions, A- and C- are the most interesting ones, as they are located exactly on the G-centre line, while that of B-form is slightly shifted to the lower wavelength direction. Therefore, according to the present investigation of the optical properties, all three tested forms of C_iC_s complex are potentially responsible for the emitting G-centre. However, as we mentioned previously, the calculations of the excited state properties should be performed with at least 2x2x2 k-point mesh.

6.3.1 Discussion and conclusion

In the present Chapter we have performed a detailed investigation on the properties of the forms of the C_iC_s complex from first principles calculations. From the combined experimental-theoretical study, we concluded, that the binding energy of the C-form corresponds to the dissociation energy of the observed C_iC_s complex (7819 cm^{-1}). The obtained results are sustainable, as the binding energies of a wide range of reference complexes (VO_i, C_iO_i, C_iO_iI, *etc*) are in excellent agreement with experimental dissociation energies.

We intend to better understand what are the properties of the possible forms of C_iC_s complex and why the C-form, which is stable according to our calculations, has been never experimentally observed so far. In addition, we tried to characterize theoretically the optical properties of the mentioned forms of carbon-carbon pair, and assign one of them to the light emitting G-centre.

Regarding to the thermodynamic stability, the C-form is an excellent candidate to be responsible for the 7819 cm^{-1} band, observed in experiment. However, the highest LVM band (1135 cm^{-1}) of this form might be beyond the IR window, while

the others can be weakened, superposed with other bands, or obscured by noise. A careful low temperature IR spectroscopy experiments should be performed in order to verify our findings.

Surprisingly, no evidences of C-form have been obtained by the Electronic Paramagnetic Resonance technique, which is another effective characterization method. However, as the C-form is a magnetic complex according to our simulations, its signal should lie in a range of the spectra, situating far from the signal of neutral species.

Therefore, additional characterization experiments are also important, in order to investigate the C-form of the C_iC_s complex. These characterizations should account for the complexe's vibrational properties, obtained in the current study, as well as its magnetization.

Regarding now the form responsible for the light emitting G-centre, we cannot provide a definite answer so far. The converged 2x2x2 k-point mesh calculations are essential to derive the final and converged conclusions.

Chapter 7

Conclusions and perspectives

This work covers a range of problems related with point defects in crystalline silicon. Particularly, by means of first principles simulations, we investigated the defect interaction of both types long range and short range. The former refers to the impact of heavy doping on diffusivity of interstitial oxygen species, while the latter accounts for the various point defect complexes and their thermodynamic, kinetic, and optical properties. Formation of these complexes can be induced by electron irradiation of Czochralski silicon.

All the studied phenomena are closely related with recent experimental investigations and their aim is to further improve the fundamental understanding in the field of silicon based photovoltaic and microelectronic applications. Nowadays, the technology needs to go towards the size reduction and the cheapness. In this regard, all the aspects related with point defects become crucial. For instance, in microelectronic industry, the width of a conducting line in an integrated circuit drops down to a few tens of nanometers. And certainly, such small devices become extremely sensitive to even a tiny concentrations of detrimental point defects. While in the photovoltaic industry, cheap cleaning procedures lead to elevated concentrations of recombinating point defects and complexes, which lead to reduced performances of solar panels.

The first problem that we dealt with in this thesis, was the enhanced and retarded oxygen diffusion in heavily doped silicon. We performed our simulations in Density Functional Theory approximation using the BigDFT tool. The latter is a wavelet based real space code and is perfectly suited for inhomogeneous systems, such as crystals with point defects. We calculated the diffusion coefficient of oxygen migrating species, namely monomer and dimer, in pristine silicon supercell and in silicon supercell containing a dopant atom (p-type, isovalent, or n-type). The obtained diffusion coefficients as a function of temperature are in a very good agreement with experimental results that demonstrates the validity of the applied methodology. That allows constructing a fundamental explanation of the experimentally observed

phenomena. First, we eliminated the effect of the uniaxial and biaxial strains. We showed that monomer's diffusion coefficient are not impacted by the external strains in a range from -1% to $+1\%$.Then, we demonstrated that the enhanced diffusivity in B-doped silicon occurs through a charge transfer mechanism. The charge transfer leads to the reduced migration energy of the oxygen monomer, and thus an enhanced diffusivity at low temperature regime ($T < 700$ ℃). In the B-doped case, the monomer becomes the primary diffusing particle at low temperatures. In the Sb-doped case, the oxygen monomer is also the primary migrating species at low temperatures, however the underlying mechanism is different. In proximity of the Sb atom, oxygen dimer becomes unstable, resulting in a "normal" monomer's diffusion with a migration energy of 2.5-3.0 eV. Nevertheless, the dimers are the primary diffusing species for the undoped, Ge or As doped silicon. We have also observed, that the dimer's migration mechanism is slightly sensitive to a dopant presence in the supercell, however, its diffusivity becomes retarded to different extents for all dopants (B, Ge, and As) compare to undoped silicon supercell. Our results excellently agree with experimental values for almost all cases. However, at the high temperatures in heavily B-doped silicon, our results suggest and enhanced diffusivity of monomer in the whole considered temperature range (400 ℃ $< T <$ 1000 ℃), while a normal diffusion is observed in experiments. Therefore, further exploration of the temperature dependence of the charge transfer mechanism is necessary.

Regarding the second aspect addressed in this thesis, we performed a combined experimental-theoretical investigation of the short range interactions in electron irradiated silicon. Particularly, we aimed to identify the impact of isovalent doping (C, Ge) and co-doping (C-Ge, C-Sn, C-Pb) on the production of different complexes (VO_i, C_iO_i, C_iC_s, *etc.*) which are electrically and optically active. Some of the complexes can be detrimental for the electronic and photovoltaic devices, while others, in contrary, can expand the application area of crystalline silicon. For that extent, the use of isovalent dopants have been shown to be a successful point defect engineering tool in order to reduce the detrimental pairs formation, such VO_i and C_iO_i. Here, we investigated experimentally the production and temperature evolution of irradiation induced complexes in isovalently doped and co-doped silicon. However, the underlying mechanisms are not always directly accessible by experimental techniques so far. For example, some complexes can be invisible via the IR spectroscopy measurement: they can be shadowed by other bands or be obscured by noise. We have also addressed thermodynamical aspect of all possible complexes stability by means of *ab initio* study.

Such a combined experimental-theoretical analysis suggests that the reduced formation of VO_i paris occurs due to the formation of the DV and DC complexes, where D is one of the oversized isovelant dopants, namely Ge, Sn, or Pb. The

complexes can be formed as a result of a chain of the two following reactions:

$$\begin{aligned} D + V &\rightarrow DV \\ DV + Ci &\rightarrow DC. \end{aligned} \tag{7.1}$$

Besides, the thermodynamics of a wide range of possible defect complexes was considered theoretically in isovalently doped material.

However, understanding of the temperature evolution requires the consideration of the kinetic aspects. The latter becomes crucial because of the following reasons: firstly, experimental conditions (namely electron-irradiation and temperature regime) are far from the thermodynamic equilibrium; secondly, due to the numerous reactions, with similar thermodynamic characteristics, the concentrations of the complexes are driven mainly by the kinetics of their components. To that purpose, we applied the Kinetic Mass Action Low techniques to simulate the experiments and extracted the chains of reactions of complexes associations, dissociations, and reassociations. That DFT-KMAL multiscale simulations proved to be a powerful tool in order to understand such a complex processes and should be soon applied for the isovalently co-doped cases. However, the KMAL simulations require certain calibrations to reproduce the experimental data. For example, losses of diffusing species during reassociations at high temperatures should be carefully taken into account. The method allows reproducing the chains of reactions and distinguishing between the forms of a complex. For example, the C-form of C_iC_s complex was associated with the dissociation energy of a carbon-carbon pair, instigating us to further investigate the properties of the carbon-carbon pair.

Indeed, among the three main electron-irradiation induced pairs, C_iC_s complex are of particular interest, as it is widely accepted to be responsible for the optically active G-centre, emitting light at 0.97 eV. Three stable geometry configurations of the complex have been proposed in literature, namely A-, B-, and C-form. According to our results, the C-form, being paramagnetic, is the most stable, and is 0.42 eV and 0.35 eV more stable than A- and B-forms, respectively. We obtained the localized vibrational modes for all three forms. For A- and B-forms, our results are in agreement with previous theoretical and experimental studies. While those of the C-form deviates from previous calculations of similar complex. The B-form is widely accepted to be responsible for the light-emitting G-centre, however there was no theoretical confirmation so far. Here, we performed the calculations of the optical properties. Although we obtained the preliminary results, more precise calculations are required to answer the question: which complex is responsible for the optically active G-centre.

Appendix A

Total energy values for the point defects and defect complexes

Defect	E_{tot} $[Ha]$
Si	-850.63905
V	-846.57455
I	-854.46015
O_i	-866.69953
C	-852.34509
Ge	-850.63093
Sn	-850.17326
Pb	-850.22513
O_{i2}	-882.76508
V_2	-842.57737
VO_i	-862.69016
VO_{i2}	-878.79490
V_2O_i	-858.67841
V_2O_{i2}	-874.78733
C_iO_i	-872.32743
C_iO_iI	-876.18857
C_sO_i	-868.32918
C_sO_{i2}	-884.49798
C_i	-856.21943
C_iC_i	-861.88360
C_sC_i-A	-857.95721
C_sC_i-B	-857.95967

C_sC_i-C	-857.96639
C_sC_i-C (SP)	-857.93954
C_sC_i-D	-857.95797
CV	-848,29266
GeV	-846.57636
SnV	-846.15161
PbV	-846.21120
CVO_i	-864.41031
$GeVO_i$	-862.69115
$SnVO_i$	-862.25362
$PbVO_i$	-862.31389
CC	-853.–830
GeC	-852.33460
SnC	-851.89077
PbC	-851.94340
CI site 1	-856.19834
GeI site 1	-854.45197
SnI site 1	-853.98878
PbI site 1	-854.04652
C_i	-856.21943
Ge_i	-854.45554
Sn_i	-853.98930
Pb_i	-854.04803
C_iC_s site 1	-857.91516
C_iC_s site 2 conf A	-857.95751
C_iC_s site 2 conf B	-857.96005
C_iC_s split conf C-SP	-857.97257
C_iGe_s site 1	-856.19495
C_iGe_s site 2	-856.21027
C_iSn_s site 1	-855.73541
C_iSn_s site 2	-855.74588
C_iPb_s site 1	-855.78334
C_iPb_s site 2	-855.79880

Appendix B

List of publications and conference contributions

B.1 Publications

— E. N. Sgourou, D. Timerkaeva, C. A. Londos, D. Aliprantis, A. Chroneos, D. Caliste, and P. Pochet, *"Impact of isovalent doping on the trapping of vacancy and interstitial related defects in Si"*, J. Appl. Phys., 113, 113506 (2013)

— E. N. Sgourou, D. Timerkaeva, C. A. Londos, D. Aliprantis, A. Chroneos, D. Caliste, and P. Pochet, *"Erratum on [Impact of isovalent doping on the trapping of vacancy and interstitial related defects in Si (vol 113, 113506, 2013)]"*, J. Appl. Phys., 113, 239901 (2013)

— C. A. Londos, E. N. Sgourou, D. Timerkaeva, A. Chroneos, P. Pochet, and V. V. Emtsev, *"Impact of isovalent doping on radiation defects in silicon"*, J. Appl. Phys., 114, 113504 (2013)

— D. Timerkaeva, D. Caliste, and P. Pochet, *"Deciphering mechanisms of enhanced-retarded oxygen diffusion in doped Si"*, Appl. Phys. Lett., 103, 251909 (2013)

— G. Brenet, D. Timerkaeva, E. N. Sgourou, C. Londos, D. Caliste, and P. Pochet, *"Predicting the impurity-defect complexes population in silicon: a coupled DFT/continuous kinetic study"*, in preparation

— D. Timerkaeva, D. Caliste, T. Deutsch, and P. Pochet *Possible mechanisms of oxygen enhanced and retarded diffusion: DFT study*, in preparation

B.2 Conference contributions

— Oral conference contributions:
  - 6^{th} International Workshop on Crystalline Silicon for Solar Cells CSSC'6 (France)
  - 3^{rd} International Conference on Statistical Physics and Mathematics of Complex Systems SPMCS'2012 (Russia)
  - 15^{th} forum on Gettering and Defect Engineering in Semiconductor Technology GADEST'2013 (England)

— Posters:
  - European Material Research Society Spring Meeting E-MRS'2014 (France)

Bibliography

[1] D. Aberg, B. G. Svensson, T. Hallberg, and J. L. Lindstrom. Kinetic study of oxygen dimer and thermal donor formation in silicon. *Phys. Rev. B*, 58:12944, 1998.

[2] J. Adey, J. P. Goss, R. Jones, and P. R. Briddon. Interstitial boron defects in si. *Physica B: Condensed Matter*, 340–342(0):505 – 508, 2003.

[3] J. Adey, R. Jones, D. W.Palmer, P. R. Briddon, and S. Öberg. Degradation of boron-doped czochralski-grown silicon solar cells. *Phys. Rev. Lett.*, 93:055504, 2004.

[4] J. Xu amd N. Wang and D. Yang. Influence of oxygen precipitation on copper precipitation in czochralski silicon. *J. Appl. Phys.*, 111:094907, 2012.

[5] A. Baghdadi, W. M. Bullis, M. C. Croarkin, L. Yue-Zhen, R. I. Scace, R. W. Series, and M. J. Watanabe P. Stallhoffer. Interlaboratory determination of the calibration factor for the measurement of the interstitial oxygen content of silicon by infrared absorption. *J. Electrochem. Soc.*, 136:2015, 1989.

[6] K. Bergman, M. Stavola, S. J. Pearton, and J. Lopata. Donor-hydrogen complexes in passivated silicon. *Phys. Rev. B*, 37:2770R, 1988.

[7] D. D. Berhanuddin, M. Lourenco, R. M. Gwilliam, and K. P. Homewood. Co-implantation of carbon and protons: an integrated silicon device technology compatible method to generate the lasing g-center. *Advanced Functional Materials*, 22(13):2709–2712, 2012.

[8] D. D. Berhanuddin, M. Lourenco, C. Jeynes, M. Milosavljevic, R. M. Gwilliam, and K. P. Homewood. Structural analysis of silicon co-implanted with carbon and high energy proton for the formation of the lasing g-centre. *J. Appl. Phys.*, 112(10):103110, 2012.

[9] M. Besson and G. G. DeLeo. Electronic structure of interstitial carbon in silicon. *Phys. Rev. B*, 43:4028, 1991.

[10] J. F. Binder and A. Pasquarello. Minimum energy path and atomistic mechanism of the elementary step in oxygen diffusion in silicon: A density-functional study. *Phys. Rev. B*, 89:245306, 2014.

[11] E. Bitzek, P. Koskinen, F. Gähler, M. Moseler, and P. Gumbsch. Structural relaxation made simple. *Phys. Rev. Lett.*, 97:170201, 2006.

[12] K. Bothe and J. Schmidt. Electronically activated boron-oxygen-related recombination centers in crystalline silicon. *J. Appl. Phys.*, 99:013701, 2006.

[13] J. Bourgoin, D. Peak, and J. W. Corbett. Ionization-enhanced diffusion: Ion implantation in semiconductors. *J. Appl. Phys.*, 44:3022, 1973.

[14] J. C. Bourgoin, J. W. Corbett, and H. L. Frisch. Ionization enhanced diffusion. *J. Chem. Phys.*, 59:4042, 1973.

[15] A. Brelot and J. Charlemagne. *Radiat. Eff.*, 8:161, 1971.

[16] S. D. Brotherton and P. Bradley. Defect production and lifetime control in electron and gamma-irradiated silicon. *J. Appl. Phys.*, 53:5720, 1982.

[17] K. L. Brower. Epr of a jahn-teller distorted (111) carbon interstitially in irradiated silicon. *Phys. Rev. B*, 9:2607–2617, 1974.

[18] J. A. Burton, R. C. Prim, and W. P. Slichter. The distribution of solute in crystals grown from the melt. part i. theoretical. *J. Chem. Phys.*, 21:1987–1991, 1953.

[19] G. Bussi. Effects of the electron–hole interaction on the optical properties of materials: the bethe–salpeter equation. *Physica Scripta*, 2004:141, 2004.

[20] D. Caliste and P. Pochet. Vacancy-assisted diffusion in silicon: a three-temperature-regime model. *Phys. Rev. Lett.*, 97:135901, 2006.

[21] D. Caliste, K. Z. Rushchanskii, and P. Pochet. Vacancy-mediated diffusion in biaxially strained si. *Appl. Phys. Lett.*, 98:031908, 2011.

[22] R. B. Capaz, A. Dal Pino, and J. D. Joannopoulos. Theory of carbon-carbon pairs in silicon. *Phys. Rev. B*, 58:9845–9850, 1998.

[23] J. Chen, D. Yang, X. Ma, R. Fan, and D. Que. Enhanced oxygen out-diffusion in silicon crystal doped with germanium. *J. Appl. Phys.*, 102:066102, 2007.

[24] A. Chroneos, C. A. Londos, E. N. Sgourou, and P. Pochet. Point defect engineering strategies to suppress a-center formation in silicon. *Appl. Phys. Lett.*, 99:241901, 2011.

[25] C. Claeys, E. Simoen, V. B. Neimash, A. Kraitchinskii, M. Kras'ko, O. Puzenko, A. Blondeel, and P. Clauws. Tin doping of silicon for controlling oxygen precipitation and radiation hardness. *J. Electrochem. Soc.*, 148:G738–G745, 2001.

[26] J. W. Corbett, G. D. Watkins, , and R. S. McDonald. New oxygen infrared bands in annealed irradiated silicon. *Phys. Rev.*, 135:A1381, 1964.

[27] J. Coutinho, R. Jones, P. R. Briddon, and S. Öberg. Oxygen and dioxygen centers in si and ge: Density-functional calculations. *Phys. Rev. B*, 62:10824–10840, 2000.

[28] J. Coutinho, R. Jones, P. R. Briddon, S. Öberg, L. I. Murin, V. P. Markevich, and J. L. Lindstrom. Interstitial carbon-oxygen center and hydrogen related shallow thermal donors in si. *Phys. Rev. B*, 65:014109, 2001.

[29] C. Cui, X. Ma, and D. Yang. Enhanced oxygen diffusion in czochralski silicon at 450–650 c. *physica status solidi (a)*, 205(5):1148–1151, 2008.

[30] J. Czochralski. Ein neues verfahren zur messung der kristallisationsgeschwindigkeit der metalle [a new method for the measurement of the crystallization rate of metals]. *Zeitschrift für Physikalische Chemie*, 92:219, 1917.

[31] M. L. David, E. Simoen, C. Claeys, V. Neimash, M. Kras'ko, A. Kraitchinskii, V. Voytovych, A. Kabaldin, and J. F. Barbot. Electrically active defects in irradiated n-type czochralski silicon doped with group iv impurities. *J. Phys.: Condens. Matter*, 17:S2255–S2266, 2005.

[32] G. Davies. In Mahajan, editor, *Handbook of semiconductors*, pages 1557–1635. Elsevier, 1994.

[33] G. Davies, E. C. Lightowlers, R. C. Newman, and A. S. Oates. A model for radiation damage effects in carbon-doped crystalline silicon. *Sci. Technol.*, 2:524–532, 1987.

[34] A. K. Deb. *Lacunes chargées, etude dans des nano-agregats de silicium.* PhD thesis, l'Ecole Doctorale de Physique des Matériuax, 3 2012.

[35] S. Docaj and S. Estreicher. Three carbon pairs in si. *Physica B: Condens. Matter*, 407:2981–2984, 2012.

[36] D. A. Drabold and S. Estreicher. *Theory of defects in semiconductors.* Springer, 2007.

[37] M.-H. Du, H. M. Branz, R. S. Crandall, and S. B. Zhang. Bistability-mediated carrier recombination at light-induced boron-oxygen complexes in silicon. *Phys. Rev. Lett.*, 97:256602, 2006.

[38] J. Dzelme, I. Ertsinsh, B. Zapol, and A. Misiuk. Structure and diffusion of oxygen and silicon interstitials in silicon. *J A C*, 286:254–257, 1999.

[39] R. Elber and M. Karplus. A method for determining reaction paths in large molecules: Application to myoglobin. *Chem. Phys. Lett.*, 139:375–380, 1987.

[40] S. K. Estreicher, D. J. Backlund, C. Carbogno, and M. Scheffler. Activation energies for diffusion of defects in silicon: the role of the exchange-correlation functional. *Angewandte Chemie (International ed. in English)*, 50(43):10221, 2011.

[41] B. Ewels, R. Jones, and S. Öberg. Oxygen-carbon, oxygen-nitrogen and oxygen-dimer defects in silicon. In R. Jones, editor, *Early stages of oxygen in silicon*, page 141. Kluwer Academic Publishers, 1996.

[42] H. Fischer and W. Pschunder. *Proc. of the 10th IEEE Photovoltaic Specialists Conference*, 404, 1973.

[43] M. Forster, E. Fourmond, F. E. Rougieux, A. Cuevas, R. Gotoh, K. Fujiwara, S. Uda, and M. Lemiti. Boron-oxygen defect in czochralski-silicon co-doped with gallium and boron. *Appl. Phys. Lett.*, 100:042110, 2012.

[44] M. Furuhashi and K. Taniguchi. Diffusion and dissociation mechanisms of vacancy-oxygen complex in silicon. *Appl. PHys. Lett.*, 86:142107, 2005.

[45] L. Genovese, A. Neelov, S. Goedecker, T. Deutsch, S. A. Ghasemi, A. Willand, D. Caliste, O. Zilberberg, M. Rayson, A. Bergman, and R. Schneider. Daubechies wavelets as a basis set for density functional pseudopotential calculations. *J. Chem. Phys.*, 129(1):014109, 2008.

[46] A. Giannattasio, J. D. Murphy, S. Senkader, R. J. Falster, and P. R. Wilshaw. Oxygen and nitrogen transport in silicon investigated by dislocation locking experiments. *J. Electrochem. Soc.*, 152(6):G460, 2005.

[47] U. Gösele and T. Y. Tan. Oxygen diffusion and thermal donor formation in silicon. *Appl. Phys. A*, 28(2):79–92, 1982.

[48] W. Götz, N. M. Johnson, D. P. Bour, M. D. McCluskey, and E. E. Haller. Local vibrational modes of the mg–h acceptor complex in gan. *Appl. Phys. Lett.*, 69:3725, 1996.

[49] V. Gusakov. Unified model of diffusion of interstitial oxygen in silicon and germanium crystals. *J. Phys. Cond. Matt.*, 17:S2285–S2291, 2005.

[50] V. Gusakov. First principle study on the diffusion of oxygen and oxygen complexes in si, si<ge> solid solutions and si nanocrystals. *Solid State Phenomena*, 205-206:171–180, 2014.

[51] S. Hahn, H. J. Stein, S. C. Shatas, and F. A. Ponce. Thermal donor formation and annihilation in oxygen-implanted float-zone silicon. *J. Appl. Phys.*, 72:1758, 1992.

[52] B. Hammer, L. B. Hansen, and J. K. Nørskov. Improved adsorption energetics within density-functional theory using revised perdew-burke-ernzerhof functionals. *Phys. Rev. B*, 59:7413, 1999.

[53] S. Hao, L. Kantorovich, and G. Davies. The interstitial cioi defect in bulk si and si(1−x)ge(x). *J. Phys.: Cond. Matt.*, 16:8545, 2004.

[54] L. Hedin. New method for calculating the one-particle green's function with application to the electron-cas problem. *Phys. Rev.*, 139:A796, 1965.

[55] L. Hedin and A. Johansson. Effects of electron-electron and electron-phonon interactions on the one-electron states of solids. *Sol. Stat. Phys.*, 23:1, 1969.

[56] T. Hoshino and Y. Nishioka. Inward diffusion of oxygen on a silicon surface. *Phys. Rev. Lett.*, 84:4633, 2000.

[57] R. Hull. *Properties of crystalline silicon*. INSPEC, the Institution of Electrical Engineers, London, United Kingdom, 1999.

[58] A. A. Istratov, T. Buonassisi, R. J. McDonald, A. R. Smith, R. Schindler, J. A. Rand, J. P. Kalejs, and E. R. Weber. Metal content of multicrystalline silicon for solar cells and its impact on minority carrier diffusion length. *J. Appl. Phys.*, 94:6552, 2003.

[59] Z. Jiang and R. A. Brown. Atomistic calculation of oxygen diffusivity in crystalline silicon. *Phys. Rev. Lett.*, 74:2046, 1995.

[60] J. C. Mikkelsen Jr. The diffusivity and solubility of oxygen in ssilicon. *MRS Proceedings*, 59, 1986.

[61] A. Khan, M. Yamaguchi, Y. Ohshita, N. Dharmarasu, K. Araki, T. Abe, H. Itoh, T. Ohshima, M. Imaizumi, and S. Matsuda. Role of the impurities in production rates of radiation-induced defects in silicon materials and solar cells. *J. Appl. Phys.*, 90:1170, 2001.

[62] L. I. Khirunenko, Yu. V. Pomozov, M. G. Sosnin, A. V. Duvanskii, N. A. Sobolev, N. V. Abrosimov, and H. Riemann. Oxygen diffusion in si1−xgex alloys. *Phisica B: Cond. Matt.*, 404:4698–4700, 2009.

[63] L. I. Khirunenko, V. I. Shakhovtsov, V. V. Shumov, and V. I. Yashnik. Reactions between point defects in silicon doped with germanium. *Mater. Sci. Forum*, 196-201:1381–4, 1995.

[64] W. Kohn and L. J. Sham. Self-consistent equations including exchange and correlation effects. *Phys. Rev.*, 140:A1133, 1965.

[65] M. Krack. Pseudopotentials for h to kr optimized for gradient-corrected exchange-correlation functionals. *Theoretical Chemistry Accounts*, 114(1-3):145–152, 2005.

[66] R. Laiho, M. P. Vlasenko, and L. S. Vlasenko. New low symmetry configuration of the two carbon-interstitial silicon complex in irradiated silicon. *Solid Stat. Comm.*, 124:403–406, 2002.

[67] E. V. Lavrov, L. Hoffmann, and B. B. Nielsen.

[68] E. V. Lavrov, B. B. Nielsen, J. R. Byberg, B. Hourahine, R. Jones, S. Öberg, and P. R. Briddon. Local vibrational modes of two neighboring substitutional carbon atoms in silicon. *Phys. Rev. B*, 62:158–165, 2000.

[69] P. Leary, R. Jones, S. Öberg, and V. J. B. Torres. Dynamic properties of interstitial carbon and carbon-carbon pair defects in silicon. *Phys. Rev. B*, 55:2188–2194, 1997.

[70] S.-T. Lee, P. Fellinger, and S. Chen. Enhanced and wafer-dependent oxygen diffusion in cz-si at 500-700 c. *J. Appl. Phys.*, 63:1924, 1988.

[71] Y. J. Lee, J. von Boehm, M. Pesola and R. M. Nieminen. First-principles study of migration, restructuring, and dissociation energies of oxygen complexes in silicon. *Phys. Rev. B*, 65:085205, 2002.

[72] B. Lim, F. Rougieux, D. Macdonald, K. Bothe, and J. Schmidt. Generation and annihilation of boron–oxygen-related recombination centers in compensated p- and n-type silicon. *J. Appl. Phys.*, 108:103722, 2010.

[73] J. L. Lindström and B. G. Svensson. Oxygen, carbon, hydrogen, and nitrogen in crystalline silicon. *MRS symposia proceeding*, 59:45, 1986.

[74] C. L. Liu, W. Windl, L. Borucki, S. F. Lu, and X. Y. Liu. Ab initio modeling and experimental study of c-b interactions in si. *Appl. Phys. Lett.*, 80:52–54, 2002.

[75] C. A. Londos, A. Andrianakis, V. Emtsev, and H. Ohyama. Radiation effects on the behavior of carbon and oxygen impurities and the role of ge in czochralski grown si upon annealing. *J. Appl. Phys.*, 105:123508, 2009.

[76] C. A. Londos, A. Andrianakis, V. V. Emtsev, G. A. Oganesyan, and H. Ohyamac. Effects of germanium doping on the behavior of oxygen and carbon impurities and impurity-related complexes in si. *Physica B: Cond. Matt.*, 404:4693–4697, 2009.

[77] C. A. Londos, A. Andrianakis, V. V. Emtsev, and H. Ohyama. Radiation-induced defects in czochralski-grown silicon containing carbon and germanium. *Semicond. Sci. Technol.*, 24:075002, 2009.

[78] C. A. Londos, A. Andrianakis, E. N. Sgourou, V. Emtsev, and H. Ohyama. Effect of germanium doping on the annealing characteristics of oxygen and carbon-related defects in czochralski silicon. *J. Appl. Phys.*, 107:093520, 2010.

[79] C. A. Londos, A. Andrianakis, E. N. Sgourou, V. V. Emtsev, and H.Ohyama. Ir studies of the impact of ge doping on the successive conversion of von defects in czochralski-si containing carbon. *J. Appl. Phys.*, 109:033508, 2011.

[80] C. A. Londos, G. D. Antonaras, M. S. Potsidi amd A. Misiuk, I. V. Antonova, and V. V. Emtsev. Production and evolution of defects in neutron-irradiated si subjected to thermal pre-treatments under hydrostatic pressure. *J. Phys.: Condens. Matter*, 17:S2341, 2005.

[81] C. A. Londos, D.Aliprantis, E. N. Sgourou, A. Chroneos, and P. Pochet. Formation and evolution of oxygen-vacancy clusters in lead and tin doped silicon. *J. Appl. Phys.*, 111:123508, 2012.

[82] C. A. Londos, M. S. Potsidi, and E. Stakakis. Carbon-related complexes in neutron-irradiated silicon. *Physica B: Cond. Matt.*, 340-342:551–555, 2003.

[83] C. A. Londos, E. N. Sgourou, and A. Chroneos. Defect engineering of the oxygen-vacancy clusters formation in electron irradiated silicon by isovalent doping: An infrared perspective. *J. Appl. Phys.*, 112:123517, 2012.

[84] C. A. Londos, E. N. Sgourou, D. Timerkaeva, A. Chroneos, P. Pochet, and V. V. Emtsev. Impact of isovalent doping on radiation defects in silicon. *J. Appl. Phys.*, 114:113504, 2013.

[85] C. Maddalon-Vinante, D. Barbier, H. Erramli, and G. Blondiaux. Charged particle activation analysis study of the oxygen outdiffusion from czochralski-grown silicon during classical and rapid thermal annealing in various gas ambient. *J. Appl. Phys.*, 74.

[86] A. Marini, C. Hogan, M. Gruning, and D. Varsano. Yambo: an ab initio tool for excited state calculations. *Comp. Phys. Comm.*, 180:1392, 2009.

[87] A. Mattoni, F. Bernardini, and L. Colombo. Self-interstitial trapping by carbon complexes in crystalline silicon. *Phys. Rev. B*, 66:195214, 2002.

[88] S. A. McQuaid, B. K. Johnson, D. Gambaro, R. Falster, M. J. Ashwin, and J. H. Tucker. The conversion of isolated oxygen atoms to a fast diffusing species in czochralski silicon at low temperatures. *J. Appl. Phys.*, 86:1878, 1999.

[89] A. A. Mostofi, J. R. Yates, Y.-S. Lee, I. Souza, D. Vanderbilt, and N. Marzari. Wannier90: A tool for obtaining maximally-localised wannier functions. *Comp. Phys. Commun.*, 178(9):685 – 699, 2008.

[90] K. Murata, Y. Yasutake, K. Nittoh, S. Fukatsu, and K. Miki. High-density g-centers, light-emitting point defects in silicon crystal. *AIP ADVANCES*, 1:032125, 2011.

[91] L. I. Murin, T. Hallberg, V. P. Markevich, and J. L. Lindstrom. Experimental evidence of the oxygen dimer in silicon. *Phys. Rev. Lett.*, 80:93–96, 1998.

[92] L. I. Murin, E. A. Tolkacheva, V. P. Markevich, A. R. Peaker, B. Hamilton, E. Monakhov, B. G. Svensson, J. L. Lindstrom, P. Santos, J. Coutino, and A. Carvalho. The oxygen dimer in si: its relationship to the light-induced degradation of si solar cells? *Appl. Phys. Lett.*, 98:182101, 2011.

[93] J. D. Murphy, S. Senkader, R. J. Falster, and P. R. Wilshaw. Oxygen transport in czochralski silicon investigated by dislocation locking experiments. *Materials Science and Engineering: B*, 134(2–3):176 – 184, 2006.

[94] V. B. Neimash, V. V. Voitovych, M. M. Kras'ko, A. M. Kraitchinskii, O. M. Kabaldin, Yu. V. Pavlovs'kyi, and V. M. Tsmots'. Formation of radiation-induced defects in n-si with lead and carbon impurities. *Ukr. J. Phys.*, 50:1273–1277, 2005.

[95] R. C. Newman. Oxygen diffusion and precipitation in czochralski silicon. *J. Phys.: Cond. Matt.*, 12(25):R335–R365, 2000.

[96] R. C. Newman, A. K. Tipping, and J. H. Tucker. The effect of metallic contamination on enhanced oxygen diffusion in silicon at low temperatures. *J. Phys. C: Solid. Stat. Phys.*, 18:L861, 1985.

[97] S. Öberg, C. P. Ewels, R. Jones, T. Hallberg, J. L. Lindström, L. I. Murin, and P. R. Briddon. First stage of oxygen aggregation in silicon: the oxygen dimer. *Phys. Rev. Lett.*, 81:2930, 1998.

[98] K. P. O'Donnell, K. M. Lee, and G. D. Watkins. Origin of the 0.97 ev luminescence in irradiated silicon. *Physica B and C*, 116:258–263, 1983.

[99] T. Ono, G. A. Rozgony, E. Asayama, H. Horie, H. Tsuya, and K. Sueoka. Oxygen diffusion in heavily antimony-, arsenic-, and boron-doped czochralski silicon wafers. *J. Appl. Phys*, 74(24):3648, 1999.

[100] M. Pagani. Secondary ion mass spectroscopy determination of oxygen diffusion coefficient in heavily sb doped si. *J. Appl. Phys.*, 68:3762, 1990.

[101] D. Peak, J. Corbett, and J. C. Bourgoin. Ionization enhanced diffusion. *J. Chem. Phys.*, 65:1206, 1976.

[102] J. P. Perdew, K. Burke, and M. Ernzerhof. Generalized gradient approximation made simple. *Phys. Rev. Lett.*, 77:3865, 1996.

[103] J. P. Perdew and Y. Wang. Accurate and simple analytic representation of the electron-gas correlation energy. *Phys. Rev. B*, 45:13244, 1992.

[104] J. P. Perdew and A. Zunger. Self-interaction correction to density-functional approximations for many-electron systems. *Phys. Rev. B*, 23:5048, 1981.

[105] M. Pesola, J. von Boehm, T. Mattila, and R. M. Nieminen. Computational study of interstitial oxygen and vacancy-oxygen complexes in silicon. *Phys. Rev. B*, 60:11449, 1999.

[106] P. Pichler. *Intrinsic point defects, impurities, and their diffusion in silicon.* Springer, 2004.

[107] P. Pochet and D. Caliste. Point defect diffusion in si and sige revisited through atomistic simulations. *Mater. Sci. Semicond. Process.*, 15:675, 2012.

[108] J. Priede and G. Gerbeth. Point defect diffusion in si and sige revisited through atomistic simulations. *J. Cryst. Growth*, 285:261–269, 2005.

[109] P. Pulay. Convergence acceleration of iterative sequences. the case of scf iteration. *Chem. Phys. Lett.*, 73:393–398, 1980.

[110] P. Pulay. Improved scf convergence acceleration. *J. Comp. Chem.*, 3:556–560, 1982.

[111] V. Quemener, B. Raeissi, F. Herklotz, L. I. Murin, E. V. Monakhov, and B. G. Svensson. Kinetics study of vacancy–oxygen-related defects in monocrystalline solar silicon. *physica status solidi (b)*, 251.

[112] M. Ramamoorthy and S. T. Pantelides. Coupled-barrier diffusion: the case of oxygen in silicon. *Phys. Rev. Lett*, 76:267, 1996.

[113] M. Ramamoorthy and S. T. Pantelides. Enhanced modes of oxygen diffusion in silicon. *Solid State Commun.*, 106:243–248, 1998.

[114] J. L. Regolini, J. P. Stoquert, C. Ganter, and P. Siffert. Determination of the conversion factor for infrared measurements of carbon in silicon. *J. Electrochem. Soc.*, 133:2165–2168, 1986.

[115] E. E. Salpeter and H. A. Bethe. A relativistic equation for bound-state problems. *Phys. Rev.*, 84:1232, 1951.

[116] J. Schmidt and K. Bothe. Structure and transformation of the metastable boron- and oxygen-related defect center in crystalline silicon. *Phys. Rev. B*, 69:024107, 2004.

[117] S. Senkader, P. R. Wilshaw, and R. J. Falster. Oxygen-dislocation interactions in silicon at temperatures below 700[U+200A]°c: Dislocation locking and oxygen diffusion. *J. Appl. Phys.*, 89:4803, 2001.

[118] E. N. Sgourou, D. Timerkaeva, C. A. Londos, D. Aliprantis, A. Chroneos, D. Caliste, and P. Pochet. Erratum on [impact of isovalent doping on the trapping of vacancy and interstitial related defects in si (vol 113, 113506, 2013)]. *J. Appl. Phys.*, 113:239901, 2013.

[119] E. N. Sgourou, D. Timerkaeva, C. A. Londos, D. Aliprantis, A. Chroneos, D. Caliste, and P. Pochet. Impact of isovalent doping on the trapping of vacancy and interstitial related defects in si. *J. Appl. Phys.*, 113:113506, 2013.

[120] L. C. Snyder, J. W. Corbett, P. Deáka, and R. Wu. On the diffusion of oxygen dimer in a silicon crystal. *Matter. Res. Soc. Symp. Proc.*, 104:179, 1987.

[121] L. W. Song, X. D. Zhan, B. W. Benson, and G. D. Watkins. Bistable interstitial-carbon - substitutional-carbon pair in silicon. *Phys. Rev. B*, 42(9):5765–5783, 1990.

[122] P. J. Stephens, F. J. Devlin, C. F. Chabalowski, and M. J. Frisch. Ab initio calculation of vibrational absorption and circular dichroism spectra using density functional force fields. *J. Phys. Chem.*, 98:11623–11627, 1994.

[123] B. Streetman and S. Banerjee. *Solid State Electronic Devices*. Prentice Hall, 5 edition, 1999.

[124] Fraunhofer Institute For Solar Energy Systems. Photovoltaics report, 2014.

[125] H. Takeno, Y. Hayamizu, and K. Miki. Diffusivity of oxygen in czochralski silicon at 400-750 c. *J. Appl. Phys.*, 84(6):3113–3117, 1998.

[126] H. Takeno, K. Sunakawa, and M. Suezawa. Temperature-dependent retardation effect of dopants on oxygen diffusion in heavily doped czochralski silicon. *Appl. Phys. Lett.*, 77(3):376–378, 2000.

[127] G. K. Teal and J. B. Little. *Phys. Rev.*, 78:647, 1950.

[128] W. K. Tice and T. Y. Tan. Nucleation of cusi precipitate colonies in oxygen-rich silicon. *Appl. Phys. Lett.*, 28(9):564–565, 1976.

[129] D. Timerkaeva, D. Caliste, and P. Pochet. Deciphering mechanisms of enhanced-retarded oxygen diffusion in doped si. *Appl. Phys. Lett.*, 103:251909, 2013.

[130] A. K. Tipping and R. C. Newman. The diffusion coefficient of interstitial carbon in silicon. *Semicond. Sci. Tech.*, 2:315, 1987.

[131] K. Torigoe, J. Fujise, T. Ono, and K. Nakamura. Enhanced diffusion of oxygen depending on fermi level position in heavily boron-doped silicon. *J. Appl. Phys.*, 116:193503, 2014.

[132] F. A. Trumbore. Solid solubilities of impurity elements in germanium and silicon. *Bell Syst. Tech. J.*, 39:205–233, 1960.

[133] G. H. Vineyard. Frequency factor and isotope effects in solid state rate processes. *J. Phys. Chem. Solids*, 3:121–127, 1957.

[134] V. V. Voronkov and R. Falster. Latent complexes of interstitial boron and oxygen dimers as a reason for degradation of silicon-based solar cells. *J. Appl. Phys.*, 107(5):053509, 2010.

[135] V. V. Voronkov, R. Falster, C. A. Londos, E. N. Sgourou, A. Andrianakis, and H. Ohyama. Production of vacancy-oxygen defect in electron irradiated silicon in the presence of self-interstitial-trapping impurities. *J. Appl. Phys.*, 110:093510, 2011.

[136] K. Wada. United model for formation kinetics of oxygen thermal donors in silicon. *Phys. Rev. B*, 30:5884–5895, 1984.

[137] G. D. Watkins, J. R. Troxell, and A.P. Chatterjee. Defects and radiation effects in semiconductors.

[138] J. Will, A. Groschel, E. Bergmann, E. Spiecker, and A. Magerl. Diffusion-driven precipitate growth and ripening of oxygen precipitates in boron doped silicon by dynamical x-ray diffraction. *J. Appl. Phys.*, 115:123505, 2014.

[139] Z. Zeng, J. D. Murphy, R. J. Falster, X. Ma, D. Yang, and P. R. Wilshaw. The effect of impurity-induced lattice strain and fermi level position on low temperature oxygen diffusion in silicon. *J. Appl. Phys.*, 109(6):063532, 2011.

[140] Y. Zhang and W. Yang. Comment on "generalized gradient approximation made simple". *Phys. Rev. Lett.*, 80:890, 1998.

[141] F. Zirkelbach, B. Stritzker, K. Nordlund, J. K. N. Lindner, W. G. Schmidt, and E. Rauls. Combined ab initio and classical potential simulation study on silicon carbide precipitation in silicon. *Phys. Rev. B*, 84(6):064126, 2011.